The Study of Reactions and Molecules Involved in the Formation of Prebiotic Molecules

By

ANNA CHRISTINA WANNENMACHER

DISSERTATION

Submitted in partial satisfaction of the requirements for the degree of

DOCTOR OF PHILOSOPHY

in

Chemistry

in the

OFFICE OF GRADUATE STUDIES

of the

UNIVERSITY OF CALIFORNIA

DAVIS

Approved:

Davide Donadio, Chair

Musahid Ahmed

R. David Britt

Committee in Charge

2023

*To my parents . . .*

*who have sculpted me, through patience and kindness, into the person I am today. I could never have done this without your love and constant support.*

# Contents

# List of Figures

# List of Tables

# Abstract

**The study of reactions and molecules involved in the formation of prebiotic molecules**

Through my time in graduate school, I have worked on three different gas phase spectroscopy research projects, performed on three unique and different apparatuses, all with astronomical relevance. At the center of these projects is the question, how life came to be on Earth. My research aims to help answer this question by studying reactions and molecules involved in the formation of complex organic molecules (COMs), which are thought to have been involved in the prebiotic/biotic chemistry on Earth and provided much of the organic material in the solar system.

To learn about the formation of COMs, it is necessary to learn about the formation of small molecules that may have played a role in the formation of COMs (project 1), be able to detect these molecules using radio telescopes (project 2), and learn about the environments where they are found (project 3).

Small molecules, such as CO, which may have played a role in the formation of COMs, are thought to have formed in the interstellar medium (ISM) through ion-molecule reactions since these reactions are barrierless and exothermic. To better understand these reactions, my first project was to study 2 ion-molecule reactions. Specifically, I studied the chemical reactivity of vanadium cations with methane and with water as a function of the quantum spin-orbit electronic state of the vanadium cation as well as a function of the center of mass collision energy. The vanadium cation, which is a relevant example for understanding ion reactions in general, was prepared into thirteen electronic states. The vanadium was ionized by two-color vis-UV lasers and prepared into the desired quantum spin-orbit electronic state through a pulsed field ionization-photoion process, then passed through two quadrupoles and two octupoles into the reaction chamber filled with either methane or water, and the formed products were detected by a modified mass spectrometer. From this, the reaction channels at different center of mass collision energies were

determined. The triplet state was shown to be more reactive than the quintet states for both methane and water, while the J-state was found to have no influence on reactivity.

While ion-molecule reactions are able to form small molecules found in the ISM, they have not been able to form larger molecules such as COMs. A proposed reaction pathway to form COMs is through radical-neutral and radical-radical reactions occurring on icy grain mantels in space. In order to predict what reactions may occur in space, it is necessary to know what radicals and other molecules may be in the ISM. Radio telescopes, such as the Atacama Large Millimeter Array (ALMA), can detect the rotational spectra of molecules in space, but without a database to compare to, few complex radicals have been identified. To obtain the rovibrational spectra of radicals thought to be in the ISM, as my next project, I designed a technique and instrument that combines cavity-enhanced frequency modulation spectroscopy with an alternating current magnetic field generated by a solenoid. This produced a sensitive, radical-selective, and Doppler-free technique that can measure rovibrational transitions of radicals with an accuracy and precision of better than 1 MHz. This technique has been named Noise Immune Cavity Enhanced Optical Heterodyne Zeeman Modulation Spectroscopy (NICE-OHZMS).

Since it is proposed that COMs may form on icy mantles of dust grains, my final project looked at how molecules in the icy mantles, specifically water, may affect the reactivity and ionization energy of molecules embedded in these icy mantles. Complex organic molecules, such as alcohols, are thought to freeze onto these icy mantles surrounding dust grains where vacuum ultraviolet (VUV) light in the ISM can photoionize these molecules, forming radical cations that may be involved in the production of precursors to life. To better understand how water may affect ethylene glycol, which has been detected in the ISM and may embed onto these icy mantles, the fundamental interactions between ethylene glycol and water were investigated by studying ethylene glycol water clusters. As a comparison with ethylene glycol, two other diol water cluster systems were studied, specifically, 1,2-propylene glycol water clusters and 1,3-propylene glycol water clusters. The experiments were performed by forming a supsersonic molecular beam of water and the diol of interest, ionizing this with tunable vacuum ultraviolet radiation from the

Advanced Light Source synchrotron, and detecting the ionized clusters using reflectron time of flight mass spectrometry. The ionizing radiation was scanned over a range of photon energies so as to provide information about the formed clusters at these photon energies and, from this, determine the appearance energy of the clusters. Clusters of both diol fragments along with unfragmented diols with water were detected and some have been visualized theoretically. It was found that the addition of the methyl group and the location of the methyl group affected the energy needed to form fragment clusters. Using theory, for certain clusters ionization energies and appearance energies were calculated.

Through these three projects, I have had the opportunity to perform both theory calculations and experiments and learn about different instruments while making a small contribution to the pursuit of how life came to be on Earth.

# Acknowledgments

I want to thank my two PIs, Davide Donadio and Musahid Ahmed who gave me a road through graduate school when things were not going well. They made it so I could make it through graduate school. Thank you to Musa for giving me a very interesting project to work on and for allowing me to work at the ALS, which was a dream of mine from the beginning of graduate school. Thank you to Davide for all your suggestions on my final project and help with it. Thank you to all the people in Davide's group and Musa's group. You all made me feel so welcome and helped me with science and with navigating life's hurtles.

Huge thank you to my parents, who have shown me incredible kindness, love, and support throughout everything. They have been there for all my hurtles and have supported me every step of my life.

Thank you to Ron Zuckermann, who has been an incredible mentor through graduate school. I so appreciate all of our interesting conversations and your advice and understanding. I am so glad I met you at the Molecular Foundry.

Thank you to everyone else who has supported me and helped me along the way and to my thesis committee for reading my thesis. I could not have done it without all the kindness I have been shown by others around me.

I would like to acknowledge the different groups with whom I did research. The work in chapter 2, the ion molecule reactions, was done in Professor Cheuk Ng's group. The work in chapters 3 through 5, setting up the NICE-OHZMS instrument, was done in Professor Kyle Crabtree's group.

# Chapter 1

# Background

What is the origin of life? The pursuit of answering this fundamental question has led to a host of different types of research in a multitude of environments ranging from seemingly inhospitable environments on Earth all the way to the interstellar medium (ISM). The interstellar medium is a rich and diverse environment containing both atomic gas and molecules. These molecules range from ions to neutral molecules to radicals, which are species with an unpaired electron.

These molecules, in the ISM, can be identified via radio astronomical observations from radio telescopes. Radio telescopes, as their name implies, are telescopes that detect radio waves. The incoming wave is detected by several parabolic antennas acting together as one telescope, resulting in the ability to observe very weak signals. This signal is then amplified and recorded. One such radio telescope is the Atacama Large Millimeter/submillimeter Array (ALMA), located in the desert in Chile and composed of 66 antennas working together. ALMA is able to detect waves spanning between radio and infrared due to being located at the most arid desert with the clearest skies and at high altitude [5].

Figure 1.1. An image of the Atacama Large Millimeter/submillimeter Array (ALMA)

One important class of molecules detected by these radio telescopes are carbon containing molecules with at least six or more atoms referred to as complex organic molecules (COMs). These molecules may have contributed to the prebiotic/biotic chemistry on Earth and are thought to have provided much of the organic material in the solar system. One such molecule is glycolaldehyde ($CH_2(OH)(CHO)$), which has been detected near class 0 protostellar binary source IRAS 16293-2422, and near Galactic Center source Sgr B2(N) as well as near other hot cores. While no amino acids have been detected in the ISM, they have been found on meteorites and comets [6]. By understanding the formation of COMs, the formation of the solar system and answers to the origin of life can be better understood.

To learn about the formation of COMs, it is necessary to understand the molecules involved in the reactions producing COMs as well as to learn about how other molecules in the environment affect these reactions. The formation of small molecules such as CO and $H_2O$ in the abundances found in dense molecular clouds has been accomplished through gas phase ion molecule reactions [7]. Many of these reactions are barrierless and exothermic and so could occur in the cold conditions of the ISM. These ion-molecule reactions alone would not be able to form complex organic molecules.

One theorized formation mechanism of COMs is through radical-neutral and radical-radical reactions occurring between molecules embedded onto the surface of icy grain mantles which form around dust grains [8]. Along with water, these icy mantles contain molecules such as $CO_2$ and $CH_4$, which when clustered around embedded molecules may affect their reactivity and ability to form COMs. Some dust grains reside in dark clouds and prestellar cores where the temperature is as low as 10K. In this case, hydrogen atoms in the grain are the most mobile species and so very likely to be involved in reactions with atoms, such as O, C, and N, or simple molecules, such as CO, that absorb onto the grain. Molecules formed through these reactions may undergo cosmic ray induced UV photolysis forming radicals which then further react. These processes can be better understand through cluster experiments involving the species in the icy mantles, some of which have been preformed and are discussed in this thesis.

One proposed COM formation nondiffusive reaction mechanism involves the reaction of newly formed radicals with nearby species on dust grains. This proposed reaction mechanism predicts the production of species in the rough abundance for which they have been detected in the gas phase. The formation of the radical produces enough energy to overcome the activation barrier needed for reaction with a stable species. Using this model, the reaction for the oxygen containing COMs acetaldehyde, methyl formate, and dimethyl ether has been predicted as shown in the reactions below, where * indicates an excited species [6].

Acetaldehyde:

$$H + CH_2 \longrightarrow CH_3^*$$

$$CH_3^* + CO \longrightarrow CH_3CO$$

$$H + CH_3CO \longrightarrow CH_3CHO$$

Methyl Formate:

$$H + H_2CO \longrightarrow CH_3O^*$$

$$CH_3O^* + CO \longrightarrow CH_3OCO$$

$$H + CH_3OCO \longrightarrow CH_3OCHO$$

Dimethyl Ether:

$$H + CH_2 \longrightarrow CH_3^*$$

$$CH_3^* + H_2CO \longrightarrow CH_3OCH_2$$

$$H + CH_3OCH_2 \longrightarrow CH_3OCH_3$$

All three of the above COMs have been detected in presterllar cores including L1689B, L1544, and B1-b and in the cold outer envelopes of protostars [6].

In order to propose possible COM reactions, it is necessary to know what molecules exist in the ISM. This requires two things. Firstly that a radio telescope can detect

the signal from the radical or neutral molecule, and secondly that there is a database containing an expansive collection of laboratory rotational spectra of radical and neutral molecules. To date, of the molecules detected and identified, roughly 30% are radicals [9], and of these detected radicals all are either linear carbon chains or contain fewer than 6 atoms. This lack of detection of complex radicals is likely due to a lack of laboratory spectra, making their identification especially challenging. It is possible to determine the rotational spectra directly using microwave spectroscopy or indirectly from the rotational fine structure in the vibrational bands of the molecule using rovibrational spectroscopy, but these spectroscopy methods have severe limitations. To solve this problem, a new laboratory technique for wideband indirect rotational spectroscopy has been created which will allow for the determination of accurate rest frequencies of the transitions of complex radicals within the detection bands of the radio telescope ALMA, allowing for their detection. With the knowledge of what molecules are in the ISM, cluster experiments on these molecules can be performed giving insights into the formation processes of COMs.

This thesis covers three general projects that aim to fill some of the gaps mentioned above and ultimately shed some light on the formation of life using various spectroscopic techniques. The first project performed utilized a visible-ultraviolet laser pulsed field ionization photoion detection method to perform two ion molecule reactions, discussed in detail in chapter 2. While these two ion molecule reactions may not be of direct astronomical interest, the general findings of these may be applicable to astrochemistry. The next project introduces a new technique, referred to as Noise Immune Cavity Enhanced Optical Heterodyne Zeeman Modulation Spectroscopy (NICE-OHZMS), and discusses the early trouble shooting involved in getting this technique set up. This technique is being realized by adding Zeeman modulation to an existing mid-infrared sub-Doppler spectrometer producing a radical-selective, Doppler free spectrometer. This is covered in chapters 3 through 5. The final project, covered in chapter 6, looks at the photoionization by synchrotron vacuum ultraviolet light of gas phase clusters of alcohols and water to learn how water in the icy mantles surrounding dust grains alters the reactivity of embedded alcohols. The three alcohols examined are 1,2-propylene glycol, 1,3-propylene glycol, and

ethylene glycol. The findings are contrasted with an earlier investigation studying the photoionization of glycerol water clusters.

# Chapter 2

# Ion Molecule Work

## 2.1 Introduction

As was discussed briefly in the introduction chapter, ion-molecule reactions may be involved in the formation of small molecules in the ISM due to these reactions typically being barrierless and exothermic. These reactions also play a role in catalysis [10], water splitting [11] and other energy and environmental fields.

To make a contribution to the understanding of these reactions, two such reactions were performed between vanadium cations and two small neutral molecules, water and methane. The vanadium cation was prepared into the following quantum spin-orbit electronic states: $V^+[a^5D_J(J = 0, 2)], V^+[a^5F_J(J = 1, 2)], V^+[a^3F_J(J = 2, 3)]$. Through these reactions, the absolute integral cross section for the reaction was determined as a function of the center of mass collision energy as well as the electronic state of the vanadium cation.

Methane is an important molecule both on Earth and in space. In space, it is found on Mars and Titan and is an important carbon containing ice in comets and interstellar space [12]. On Earth, it is the most widespread alkane, is a major green-house gas [13], and is an intermediate in the production of methylene radical, methanol, and $H_2$ [14]. The current process for methane activation and reaction to other hydrocarbons is via the Fischer-Tropsch process [14] which is expensive and energy intensive. New, less expensive and energy intensive pathways for methane activation are desired and could be applied to

larger hydrocarbons. Transition metals have been shown to efficiently break the C-C and C-H bonds of alkanes [15] making these useful for alkane activation. Cross sections and reaction pathways for vanadium cation methane ion-molecule reactions have been studied previously by the Armentrout group [16], but the electronic state of the vanadium cation was unknown. Through our experiments, the activation of methane as a function of spin orbit electronic state of the vanadium cation can be better understood. Building off of these results, better activation pathways for both methane and larger alkanes can be developed.

Another important molecule is $H_2$, which is an ideal energy carrier. Current production of $H_2$ is through water splitting, but this is costly as it uses trace-metal catalysts. Using non-trace metals, such as transition metals, would provide a lower cost method for this production [17]. By reacting water with vanadium cation prepared into a specific spin orbit electronic state, the effect the state the cation has upon the reactivity water can be better understood and this knowledge can be applied to producing better catalysts.

The instrument used for these ion-molecule reactions as well as the results of these reactions are discussed in this chapter.

### 2.1.1 Ion-Molecule Instrument

A schematic of the ion-molecule instrument is shown in figure 2.1. The instrument, which

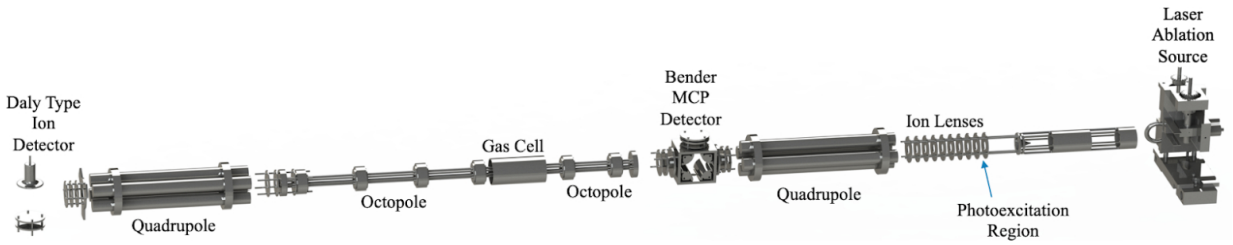


Figure 2.1. A schematic of the ion-molecule instrument used to determine the absolute integral reaction cross sections for the reactions between vanadium cation and the small neutral molecules water and methane.

will be analyzed from right to left following the direction of molecular beam travel, begins with the laser ablation source. Here, a plasma of neutral and charged vanadium atoms are generated through ablation of a vanadium metal rod by the second harmonic (532 nm) of a

pulsed Nd:YAG laser. These vanadium atoms are seeded into a pulsed supersonic Helium molecular beam moving through the instrument. At this point only neutral vanadium cations are desired, these will later be ionized into a set spin orbit quantum state, and so the charged vanadium atoms are removed by a DC electric field. The neutral vanadium molecular beam enters the photoexcitation region, which is the region containing ion lenses, shown in figure 2.2. In this region the neutral vanadium is excited into the desired

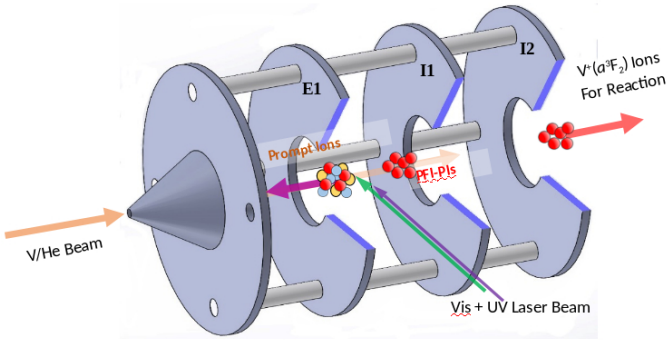


Figure 2.2. A schematic of the photoexcitation region showing the three key ion lenses, E1, I1, I2, and the ions formed, unwanted prompt ions and the desired pulsed field ionization photo ions (PFI-PI).

spin orbit state and then ionized. This process begins with excitation by a visible laser, $\omega 1$, followed by excitation by a UV laser, $\omega 2$, into a high-n ($n \geq 60$) Rydberg state, as outlined in figure 2.3. Both laser beams are produced by dye lasers which are pumped by

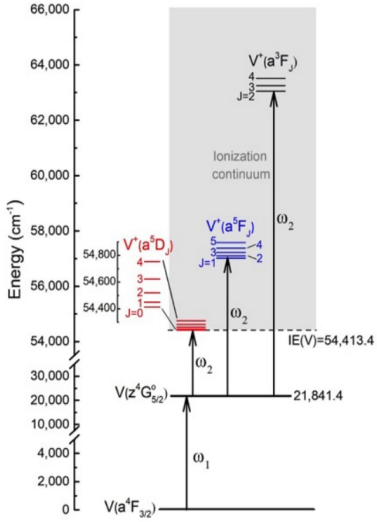


Figure 2.3. A schematic of the laser excitation of neutral Vanadium into the selected spin orbit states. $\omega 1$ is the visible laser and $\omega 2$ is the UV laser.

pulsed Nd:YAG lasers. Through this excitation process, some of the Vanadium atoms are ionized without state selection, referred to as prompt ions. To separate these ions from the neutral excited vanadium atoms, a 2.0 eV pulsed electric field is applied to ion lens, E1, for 2 $\mu$s. This electric field retards the prompt ions thereby creating separate clumps of neutral excited vanadium atoms followed by charged ions. 10 ns after turning off the electric field from E1 a second 41.7 eV pulsed electric field is applied for 0.75 $\mu$s to ion lens I1. This electric field pulsed-field ionizes the excited neutral vanadium atoms producing electronic state selected vanadium cations in the following quantum spin-orbit coupled J states $V^+[a^5D_J(J = 0, 2)], V^+[a^5F_J(J = 1, 2)], V^+[a^3F_J(J = 2, 3)]$. The duration of this electric field is determined by the amount of time it takes for the ions to leave the photoexcitation (PEX) region. The electric field must be turned off before these ions leave the PEX region so that all state selected ions have the same kinetic energy. The prompt ions have a lower kinetic energy than the state selected ions, due to the first electric field, and so lag behind the state selected ions. By applying a small positive DC voltage to ion lens I2 after the state selected ions have passed through this ion lens, the prompt ions are removed from the molecular beam. Now only spin orbit electronic state selected vanadium cations, moving with a specific laboratory kinetic energy ($E_{lab}$), and helium atoms are contained in the molecular beam. This beam is directed through the quadrupole mass filter, which acts as an ion focusing lens, into the MCP detector, which basically acts as another quadrupole, through the radio frequency octopole ion guide which contains the reaction gas cell filled with the neutral molecule of interest, either water or methane. The typical pressure of the neutral molecules inside the gas cell is $2.0x10^{-4}$ Torr and is monitored by an MKS Baratron. The laboratory kinetic energy is converted into center of mass collision energy ($E_{CM}$) using equation (2.1)

$$E_{CM} = E_{lab}[\frac{M}{m^+ + M}] \tag{2.1}$$

where M is the mass of the neutral molecule and $m^+$ is the mass of the vanadium cation. All reactions are performed in the center of mass collision energy range 0.1 - 10.0 eV. The products from the reaction gas cell are directed through another quadrupole mass filter and directed to an ion detection system composed of a modified Daly Type Ion Detector.

This detector has been modified by replacing the photomultiplier-scintillation assembly with a dual set of microchannel plate ion detectors. From this, the absolute integral reaction cross sections, $\sigma$, were determined by comparing the intensities of the reactant vanadium cation with those of the products using a thin target ion-neutral scattering scheme, as shown in equation (2.2),

$$\sigma = \frac{kT}{Pl} ln(\frac{I+i}{I}) \tag{2.2}$$

where k is the Boltzmann constant, T is temperature in Kelvin, P is the pressure of the neutral reactant in the gas cell, l is the length of the gas cell, I is the intensity of the reactant vanadium cation, and i is the intensity of the product.

### 2.1.2 Vanadium Cation plus Water Results

For the reactions between state selected vanadium cations and neutral water molecules three product channels were observed for each vanadium reactant state and are $VO^+ + H_2$, $VH^+ + OH$, and $VOH^+ + H$, resulting in a total of nine reactions. These reactions are shown in equations (2.3) through (2.11) accompanied by the threshold energies of reaction ($E_T$) for some of the reactions.

$$V^+(a^3F_J) + H_2O \rightarrow VO^+ + H_2, E_T = -2.0 \pm 0.1\, eV \tag{2.3}$$

$$V^+(a^5F_J) + H_2O \rightarrow VO^+ + H_2, E_T = -1.2 \pm 0.1\, eV \tag{2.4}$$

$$V^+(a^5D_J) + H_2O \rightarrow VO^+ + H_2, E_T = -0.9 \pm 0.1\, eV \tag{2.5}$$

$$V^+(a^3F_J) + H_2O \rightarrow VH^+ + OH, E_T = 1.3 \pm 0.1\, eV \tag{2.6}$$

$$V^+(a^5F_J) + H_2O \rightarrow VH^+ + OH, E_T = 2.2 \pm 0.1\, eV \tag{2.7}$$

$$V^+(a^5D_J) + H_2O \rightarrow VH^+ + OH, E_T = 2.6 \pm 0.1\, eV \tag{2.8}$$

$$V^+(a^3F_J) + H_2O \rightarrow VOH^+ + H \tag{2.9}$$

$$V^+(a^5F_J) + H_2O \rightarrow VOH^+ + H, E_T = 0.4 \pm 0.1 eV \tag{2.10}$$

$$V^+(a^5D_J) + H_2O \rightarrow VOH^+ + H, E_T = 1.0 \pm 0.1\, eV \tag{2.11}$$

As an example of the obtained mass spectra, two of the experimentally obtained mass spectra are shown in figure 2.4 for the reaction $V^+(a^3F_2) + H_2O$. Similar mass spectra were observed for the reactions between the other spin orbit electronic states of vanadium and water. Panel a shows the mass spectrum of $V^+(a^3F_2)$ and panel b shows the mass

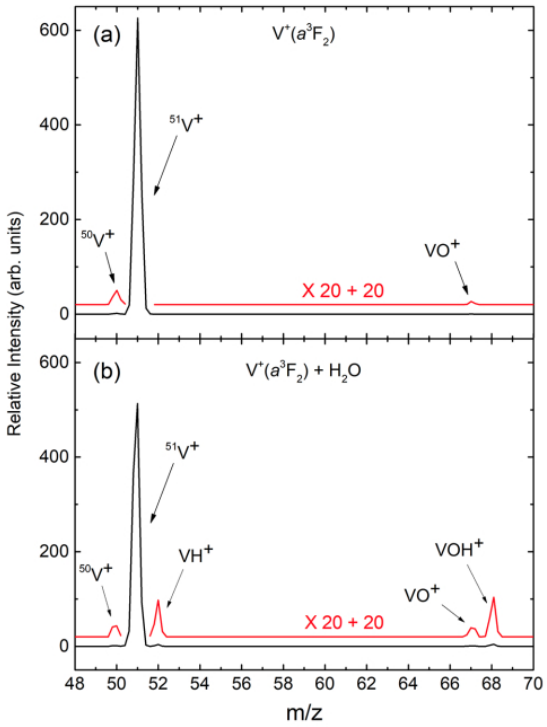


Figure 2.4. Panel a shows the mass spectrum of $V^+(a^3F_2)$ and panel b shows the mass spectrum of $V^+(a^3F_2) + H_2O$ products. To better show the peaks, a portion of the spectrum, shown in red, has been magnified (x20) and shifted up by 20.

spectrum of the product channels of the reaction $V^+(a^3F_2) + H_2O$. Panel a was obtained with an empty gas cell while panel b was obtained by filling the gas cell with water to a pressure of $2.0x10^{-4}$ Torr. Panel b has 2 peaks more than panel a indicating the production of the two products, $VH^+$ at m/z = 52 and $VOH^+$ at m/z = 68, formed through the reaction. The increased height of the $VO^+$ peak indicates that this is also a product of the reaction. The intensities of the two vanadium cation peaks, shown in both spectra at m/z = 50 and 51, are consistent with the natural abundance of the two most abundant isotopes of vanadium.

From these reactions, the absolute integral cross sections were determined as a func-

tion of center of mass energy and are shown in figure 2.5 with different curves for the reactants prepared with different spin multiplicity. Based upon the cross sections, it can

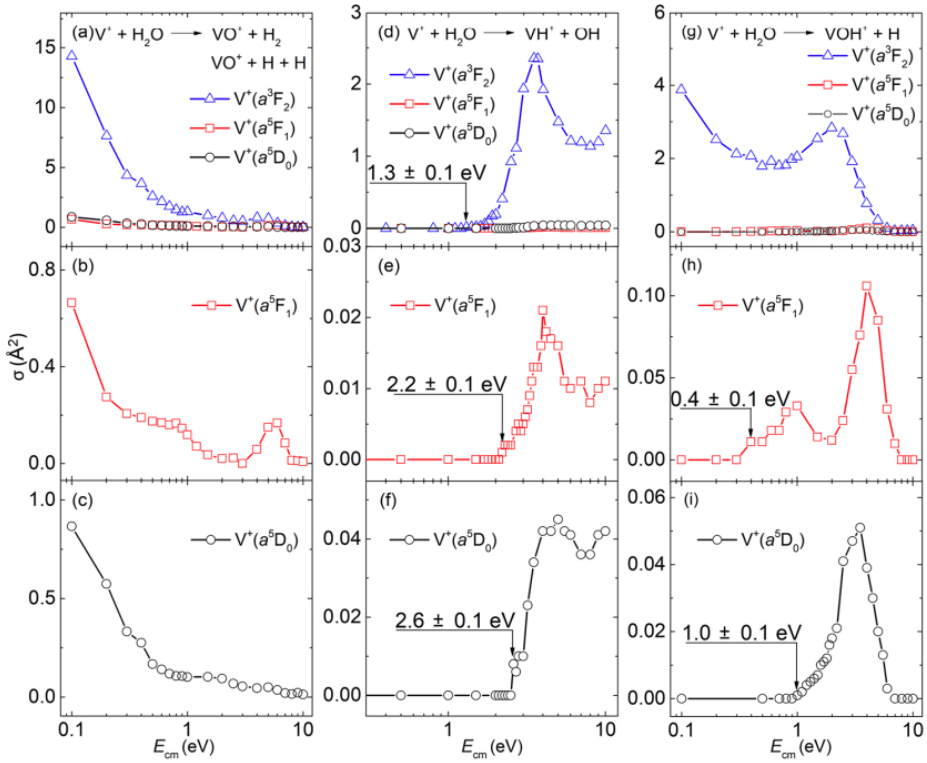


Figure 2.5. The absolute integral cross sections from the reactions between $V^+(a^3F_2, a^5F_1, a^5D_0)$ and water forming the three product channels, $VO^+, VH^+, VOH^+$. These were observed in the $E_{CM}$ range 0.1 - 10.0 eV.

be determined if the reaction is exothermic as in figure 2.5 panels a through c, and blue line in g, where the cross section decreases with increasing $E_{CM}$, or endothermic as in figure 2.5 panels d through f and h and i, where the cross section increases with increasing $E_{CM}$. The results of the exothermic reactions follow the Langevin-Gioumousis-Stevenson (LGS) orbiting model, which would indicate that the reactions are governed by attractive potential energy surfaces occurring through reaction complex measurements at low $E_{CM}$.

In the case of the endothermic reactions, $E_T$ was determined based upon the $E_{CM}$ threshold, and found to be positive. Given that the exothermic reactions do not have distinct $E_{CM}$ thresholds, $E_T$ was determined based upon the known 0 K heats of formation of the chemical species involved as well as the dissociation energy for the products. The determined $E_T$ values are found to be consistent with the known electronic energy spacings

of the spin-orbit electronic states $a^5D_0$, $a^5F_1$, and $a^3F_2$.

As can be seen in figure 2.5 panels a, d, and g, the cross sections for the products produced by the triplet vanadium cation are at least four orders of magnitude higher than those produced by the quintet vanadium cations. The heightened reactivity of triplet vanadium cation with water indicates a spin multiplicity preference. There is also a product preference given that the cross section for $VO^+$ is larger than for the other products. The proposed reaction mechanism in the heat of formation scale is shown in figure 2.6. The reactants are shown on the left, with black indicating a quintet state and

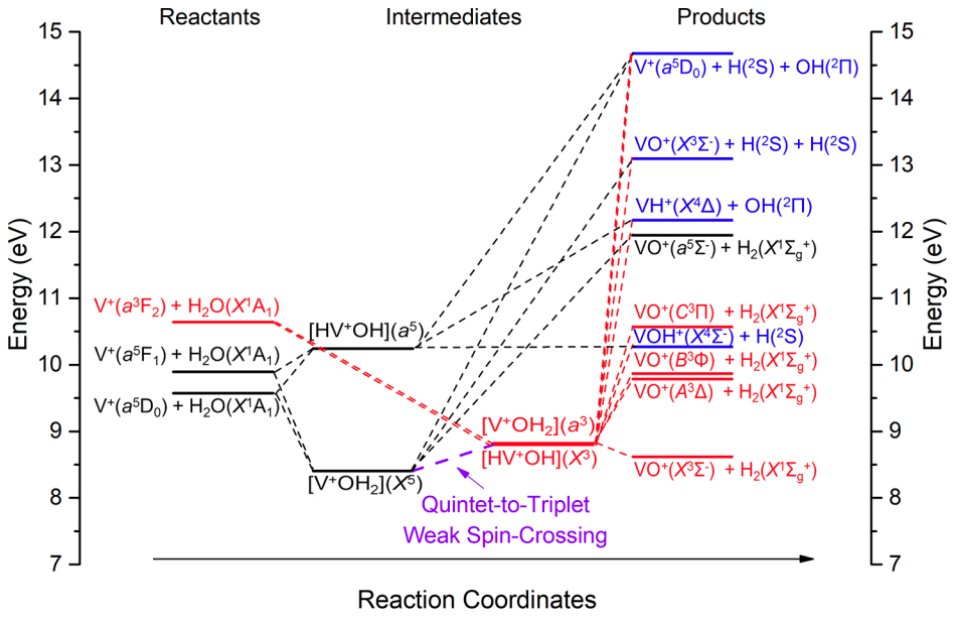


Figure 2.6. The proposed reaction pathways for the $V^+ + H_2O$ reaction system. In the left column are the reactants, in the middle are the quintet and triplet intermediates, and on the right are the possible product channels. Red indicates a triplet state, black a quintet state, and blue indicates a product that could form from either a triplet or quintet state.

red indicating a triplet state. In the middle are the intermediates, with the same coloring as the reactants. On the right are the proposed products. Here, as before, red indicates a triplet state and black a quintet state. Blue indicates that the product could form from either a triplet or quintet reactant. Given that $VO^+$ is the dominant species and the energetics of the excited states are known, excited $VO^+$ products are included in figure 2.6.

Two reaction intermediates are proposed to play a role in the vanadium cation water reaction, each of these in both quintet and triplet states. The energy positions of these intermediates were calculated using DFT. The $C_{2V}$ $V^+OH_2$ intermediate is thought to form through a charge-dipole and induced dipole attraction between $V^+$ and $H_2O$. Since the oxygen in water has a net negative charge, the $V^+$ ion will preferentially attack the oxygen atom rather than the hydrogens of water forming a strong, 6 eV [18], $VO^+$ bond, weakening the OH bond of the $V^+OH_2$ intermediate and forming the product $VO^+ + H_2$.

The $HV^+OH$ intermediate is thought to form when $V^+$ is inserted into one of the OH bonds of a water molecule. This forms two new bonds, $V^+ - H$ and $V^+ - OH$, which are both energetically favorable, giving rise to the $VH^+$ and $VOH^+$ products.

In figure 2.5 panel a and somewhat in panels b and c it can be seen that $VO^+$ is preferentially formed over $VH^+$ and $VOH^+$. $V^+OH_2(a^5)$ being 2.3 eV lower in energy than $HV^+OH(X^5)$ and forming $VO^+$ could potentially explain some of the preference for $VO^+$, but given that $VO^+(z^5\Sigma^-)$ is over 2 eV above the quintet vanadium reactants this reaction is not favored. In order to form the lower energy triplet $VO^+$ from a quintet product, a quintet-to-triplet spin crossing would be needed, and this is clearly a weak crossing given the low cross sections in panels b and c. Given all this, the formation of the products from the quintet reactants is not favorable when compared with the triplet reactant. Reactant $V^+(a^3F_2)$ forms the triplet intermediates without preference since both are at similar energies. From there, these intermediates can form the three triplet products, with much higher cross sections (panels a, d, g) than the products formed from the quintet reactants. This favored formation of product with the same spin as the reactant indicates that total electron spin conservation is highly favored in this reaction.

The reactant vanadium cations were not only prepared with different spin multiplies, but also in different J states. Product cross section curves obtained from reactants with different J states, $V^+(a^3F_{2,3}, a^5F_{1,2}, a^5D_{0,2})$, are shown in figure 2.7. No J-state dependence is found and therefor no J-state effects on the chemical reactivity of $V^+$ with $H_2O$, as indicated by the almost identical curves for the same products formed from reactants with different J-states. This means that there is a weak coupling between electron spin

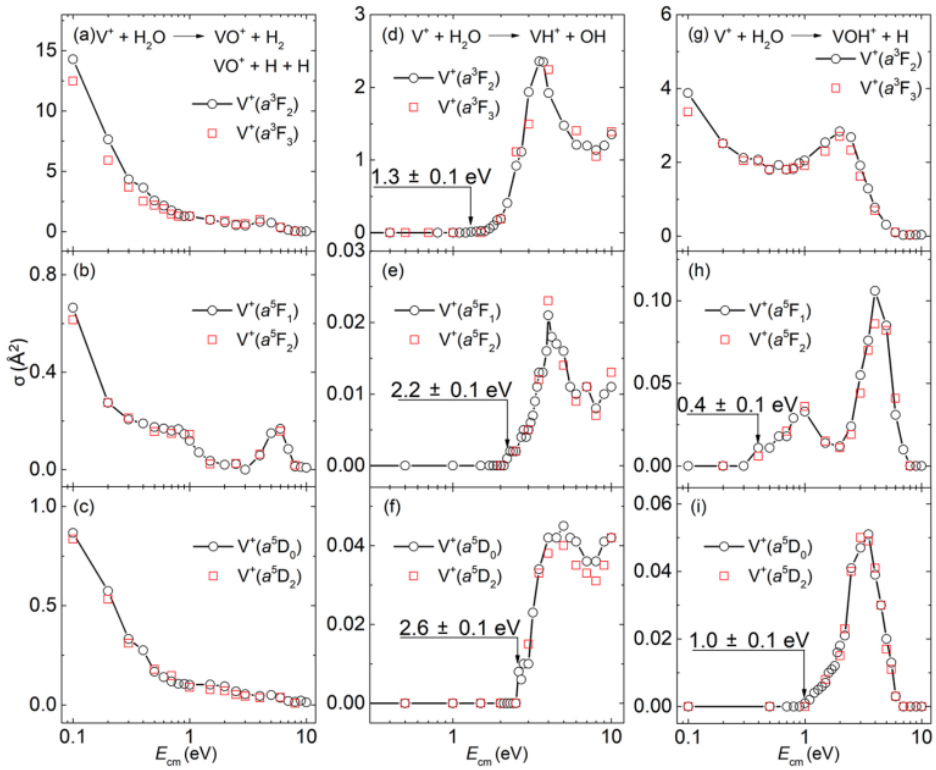


Figure 2.7. Cross section curves for the three products produced from the reaction between $V^+(a^3F_{2,3}, a^5F_{1,2}, a^5D_{0,2})$ and $H_2O$. These curves indicate no J-state dependence for this reaction.

and orbital angular momenta in $V^+$.

The difference in reactivity between the various electronic states of vanadium cation is therefore attributed to the difference in electron spin or multiplicity rather than J state [19]. The findings of no J-state dependence and a weak quintet-to-triplet spin crossing are consistent with the results from the previously performed reaction between quantum electronic state selected $V^+$ and $D_2$ [20] and $CO_2$ [21].

### 2.1.3 Vanadium Cation plus Methane Results

Similar to the vanadium cation plus water reaction, the absolute integral cross sections for the reaction between $V^+[a^5D_J(J = 0, 2), a^5F_J(J = 1, 2), a^3F_J(J = 2, 3)]$ and methane were determined in the center-of-mass collision energy range ($E_{CM}$) 0.1 to 10.0 eV. The three observed product channels are $VH^+ + CH_3$, $VCH_2^+ + H_2$, and $VCH_3^+ + H$. Formation reactions for the ground state vanadium cation are shown in reactions (2.12) through (2.14), the excited states ($V^+[a^5D_J(J = 2), a^5F_J(J = 1, 2), a^3F_J(J = 2, 3)]$) would un-

dergo similar reactions to form these products.

$$V^+(a^5D_0) + CH_4(X^1A_1) \rightarrow VH^+(X^4\Delta) + CH_3(X^2A_2"), E_T = 1.9 \pm 0.1\, eV \quad (2.12)$$

$$V^+(a^5D_0) + CH_4(X^1A_1) \rightarrow VCH_2^+(X^3A_1) + H_2(X^1\Sigma_g^+), E_T = 1.2 \pm 0.1\, eV \quad (2.13)$$

$$V^+(a^5D_0) + CH_4(X^1A_1) \rightarrow VCH_3^+(X^4B_1) + H(^2S_{1/2}), E_T = 1.8 \pm 0.1\, eV \quad (2.14)$$

The apparent threshold energies of reaction ($E_T$) are determined either directly or indirectly by $E_{CM}$ threshold measurements. As is indicated by the positive $E_T$, reactions (2.12) through (2.14) are endothermic. Two of the mass spectra, taken with $E_{CM} = 2.0eV$, are shown in figure 2.8. Similar mass spectra were obtained for the other spin orbit electronic states of vanadium.

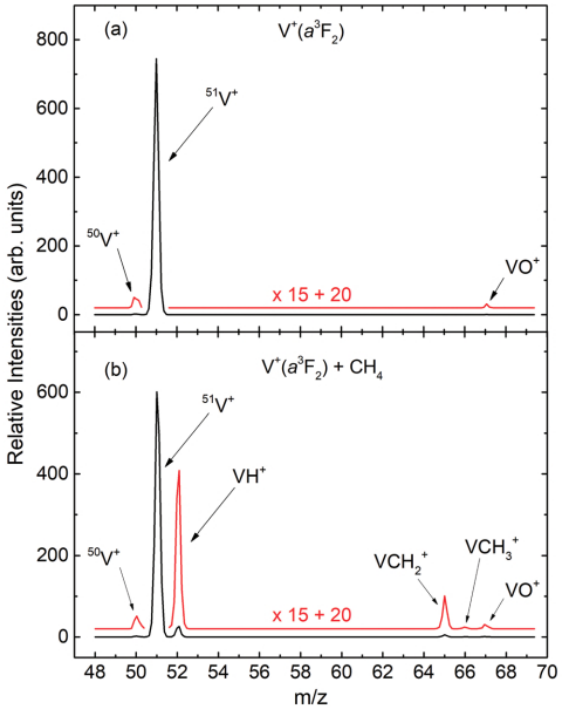


Figure 2.8. Panel a shows the mass spectrum of $V^+(a^3F_2)$ and panel b shows the mass spectrum of $V^+(a^3F_2) + CH_4$ products. To better show the peaks, a portion of the spectrum, shown in red, has been magnified (x15) and shifted up by 20.

Panel a shows the mass spectrum of $V^+(a^3F_2)$ and panel b shows the mass spectrum of the product channels for the reaction $V^+(a^3F_2) + CH_4$. Panel a was obtained with an empty gas cell while panel b was obtained by filling the gas cell with methane to a

pressure of $2.0x10^{-4}$ Torr. In panel a, three ion peaks are observed and are assigned to $^{50}V^+$ with m/z = 50, $^{51}V^+$ with m/z = 51, and $VO^+$ with m/z = 67. The intensities of the vanadium cation ion peaks are consistent with the natural abundances of these vanadium isotopes. The six ion peaks seen in panel b are attributed to $^{50}V^+$ with m/z = 50, $^{51}V^+$ with m/z = 51, $VH^+$ with m/z = 52, $VCH_2^+$ with m/z = 65, $VCH_3^+$ with m/z = 66, and $VO^+$ with m/z = 67. Note that there is no peak for the formation of $VCH^+$ ion. $VCH_4^+$ has the same m/z value as $VO^+$, but given that the intensities of $VO^+$ in panels a and b are similar, this peak in panel b can be attributed to $VO^+$ forming through a reaction between reactant $V^+$ and trace $O_2$ or $H_2O$.

The absolute integral cross sections for the observed products determined as a function of the center of mass energy are shown in figure 2.9 for reactants prepared with different spin multiplicities. The cross section for $VCH_3^+$ produced by $V^+(a^5F_1) + CH_4$ is below the detection limit and so no cross section curve for this product was obtained. For

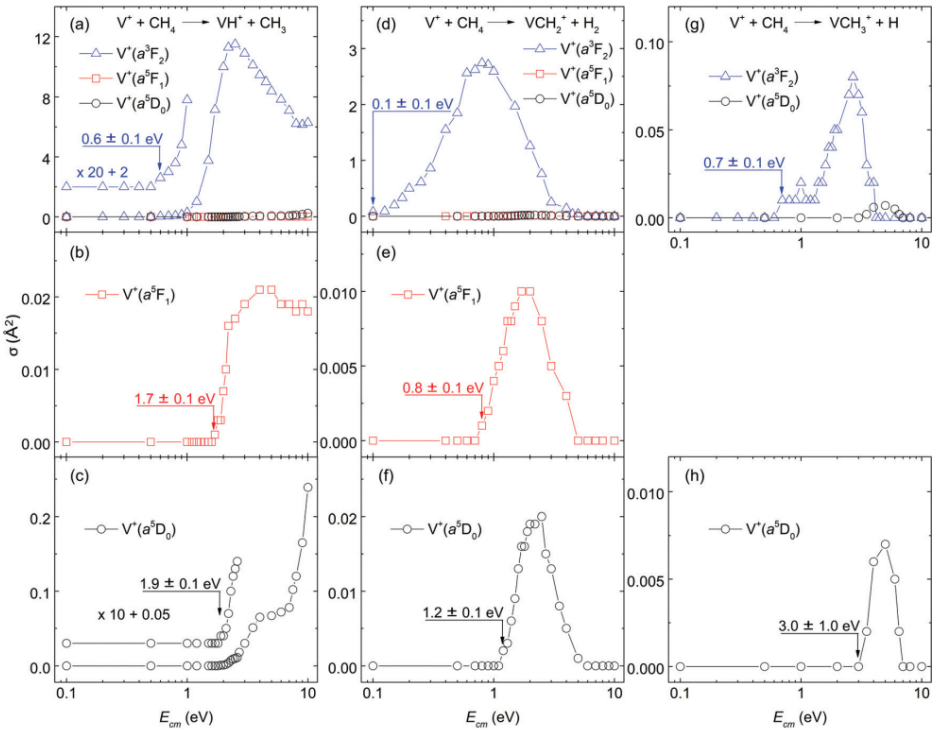


Figure 2.9. The absolute integral cross sections from the reactions between $V^+(a^3F_2, a^5F_1, a^5D_0)$ and methane forming the three product channels, $VH^+, VCH_2^+, VCH_3^+$. These were observed in the $E_{CM}$ range 0.1 - 10.0 eV. Panels b, c, e, f, h show magnified views of some of the cross section curves.

this reaction, all product channels are endothermic, as indicated by the cross section increasing with increasing $E_{CM}$ to a point where it then may start to decrease. As the cross section curves show, the initial state of the vanadium cation makes a huge difference in the reactivity and size of the cross section. The triplet reactant ion, $V^+(a^3F_2)$, is substantially more reactive than the quintet reactant ions, $V^+(a^5D_0, a^5F_1)$. This trend is rationalized by conservation of total electron spin, just as it was with the vanadium cation water reaction. The proposed reaction mechanism in the heat of formation scale for the $V^+ + CH_4$ reaction system is shown in figure 2.10.

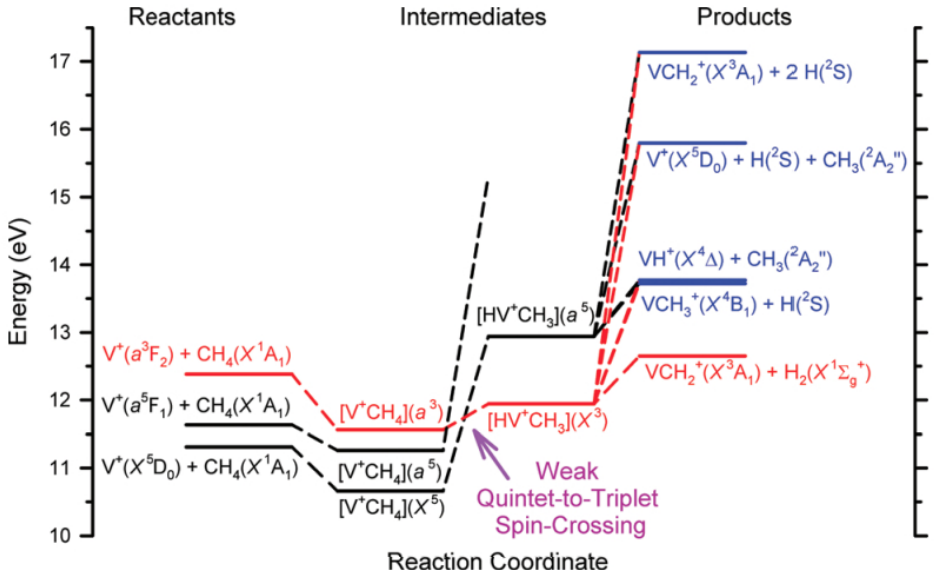


Figure 2.10. The proposed reaction pathways for the $V^+ + CH_4$ reaction system. In the left column are the reactants, in the middle are the quintet and triplet intermediates, and on the right are the possible product channels. Red indicates a triplet state, black a quintet state, and blue indicates a product that could form from either a triplet or quintet state.

The reactants are shown on the left, with black indicating a quintet state and red indicating a triplet state. In the middle are the intermediates, following the same coloring scheme as the reactants. On the right are the product channels, $VH^+(X^4\Delta) + CH_3(X^2A_2")$, $VCH_2^+(X^3A_1) + H_2(X^1\Sigma_g^+)$, $VCH_3^+(X^4B_1) + H(^2S_{1/2})$ for the reaction $V^+ + CH_4$ as well as the dissociative product channels, $V^+(X^5D_0) + CH_3(X^2A_2") + H(^2S_{1/2}$ and $VCH_2^+(X^3A_1) + 2H(^2S_{1/2})$. The red product indicates it can only form form a triplet. All other products are shown in blue indicating that they can form from both triplet and

quintet reactants.

The two proposed intermediates, $V^+CH_4$ and $HVCH_3^+$, can both form in quintet as well as triplet states. The $V^+CH_4$ intermediate is expected to rearrange into the inserted $HVCH_3^+$ intermediate due to $V^+ - H$ having a much weaker bond dissociation energy than $H - CH_3$. Both triplet intermediates are at a lower energy than the triplet reactant $V^+(a^3F_2) + CH_4$ that forms them. This results in an exothermic reaction requiring no electron spin flipping. The quintet reactants can form a quintet inserted intermediate, thereby conserving total electron spin, but this intermediate is 1.6 eV higher in energy than the ground state quintet vanadium cation so will be an endothermic reaction. In order for the quintet reactants to form the triplet product, a quintet to triplet spin-crossing would be required, making this unfavorable. Both intermediates can form in either the triplet or quintet states. Focusing on the triplet intermediate, this intermediate can either form from the triplet reactant or the quintet reactant, though this would require a quintet-to-triplet spin crossing which is weak. On top of spin crossing, both quintet states are lower in energy than the triplet intermediate, meaning this pathway has very low reactivity. The triplet reactant is higher in energy than the triplet intermediates and would require no spin crossing so this is the dominant mechanism for the product channel $VCH_2^+(X^3A_0)$. This is further supported by panels d, e, and f of figure 2.9, which shows a much larger cross section curve for the triplet reactant, blue curve in panel d. $VH^+$ and $VCH_3^+$ can form from the quintet intermediate, $[HV^+CH_3](a^5)$, without a quintet-to-triplet spin crossing if the $E_{CM}$ is high enough to form this intermediate. This can be seen in figure 2.9 panels b, c, and h where cross section starts to increase as $E_{CM}$ increases. At very high $E_{CM}$ there is a general trend of decreasing cross section. This is most noticeable for $VCH_2^+$ and $VCH_3^+$, panels d through h, where the cross section decreases to 0, but can also be seen in $VH^+$ panels a and b. This trend is attributed to the collision induced dissociation product channel, shown in reaction (2.15), occurring at $E_{CM} \geq 4.482$ eV, as well as the dissociation of excited $VH^+, VCH_2^+, CH_3^+$.

$$V^+(a^5D_0) + CH_4(X^1A_1) \rightarrow V^+(a^5D_0) + CH_3(X^2A_2") + H(^2S_{1/2}), E_0 = 4.482 \pm 0.001\, eV \tag{2.15}$$

$VCH_2^+$ may also dissociate into $VH^+$ explaining the higher cross sections for $VH^+$ compared with the other products as well as the threshold $E_{CM}$ for $VH^+$ being around the $E_{CM}$ where $VCH_2^+$ starts to decrease.

In order to see if the J-state played a role in the reactivity of the reactant vanadium cation with methane, these cations were prepared into different J states. Product cross section curves obtained from reactants with different J states, $V^+(a^3F_{2,3}, a^5F_{1,2}, a^5D_{0,2})$, are shown in figure 2.11. Just as in the $V^+ + CH_4$ reaction, no J-state dependence is found

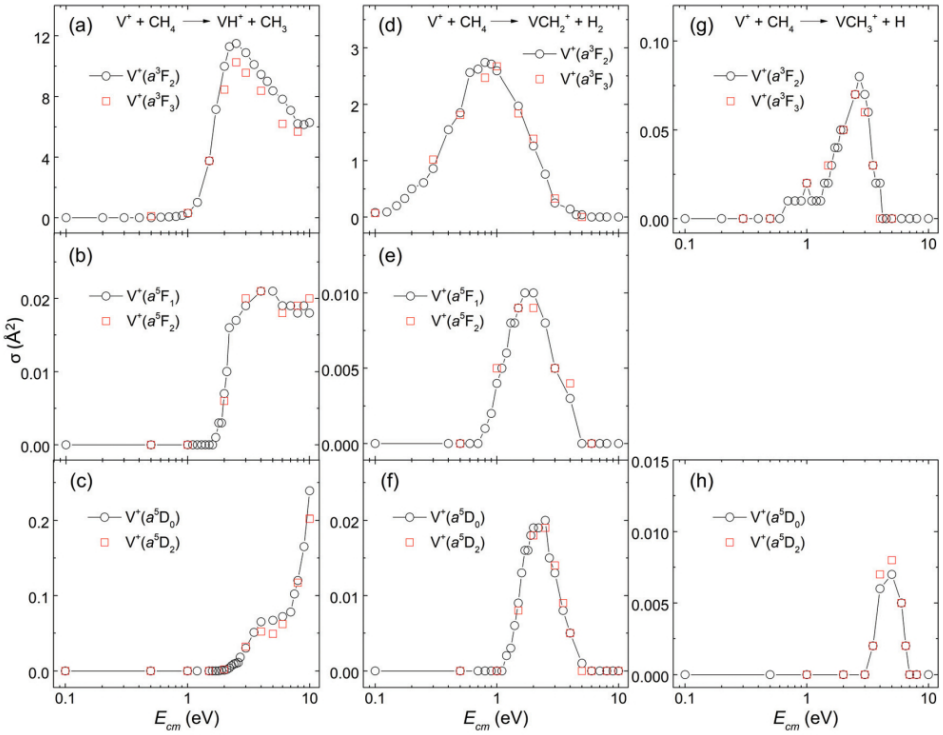


Figure 2.11. Cross section curves for the three products produced from the reaction between $V^+(a^3F_{2,3}, a^5F_{1,2}, a^5D_{0,2})$ and $CH_4$). These curves indicate no J-state dependence for this reaction.

and therefore no J-state effects on the chemical reactivity of $V^+$ with $CH_4$, as indicated by the almost identical curves for the same products formed from reactants with different J-states. This means that there is a weak coupling between electron spin and orbital angular momenta in $V^+$.

The difference in reactivity between the various electronic states of vanadium cation is therefore attributed to the difference in electron spin or multiplicity rather than J state [22].

The findings of no J-state dependence and a weak quintet-to-triplet spin crossing are consistent with the results from the previously performed reaction between quantum electronic state selected $V^+H_2O$ [19].

### 2.1.4 Conclusions

Reactions between vanadium cation, prepared into the quantum spin-orbit states $a^5D_{0,2}$, $a^5F_{1,2}$, $a^3F_{2,3}$, with water and methane, separately, were performed in the center of mass collision energy range 0.1 to 10.0 eV. For the vanadium cation water reactions, the three product channels $VO^+ + H_2, VH^+ + OH$, and $VOH^+ + H_2O$ were identified. For the reaction between vanadium cation and methane, the three product channels $VH^+ + CH_3, VCH_2^+ + H_2$ and $VCH^+ + H$ were identified.

In both reactions, the triplet state, $a^3F_{2,3}$, was found to be more reactive than the quintet states, $a^5D_{0,2}, a^5F_{1,2}$, which is attributed to a weak quintet-to-triplet spin crossing mechanism and therefor a favoring of conservation of total electron spin. In the vanadium cation methane reaction, an inserted intermediate $HV^+CH_3$ also favored the triplet state. The distinct pathways for the various electronic states is attributed to weak spin-orbit coupling.

In both reactions, viable pathways to form $H_2$ were shown providing insight into designing more effective catalyst for $H_2$ formation as well as $CH_4$ activation. This work is discussed in detail in the published papers given in references [19] and [22].

# Chapter 3

# Zeeman Modulation applied to Noise Immune Cavity Enhanced Optical Heterodyne Molecular Spectroscopy (NICE-OHMS)

## 3.1 Introduction

Ion-molecule reactions can explain the formation of small molecules found in the ISM, but they alone cannot form complex organic molecules (COMs). [7] Radicals, which make up about 30% of the known molecules in space, act as probes providing information about the chemical and physical conditions of the environments they come from. They are also thought to play a key role in the production of COMs [9]. In order to better understand the reactions that occurred to form COMs, it is necessary to know what radicals exist in space. While some radicals have been identified using radio telescopes such as the Atacama Large Millimeter/submillimeter Array (ALMA), all have either been linear carbon chains or have contained fewer than 6 atoms. Without the identification of complex radicals it is difficult to propose plausible radical reactions. This lack of identification of radicals in space stems from the lack of reliable laboratory spectra of complex radicals, due to the difficulty of obtaining such spectra. Laboratory detection of radicals is made difficult for a variety of reasons. These challenges begin with the difficulty

involved in producing radicals and continues from there with issues of radical reactivity and radical spectra detection. The production of radicals can occur through various methods. For gas phase spectroscopy, such as that done for astrochemical applications, useful production methods are UV photolysis, shown in reaction (3.1), where a bond is broken by UV light [23], discharge, where an electric current passes through a gas forming a plasma, and abstraction, where a bond is broken by an existing radical.

$$\mathrm{X{-}Y} \xrightarrow{\mathrm{h}\nu} \mathrm{X}^{\bullet} + \mathrm{Y}^{\bullet} \tag{3.1}$$

In the process of producing radicals, unwanted species, such as hot radicals and ions, are produced and unreacted precursor is leftover. In order to selectively determine the spectra of only the radicals, it is necessary to have a radical selection process that discriminates the spectra of radicals from those of other species. Detecting the spectra of radicals is made all the more difficult by the short lifetime of radicals and the unpaired electron which causes spin-rotation interactions and fine structure splitting resulting in complex spectral patterns.

The common spectroscopy techniques currently available to determine the rotational spectra of radicals are pure rotational spectroscopy and rovibrational/rovibronic spectroscopy. These techniques have certain advantages, but also disadvantages.

Pure rotational spectroscopy, performed using microwave radiation, is intrinsically selective, very precise and accurate, and produces spectra with narrow linewidths. The search for spectral lines begins in the centimeter band looking for transitions between low-N rotational levels, where N represents the rotational angular momentum quantum number. The transitions are predicted by ab intio electronic structure calculations, which may be costly and time-consuming. Searches for radicals predicted in low-abundance to be in space are best performed at high frequency, high N transitions, to exploit the sensitivity of radio telescopes such as ALMA. To attain this high frequency data by extrapolating data from low frequency transitions leads to uncertainty on the order of tens of MHz. The best way to observe transitions at high frequency is to span multiple frequency octaves. Most instruments do not have the capability to cover multiple frequency octaves so multiple instruments are needed and these instruments are often housed at different

laboratories increasing the difficulty in obtaining spectra. As an example of this, the beta cyanovinyl radical, shown in figure 3.1, which is thought to be a possible precursor for pyridine, has been experimentally detected in the centimeter band region through its rotational transitions up to N = 4. In order to search for this radical in space using ALMAs band 6, with a frequency range of 211 through 275GHz, transitions with N = 15 - 20, would be required. It is not possible to reliably predict these experimental transitions using the existing laboratory data taken at low N [24].

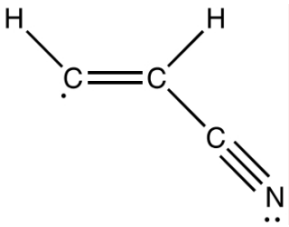


Figure 3.1. Cyanovinyl Radical

With high enough resolution, each line in the vibrational spectrum of a molecule contains many closely spaced components, due to rotational transitions accompanying the vibrational transitions and so the rotational spectrum of a radical can be indirectly determined from this rovibrational spectroscopy. Similarly to rovibrational spectroscopy, rovibronic spectroscopy indirectly determines the vibrational and rotational spectra of the molecule from the fine structure in the electronic bands.

These spectroscopy techniques can cover a large frequency range thereby covering a wide range of rotational levels with a single instrument, but along with this increased frequency range comes Doppler broadening, which is the broadening of spectral lines occurring when a radiation source is moving towards or away from the observer causing a frequency shift in the radiation [25]. At infrared wavelengths, those used for rovibrational spectroscopy, the linewidths are Doppler broadened to greater than 200 MHz, which greatly lowers the precision and accuracy of the rest frequencies and therefore the usefulness of these measurements, such as in the case of astronomical identification, which cannot be done given the high uncertainty. Because of these limitations traditional rovibrational spectroscopy is not useful as a means for indirect rotational spectroscopy.

Given these difficulties and the necessity to determine laboratory spectra and from

this rest frequencies of radicals, a new technique, called Noise Immune Cavity Enhanced Optical Heterodyne Zeeman Modulation Spectroscopy (NICE-OHZMS), has been developed. The technique allows for the selective determination of the rovibrational spectra of radicals and from that the rotational transition frequencies of radicals without the limitation of conventional infrared and microwave spectroscopy, but with the advantages of both of these types of spectroscopy. This is accomplished by applying Zeeman modulation to the existing technique noise immune cavity enhanced optical heterodyne molecular spectroscopy, NICE-OHMS. By doing this, a single instrument has been created that can determine the rest frequencies of radicals through this new Doppler free rovibrational spectroscopy technique with sub-MHz accuracy and precision.

At its heart, this technique is a laser absorption spectroscopy technique which detects the absorption and dispersion of light when it interacts with molecules, and in this case radicals. The rate of absorption and dispersion is governed by the energy density of the light, $\rho$, the population of molecules in the correct energy configuration, $N_1$, and the Einstein $B_{12}$ coefficient, as outlined in equation (3.2) [25]

$$(\frac{dN_1}{dt})_{abs} = N_1 B_{12} \rho \tag{3.2}$$

The energy transition that occurs when light and a radical interact is determined by the wavelength of the light. When infrared light radiates upon a molecule, a vibrational transition occurs. The vibrational energy levels are broken up into rotational energy levels which, if the laser has high enough resolution, allows for rotational vibrational, or rovibrational, transitions to occur. Rovibrational transisitons are seen with the NICE-OHZMS technique because the laser used is an infrared laser with high enough resolution.

This technique is being realized by modifying an existing instrument that was previously used to determine the rovibrational spectra of ions, among them $H_3^+$, through the technique noise immune cavity enhanced optical heterodyne velocity modulation spectroscopy (NICE-OHVMS). NICE-OHVMS is a highly sensitive, accurate and precise sub-doppler, ion-selective spectroscopy technique that is the result of the combination of velocity modulation and the technique noise-immune cavity enhanced optical heterodyne molecular spectroscopy (NICE-OHMS).

For the remainder of this chapter, the NICE-OHZMS technique will be analyzed by dissecting the parts of the technique. This analysis will start by understanding the pieces making up the technique NICE-OHMS. These pieces are cavity enhancement, optical heterodyne molecular spectroscopy, and noise immunity. By adding an extra layer of modulation, spectral discrimination can be obtained. This was initially done with the technique NICE-OHVMS, which added velocity modulation to NICE-OHMS creating an ion-neutral discriminator technique. The NICE-OHVMS technique is discussed to better understand the idea of adding an extra layer of modulation. At the end of the chapter, zeeman modulation is introduced and added to NICE-OHMS giving a full understanding of the new technique NICE-OHZMS.

With the technique understood, the parts of the instrument built for the NICE-OHZMS technique will be walked through in detail in chapter 4. Finally, in chapter 5, the results of the initial testing of the instrument are presented.

## 3.2 Noise Immune Cavity Enhanced Optical Heterodyne Molecular Spectroscopy

The Noise Immune Cavity Enhanced Optical Heterodyne Molecular Spectroscopy or NICE-OHMS technique was first realized by June Ye in 1998 [26]. This is a highly sensitive laser based absorption technique which is best understood by dissecting the name.

### 3.2.1 Cavity Enhancement

Cavity enhancement, or CE, is accomplished when the generated plasma or gas of interest is contained between two mirrors forming a cavity. This increases the length of interaction between the light and the ions thereby enhancing intracavity power and increasing the signal and precision. Thinking of the Beer-Lambert Law, given in equation (3.3),

$$A = \epsilon l c, \tag{3.3}$$

where A is the absorption of the sample, epsilon is the molar absorption coefficient of the sample, l is the path length, and c is the concentration of the sample, [25] it can

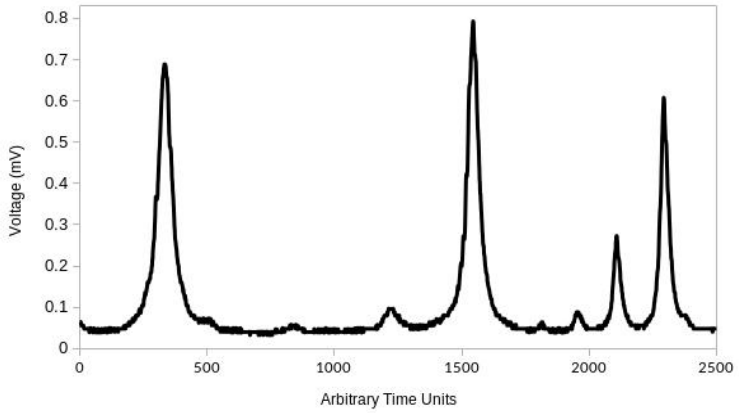


Figure 3.2. The transmission of the NICE-OHZMS cavity with a mirror reflectivity of 99±0.3%. Multiple modes are shown, the finesse for the largest fringes, $TEM_0 0$ mode, is around 166.

be seen that by placing the sample between two mirrors the path length over which the laser light and sample can interact is increased and therefore the absorption of the sample is increased. This increased path length, without needing to make the cell meters long, greatly enhances this technique allowing for the determination of absorption spectra for samples with a low concentration, such as radicals produced in a plasma. The cavity mirrors not only increase the path length, but also control the amount of light that is lost, or leaks out of the cavity. Inside the cavity, the optical energy is stored at resonant wavelengths forming fringes. The higher the reflectivity of the mirrors, the lower the loss and the narrower the resonances relative to the frequency distance. The finesse is determined by dividing the free spectral range, or the fundamental mode spacing, by the bandwidth, or full width at half-maximum. The transmission of the NICE-OHZMS cavity with a mirror reflectivity of 99 ± 0.3% is shown in figure 3.2, where the finesse for the largest fringes, the $TEM_{00}$ mode, is about 166. Cavity enhancement is a technique used in other types of spectroscopy such as cavity enhanced absorption spectroscopy and cavity ring down spectroscopy.

### 3.2.2 Optical Heterodyne Molecular Spectroscopy

Cavity enhancement is combined with frequency modulation, or FM, to reduce 1/f noise and then detected via optical heterodyne detection, hence the optical heterodyne portion

of the technique name, which demodulates the signal. Frequency modulation combined with heterodyne detection was first introduced by Gary Bjorklund in 1979 as a way to perform wavelength modulation via phase modulation rather than by using tunable laser sources. No spectral resolution is lost in the absorption or dispersion spectra when using a phase modulator rather than a cw dye laser and the absorption and dispersion features can be detected separately by adjusting the radio frequency beat signals phase and amplitude. [1] At a very basic level, modulation buries information or signal in a carrier frequency. In the case of frequency modulation, the carrier frequency is the pump laser, which is a ytterbium doped fiber laser, discussed in the instrument chapter. This is phase modulated by the EOM, which is driven by a radio frequency, referred to as the heterodyne frequency, resulting in 2 side bands, $180^o$ out of phase, on either side of the pump. The side bands and the pump are passed through the cavity interacting with the molecule of interest. [1] The molecules absorption coefficient and index of refraction at the given carrier frequency attenuates the amplitude, symbolized by $\delta$, and shifts the phase, symbolized by $\phi$, of the modulated beam. This modulated beam hits a photodetector producing an electrical signal which contains two rf beat notes, one from each of the side bands beating against the carrier buried in the modulation frequency. If the side bands were equally affected by the absorption of the molecule, either in amplitude or phase, then the two beat notes would cancel resulting in no rf signal. If the side bands were unequally affected by the absorption of the molecule then the beat notes would not cancel resulting in an rf signal, which is highly sensitive to changes in the phase and amplitude. In order to extract the signal from the modulation frequency, the modulated beam is mixed with the rf heterodyne frequency, keeping only the DC component resulting in the demodulated absorption and dispersion signals, shown in equation (3.4), where $\beta$ is the modulation index, $\Omega$ is the modulation frequency, or heterodyne frequency, and $E_0$ is the amplitude of the carrier frequency.

$$I(t) = \frac{cE_0^2}{8\pi} e^{-2\delta}[1 - \Delta\delta(\beta)cos\Omega t + \Delta\phi(\beta)sin\Omega t] \tag{3.4}$$

Assuming the heterodyne frequency, $\Omega$, is large compared with the frequency of the carrier, the in-phase component, cosine component of equation (3.4), is proportional to the

absorption of the molecule of interest while the quadrature component, sine component in equation (3.4), is proportional to the dispersion of that molecule. These signals are shown in figure 3.3. [1] By encoding the signal in a radio frequency, which is a region

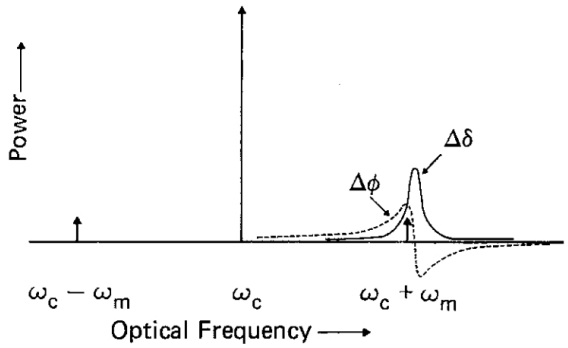


Figure 3.3. This figure, taken from G.C. Bjorklund's Frequency Modulation (FM) Spectroscopy paper [1], shows the absorption and dispersion occurring when a molecule has interacted with a modulated beam and the the rf signal has been demodulated leaving behind these signals.

with low noise, the noise level is reduced thereby increasing the signal-to-noise ratio. On top of that, by burying the signal at high frequency, 1/f noise is minimized leaving only white noise.

When frequency modulation is performed using an electro-optic modulator, such as is done in the NICE-OHZMS technique, a second type of undesired non-zero amplitude modulation called residual amplitude modulation (RAM) is imprinted onto the laser. It has been found that the amount of RAM can be adjusted by the optical layout and removed by a feedback control system [27].

Frequency modulation is a common noise removal technique used in radio broadcasting as well as molecular absorption measurements [28] and laser frequency stabilization [29].

### 3.2.3 Noise Immunity

By combining cavity enhancement with frequency modulation and optical heterodyne detection a technique is realized which is immune to the amplitude noise caused by the jitter of the laser frequency compared with the cavity resonance frequency. This noise immunity occurs only if the 2 FM sidebands and carrier, making up the FM triplet, are on resonance with the cavity, meaning the modulation frequency is an integer multiple

of the free spectral range of the cavity. If the modulation frequency is off of the free spectral range, then the FM triplet samples the same portion of the cavity mode resulting in no beat signal. By implementing frequency modulation with cavity enhancement, this technique does not suffer from lock noise like previous techniques such as Cavity-Enhanced Velocity Modulation Spectroscopy (CE-VMS) did.

Cavity-enhancement was first combined with frequency modulation by Jun Ye, et. al in 1998. They performed ultrasensitive molecular overtone spectroscopy on HCCD, HCCH, and $CO_2$ molecules to obtain their sub-Doppler overtone resonances [26]. Since then, this technique has been modified in many ways with some examples being the addition of a mid-Infrared OPO [30] and the addition of a fiber-coupled single sideband modulator to better control laser frequency [31].

Since this initial combination of cavity enhancement and frequency modulation, this highly sensitive technique has been combined with additional modulation to discriminate the spectra of certain molecules from spectra of others. This was first done to determine the spectra of ions, with the technique NICE-OHVMS. The NICE-OHVMS technique has similarities to our technique, NICE-OHZMS, so NICE-OHVMS will be analyzed below before getting into NICE-OHZMS.

## 3.3 Noise Immune Cavity Enhanced Optical Heterodyne Velocity Modulation Spectroscopy

Noise Immune Cavity Enhanced Optical Heterodyne Velocity Modulation Spectroscopy or NICE-OHVMS adds an extra layer of modulation, specifically velocity modulation, to NICE-OHMS to create a technique that can discriminate between the spectra of ions and all other molecules.

Velocity modulation was first performed by Richard Saykally in 1983 and became a leading ion spectroscopy technique because of its ability to discriminate between ions and much more abundant neutral molecules in plasmas. This technique is performed by applying an alternating electric field, which is assumed to be sinusoidal and has a magnitude given by E, to a glow discharge inside a cell. This produces a cathode at one

end of the cell and an anode at the other with an AC plasma in between, containing ions and other species. In most situations, only the ions are attracted to the cathode, while the other species in the plasma are unaffected by the polarity of the cell. While there have been cases where the neutral molecules are affected by the AC electric field, these will be ignored in this discussion because they are uncommon. Since the plasma is produced by an AC electric field, the polarity of the cell changes and the average velocity of the ions changes with the same frequency, given in equation (3.5), while the average velocity of the neutral molecules remains unchanged. In equation (3.5) K represents the ion mobility.

$$v(t) = KEcos(2\pi t) \tag{3.5}$$

When a laser beam passes through the cell, the absorption profiles of the ions undergo an oscillatory Doppler shift, at the frequency of the AC electric field. The Doppler shifted velocity is given in equation (3.6), where the velocity modulation amplitude is represented by $v_{ma}$ and the shift over time in the line center results in the transformation given in (3.7) where $\chi(v)$ represents the frequency detuning due to transition frequency shifting.

$$v_{mod}(t) = v_{ma}cos(2\pi t) \tag{3.6}$$

$$\chi(v,t) \rightarrow \chi(v + v_{mod}(t)) \tag{3.7}$$

The detected Doppler shifted signal is demodulated resulting in the spectrum of the ion given in equation (3.8) where the demodulation was done using a Fourier filter, as is done in a lock-in amplifier.

$$\chi_{vms}(v) = \int_{-1/2}^{1/2} \chi(v,t)cos(2\pi t)dt \tag{3.8}$$

One downside to this technique is the derivative-like line shape, which makes it difficult to determine accurately the line strengths, line widths and the modulation depths. [32]

The technique NICE-OHVMS was first demonstrated by Professor Benjamin McCall's group in 2011. By performing velocity modulation along with frequency modulation inside a cavity, resulting in a very long path length and reduced noise, it is possible to obtain spectra with sub-Doppler resolution and ion-neutral discrimination. [33]

Following the lead of adding an extra layer of modulation to NICE-OHMS to discriminately look at one type of molecule, we decided to design a technique that could

discriminate between the spectra of radicals and closed shell molecules by combining Zeeman modulation with NICE-OHMS.

## 3.4 Noise Immune Cavity Enhanced Optical Heterodyne Zeeman Modulation Spectroscopy

By combining Zeeman modulation with NICE-OHMS the technique Noise Immune Cavity Enhanced Optical Heterodyne Zeeman Modulation Spectroscopy or NICE-OHZMS was created allowing for the determination of Doppler-free rovibrational transitions of radicals with sub-MHz precision and accuracy and without contamination of much more abundant closed shell molecules. The accuracy of the rovibrational transitions results from the frequency comb and the precision results from lamb dips in the absorption spectra. A lamb dip, shown pictorially in figure 3.4, results when the incident radiation is tuned to the absorption peak. In this case, the only molecules that can absorb the beam are those with velocity in the direction perpendicular to the travel of the beam, or molecules with no Doppler shift. Upon first pass of the light, these non-Doppler shifted molecules absorb the light causing excitation and so fewer molecules absorb light upon subsequent passes of the light resulting in a reduction in intensity. If the radiation frequency is higher than the absorption peak, then the light is only absorbed by molecules traveling with the correct velocity parallel to the light. This will occur on both the first and second passes of the light resulting in a double dose of absorption. The highest absorption, seen in figure 3.4, occurs at frequencies right above and below the absorption peak and less absorption occurs at the exact frequency of the peak [25].

Through the use of combination differences and Hamiltonian fitting the pure rotational rest frequencies of the radical of interest can be determined from the rovibrational transitions.

The technique has been realized by adding an AC audio amplified solenoid to the typical NICE-OHMS set up producing an alternating magnetic field and therefore Zeeman modulation.

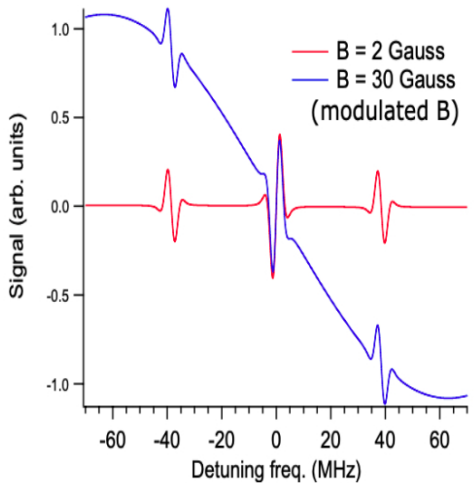


Figure 3.4. This figure shows simulated Zeeman modulation spectra with magnetic fields of 2 and 30 Gauss. Each spectrum contains 3 lamb dips (shown in the middle and on either side of this middle lamb dip). The lamb dip allows for the precise determination of the transition frequency.

### 3.4.1 Zeeman Modulation

Zeeman modulation utilizes the Zeeman effect to bury a signal in a carrier frequency, which in this case is the frequency driving a magnetic field. When a magnetic dipole moment is exposed to an external magnetic field, $B$, the energy of that magnetic moment is altered as shown in equation (3.9),

$$\delta E = -\mu_z B \tag{3.9}$$

where $\mu_z$ is the orbital angular momentum of an electron around the z-axis, given in equation (3.10).

$$\mu_z = -\frac{e\hbar}{2m_e} M_l = -\mu_B M_l \tag{3.10}$$

Here $\mu_B$ is the bohr magneton and $M_l$ is the quantum number for the state containing the electron. Equations (3.9) and (3.10) can be combined resulting in equation (3.11)

$$\delta E = \mu_B M_l B \tag{3.11}$$

which shows that the number of nondegenerate energy levels resulting from a degenerate energy level is determined by the $M_l$ value. If, for example, the electron is contained in a p orbital, with $M_l = -1, 0, 1$, then in the presence of a magnetic field the energy of the

three states would be that given in equation (3.12).

$$\delta E_1 = \mu_B B, \delta E_0 = 0, \delta E_{-1} = -\mu_B B \tag{3.12}$$

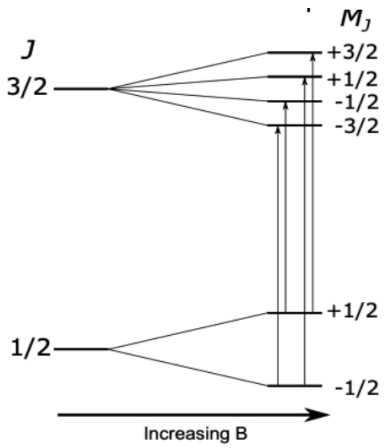


Figure 3.5. With the application of a magnetic field, the degenerate $M_J$ levels of the J = 0, 1 levels are Zeeman split, with the amount of splitting proportional to the magnetic field strength.

The Zeeman effect discussed above is the normal Zeeman effect. In actuality, the splitting due to the Zeeman effect is much more complicated because of the magnetic moment of the electron spin which also interacts with the external magnetic field resulting in the magnetic moment energy given in equation (3.13) where $g_L$ is the spin gyromagnetic ratio, S and L are the spin and orbital angular momentum vectors respectively and $M_J$ is the total angular momentum [25].

$$\delta E = \frac{e}{2m}(L + 2S)\dot{B} = g_L \mu_B M_J B \tag{3.13}$$

Figure 3.5 shows an example of Zeeman splitting of the J = 0 and 1 levels. When a magnetic field is applied, the previously degenerate $M_J$ components are split, with the splitting based upon the strength of the magnetic field.

If the magnetic field varies with time, as is the case in Zeeman modulation, the splitting of the energy levels will vary with the same frequency as the varying magnetic field thereby burying the absorption signal at the frequency of the varying magnetic field. This varying field will interact with the large magnetic moment of an open-shell molecule, or radical, thereby splitting the previously degenerate $M_J$ components of the J level, as is seen in

figure 3.5. The size of the splitting will vary with the strength of the magnetic field. Since closed shell molecules do not have a magnetic moment, they will be largely unaffected by the magnetic field and therefore the absorption of these species will not be modulated at the frequency of the magnetic field resulting in a radical selective spectroscopy technique.

Previous radical selective spectroscopy employing Zeeman based techniques has been performed through magnetic rotation (MR) spectroscopy [34], frequency modulation enhanced magnetic rotation (FM-MR) spectroscopy [35] and sideband optical-optical double resonance Zeeman (SOODRZ) spectroscopy [36]. Building off of these techniques, a Doppler free, highly sensitive, radical selective spectroscopy technique is being created through the combination of Zeeman modulation and the existing NICE-OHMS technique.

With the NICE-OHZMS technique fully understood, the instrument used for the technique will be dissected in chapter 4.

# Chapter 4

# Noise Immune Cavity Enhanced Optical Heterodyne Zeeman Modulation Spectroscopy (NICE-OHZMS) Instrument

The noise immune cavity enhanced optical heterodyne zeeman modulation spectroscopy instrument, shown in figure 4.1 is composed of a multitude of pieces and parts. To

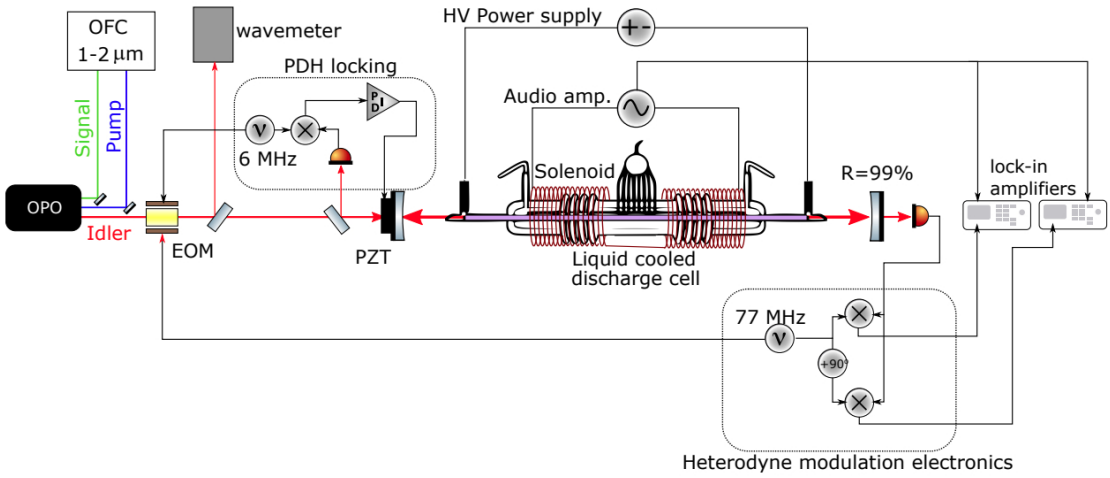


Figure 4.1. Shown here is a block diagram of the NICE-OHZMS instrument. Some abbreviations are as follows, OPO: optical parametric oscillator, OFC: optical frequency comb, EOM: electro-optic modulator, PDH: Pound Drevor Hall, PZT: piezoelectric transducer, HV: high voltage

better understand this instrument the pieces involved can be categorized into two main

categories, optical components and modulation components. The optical components are those involved in the general instrument layout and laser path while the modulation components are those involved in modulating the signal, so for the most part electronics. Each of these components will be discussed in detail in the following sections.

## 4.1 Optical Components

The optical components making up the laser light path are the laser, wavelength meter or wavemeter, cavity, detector, and the optical frequency comb. A schematic of these components is shown in figure 4.2.

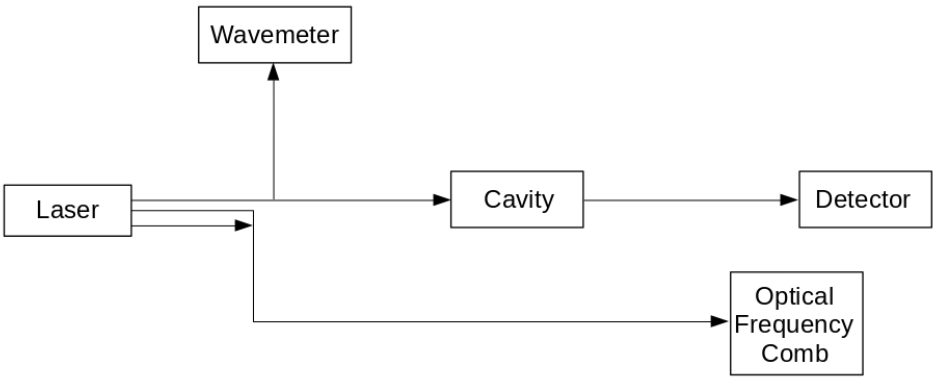


Figure 4.2. This schematic shows the general parts making up the optical components, the laser, wavemeter, cavity, detector, and optical frequency comb. The arrows between these components represent a laser beam.

The laser used for the experiments is an optical parametric oscillator (OPO) which is pumped by a continuous wave 1064 nm Ytterbium doped fiber seed laser (YDFL). This seed laser is a Koheras AdjustiK Y10 single frequency DFB fiber laser with a maximum output power of 10 mW, a line width of less than 70 kHz and piezo tuning of greater than 15 pm. The YDFL beam is sent through an acousto-optic modulator (AOM), then through an electro-optic modulator (EOM), and then through an IPG photonics fiber amplifier (model number: YAR-10K-1064-LP-SF, maximum power output = 10 W, spectral range 1060-1070 nm), before entering the OPO. Both the AOM and EOM will be discussed in detail in the modulation components section.

OPOs work by splitting a single laser beam into two tunable beams of lower energy

and therefore lower frequency as shown in equation (4.1) [37]

$$\nu_{pump} = \nu_{signal} + \nu_{idler} \tag{4.1}$$

and diagrammed in figure 4.3 [37] [38] .

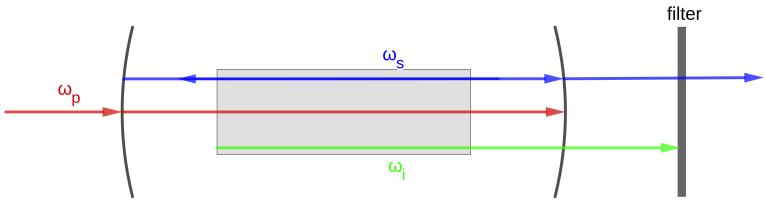


Figure 4.3. This figure shows a diagram of an OPO. The pump beam is split into two beams, the idler beam, which exits after 1 pass and the signal beam, which is resonant with the OPO cavity.

The output of the OPO is three beams, the two of lower energy referred to as the signal and idler beams, and the original pump beam. The spectrum of the beams coming out of the OPO is ultimately determined by the spectrum of the seed laser, which in this case is 1064 nm. The OPO used in this instrument is an Argos Model 2400 CW OPO, which is a single frequency model (M-type pzt) employing a periodically poled lithium niobate (PPLN) crystal. The OPO used is resonant with the signal beam and therefore the spectrum of the pump laser is imprinted onto the idler beam. By adjusting the phase matching conditions, namely the orientation and temperature of the PPLN crystal, the wavelength of the signal and therefore idler beams can be tuned [39]. This OPO has three different cavity modules which in total span the wavelengths 2.3 to 3.9 $\mu$m with a line width less than 1 MHz, a maximum tuning rate of 30 Hz, a beam quality of $TEM_{00}$, a power output greater than 1 Watt at all wavelengths, power stability less than 5% rms and a mode-hop-free tuning range of 50 GHz. [38]

The signal and pump beams from the OPO are sent into an FC1500 Menlo Systems optical frequency comb, which is used for frequency calibration. This femtosecond fiber laser frequency comb is composed of a mode locked Erbium fiber laser pumped by a mode-locked fiber ring laser with a center wavelength of 1560 nm. By beating the beam, either the signal or the pump, off of the comb teeth produced by the frequency comb, the

wavelength of the beam is determined. The frequency comb provides a means of adjusting the wavelength of the idler, such as by locking either the signal or pump to the comb.

At the most basic level, a frequency comb can be thought of as a ruler where each ruler line is a spectral line of known frequency formed by a laser, as shown in figure 4.4. At the

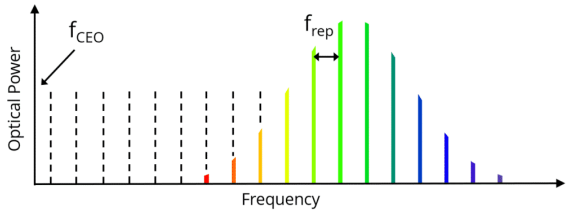


Figure 4.4. A frequency comb formed in the visible spectrum [2].

heart of our frequency comb is a mode locked laser, which fixes the phase between modes of the laser so that periodic constructive interference occurs resulting in a pulse train such as that shown in figure 4.5. Due to the speed of propagation of the pulse envelope,

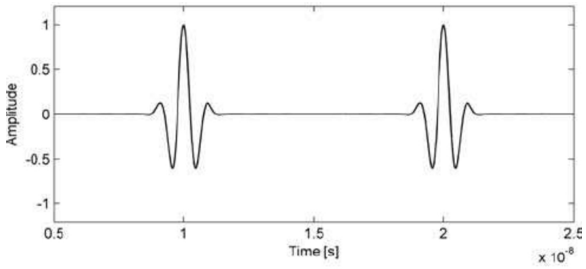


Figure 4.5. A pulse train formed by a mode locked laser [2].

A(t), being different from that of the carrier wave, which has a carrier frequency of $\omega_c$, after each round trip the pulse is shifted by the phase angle. The electric field of the wave outside the laser is given by equation (4.2), where $A_N$ is the Fourier amplitude component of A(t) and N is the mode number.

$$E(t) = A(t)e^{i\omega_c t} = \sum_{N=N_i}^{N_f} A_N e^{i\omega_N t}, \tag{4.2}$$

Based upon equation (4.2), it can be seen that the resulting spectrum from a mode locked laser is composed of spectral lines, or comb teeth, separated by the pulse repetition frequency, $\omega_r$, shown in figure 4.4. The carrier frequency, $\omega_c$, is not necessarily an integer

multiple of the pulse repetition frequency so the modes are shifted by an offset, m, between the values 100,000 and 1,000,000 thereby converting the frequencies $\omega_r$ and $\omega_0$ to optical frequencies $\omega_m$ as shown in equation (4.3). [2]

$$\omega_m = m\omega_r + \omega_0, \tag{4.3}$$

To stabilize the frequency comb, the spacing and comb offset are stabilized. The cavity length and the pump power are controlled to phase lock the repetition rate and the offset frequency. The 2100 nm part of the comb is frequency doubled and beat against the 1050 nm part of the comb to determine the offset frequency.

The idler from the OPO, which is ultimately used to interrogate the radical of interest, is sent into the cavity with a pick-off sent to the Bristol Instruments model 621 wavelength meter, which is used to determine the wavelength of the idler. The wavemeter contains a scanning Michelson interferometer which is calibrated using an internal class 2 laser. The length of one of the arms of the interferometer is adjusted and the power of laser light versus length of the arm is recorded by a photodetector and used to determine the wavelength of the idler beam. The accuracy of this wavemeter is 30 MHz, which allows for the constraining of $\delta$n of the pump and signal beams. [40]

The cavity, which is 2.336 m long, is composed of a liquid nitrogen cooled glass discharge cell with cavity mirrors on either side of this cell. The cell is filled with the gas phase radical of interest which is generated in a direct current discharge and cooled by liquid nitrogen to reduce the rotational partition function. The direct current discharge is produced by two electrodes which have a voltage applied between them. These electrodes are at the ends of a cell which is at low pressure to increase the mean free path of the gas molecules, and thereby the energy of the molecules before they collide with each other. The applied voltage between the electrodes causes a small number of the gas molecules to ionize as well as form radicals, which are the focus of this instrument [41]. To form our direct current discharge we use a reversible polarity regulated high voltage DC power supply (ET Series 2000 W). Half of the cell is surrounded by an ac audio amplifier driven solenoid which is used to generate the time varying magnetic field used for Zeeman modulation. The AC audio amplified solenoid is in house made with 16 AWG shielded wire

wrapped around a pvc pipe cut to fit around the glass cell, as shown in figure (7.1). It has 150 turns and is 22.1 cm long. Neither the pvc pipe nor the metal touch the glass cell.

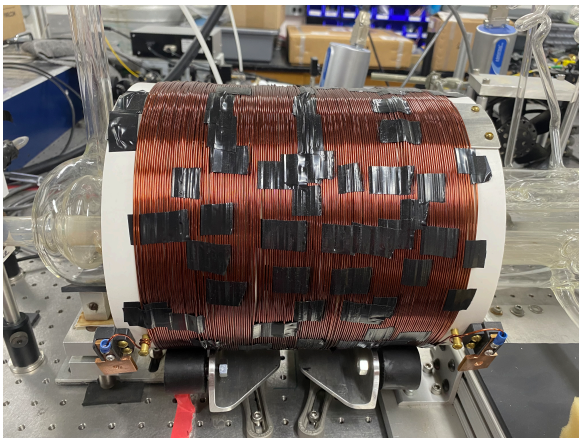

Figure 4.6. A picture of the AC audio amplified solenoid which produces the time varying magnetic field used in the NICE-OHZMS technique to discriminate the spectra of radicals from that of closed shell molecules.

The solenoid is driven by an amplified AC signal originating from a BK Precision 4 MHz Sweep Function Generator and amplified by a Series 7700 Techron Power Supply Amplifier. The field produced by the solenoid is coaxial with the plasma in the cavity and with the laser beam path, which results in a selection rule of $\Delta M_J = \pm 1$ and a splitting on the order of 1 MHz/Gauss. The produced time varying magnetic field results in the discrimination between the spectra of radicals and closed shell molecules in the NICE-OHZMS technique.

The cavity mirrors, on either end of the cell, are IR coated fused silica with 99(+0.5/-1)% reflection between the wavelengths 2600 and 3400 nm. This results in the light passing between the two mirrors many times producing a cavity enhanced system. These mirrors have a radius of curvature of 2 m and are plano-concave. When working with a plasma the cavity mirrors do not touch the cell, in an effort to keep them clean, but rather the glass cell has Brewster windows on either side. Each cavity mirror is mounted on a piezoelectric transducer, which allows for small adjustments to the cavity length to keep the cavity and laser beam locked. This locking occurs by implementing the Pound-Drever-Hall (PDH) technique, which will be discussed in detail in the modulation section.

The idler beam arrives at the cavity after traveling through a collection of three focus-

ing lenses referred to as the telescope. The goal of the telescope is to focus the beam to a point inside the cavity, a little bit before the middle of the cavity. The location and focal length of each lens is determined based upon the idler beam size and the ideal beam waist inside the cavity. Measuring the idler beam diameter presented too many challenges so instead the beam waist after the first telescope lens, which is a 10 cm focusing lens, was measured and found to be 0.0374 mm. Using the cavity length and the index of refraction of the mirrors, the ideal beam waist, $\omega$, at the center of the cavity was determined using equation (4.4)

$$R(x) = x[1 - (\frac{\pi\omega^2}{\lambda x})^2], \tag{4.4}$$

For the current cavity of length 2.336 m, the ideal beam waist is 0.9098 mm. Knowing both the starting point and ideal ending point, the position and focal length of the other two telescope mirrors were determined using ABCD matrices and Gaussian beam propagation. A schematic of the placement of the last two telescope lenses as well as the cavity mirror, all represented as vertical lines, is shown in figure 4.7.

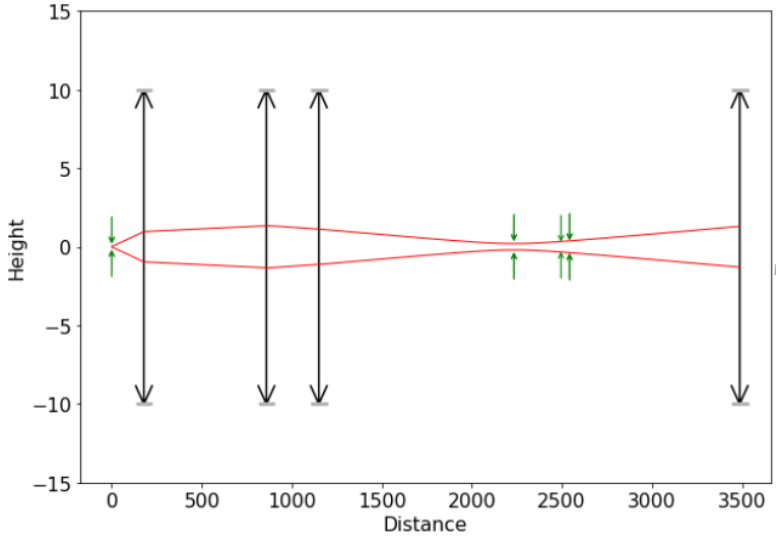


Figure 4.7. Here is an example of the output of a raytracing program used to determine the placement of the three telescope lenses. The vertical lines are the 2 telescope lenses and then the 2 cavity mirrors. The green arrows show focal points. The starting point is after the first telescope lens, 10cm focusing lens.

The beam exiting the cavity through the end mirror is detected by a mid-IR detector

(Boston Electronics Vigo PVI-4TE-6) which will be referred to as the transmission detector. This detector is the same as that used for the back reflection detection and both of these are photoconductor detectors made from Mercury Cadmium Telluride. [42]. More details on post detection processes and demodulation processes are in the modulation components section.

## 4.2 Modulation Components

The modulation components are those involved in frequency modulation or heterodyne detection and Pound-Drever-Hall (PDH) locking with a small amount of Zeeman modulation discussed. The electrical components will be described along with the techniques to better understand them.

In the case of frequency modulation, the carrier frequency is the pump laser, which is a 1064 nm ytterbium doped fiber laser, more details are contained in the previous section. This is phase modulated by the EOM, which is driven by a radio frequency, referred to as the heterodyne frequency, resulting in two side bands, $180^o$ out of phase, on either side of the pump. One set of sidebands is used for frequency modulation while the other is involved in PDH locking, which is discussed later. The workings of an EOM will be described briefly here before returning to the description of frequency modulation.

The EOM contains a Pockels cell which is a noncentrosymmetric crystal, meaning a crystal without a center of symmetry, with electrodes attached to it allowing for the application of alternating electric voltages [37]. The applied voltage alters the refractive index of the crystal so when a laser beam is sent through this crystal, side bands are applied to the carrier beam, in our case the pump. These side bands are $180^o$ out of phase with each other and at higher and lower frequencies than the pump.

The following math outlines the formation of side bands when a laser is sent through the EOM. The laser beam, before interacting with the EOM, is mathematically described as shown in equation (4.5) where $\omega$ represents the frequency of the laser beam.

$$E = \frac{E_0}{2} e^{-2\pi i \omega t} \tag{4.5}$$

To the EOM a sinusoidally varying potential voltage, whose frequency is represented by

$\Omega$ and amplitude is represented by $\beta$, is applied producing a laser beam described by equation (4.6) after passing through the EOM.

$$E = \frac{E_0}{2} e^{-2\pi i\omega t - i\beta \sin(2\pi\Omega t)} \tag{4.6}$$

Using the Jacobi-Angler expansion, which is a Bessel function, equation (4.6) can be written as shown in equation (4.7) where $J_j(\beta)$ is a $j^{th}$ order Bessel function.

$$E = \frac{E_0}{2} e^{i2\pi\omega t} \sum_{j=-\infty}^{\infty} J_j(\beta) e^{i2\pi j\Omega t} \tag{4.7}$$

Based upon this it can be seen that the result of passing the laser beam through the EOM with an applied voltage is a superposition of electromagnetic waves with frequencies equal to $\omega \pm j\Omega$ which show up as side bands on the carrier beam [43]. In the case of our instrument, two pairs of sidebands are created so $\Omega$ is either the heterodyne frequency, which is generated using a 0.1-1040 MHz Signal Generator (Hewlett Packard, 8657A), or the frequency for the PDH locking, generated by an Agilent (33120A) 15MHz Function/Arbitrary Waveform Generator. This signal and waveform are combined by a mini-circuits splitter (15542, 2FRSC-2050), acting as a mixer, and then sent to the EOM.

To implement frequency modulation, the phase modulated beam is passed through the cavity, of length L, interacting with the molecule of interest [1]. To ensure that all three components of the modulated beam, the two side bands and the carrier, make it into the cavity, the heterodyne frequency is set equal to the free spectral range, FSR, of the cavity. The free spectral range is determined by the constant separation distance between the longitudinal cavity modes, whose frequency can be determined by equation (4.8) [37].

$$\nu_m = \frac{m\nu}{2L} \tag{4.8}$$

The modulated beam is detected and demodulated at the heterodyne frequency. More details on frequency modulation are given in the NICE-OHMS chapter.

The second set of sidebands produced by the EOM are used for the PDH locking. In order for the cavity and idler to be on resonance, meaning a standing wave forms between the two cavity mirrors, the cavity length must be equal to the wavelength of light in the cavity times an integer, m, as shown in equation (4.9) [44].

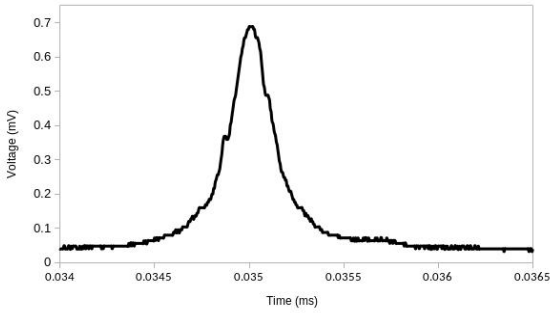


Figure 4.8. Cavity transmission fringe from the NICE-OHZMS instrument.

$$\lambda = \frac{2d}{m}, \tag{4.9}$$

When this requirement is met, transmission fringes form, such as that shown in figure 4.8 taken from the NICE-OHZMS instrument. Since the laser wavelength fluctuates, the Pound-Drever-Hall (PDH) locking technique is employed to keep the cavity and laser on resonance. To employ this technique it must be known if the laser and cavity are on resonance and if not, it must be determined in what direction to move the frequency in order to get back onto resonance. This can be accomplished using light that is reflected off of the first cavity mirror (never enters the cavity) as well as the light that leaks out of the mirror from inside the cavity. This light is detected by a mid-IR detector (Boston Electronics Vigo PVI-4TE-6), referred to as the back reflection detector. The signal, composed of the laser beam with sidebands created by the EOM and the Agilent (33120A) 15MHz Function/Arbitrary Waveform Generator, is then passed through a mini-circuits low pass filter (BLP-30+), through a mini-circuits amplifier (ZFL-500LN-BNC+) and then multiplied by the function produced by the Agilent 15MHz Function/Arbitrary (33120A) waveform generator using a mini-circuits mixer (ZFM-3). The mixing produces two products, a signal at DC and a signal at twice the modulation frequency. The signal at DC produces the derivative of the back reflected light, which is referred to as the Pound-Drever-Hall error signal [44]. An error signal, taken from the NICE-OHZMS instrument is shown in figure 4.9. An idealized error signal, taken from Eric Black's PDH paper [44], is shown in figure 4.10 for comparison.

This error signal is then passed through a low pass filter. By monitoring the error

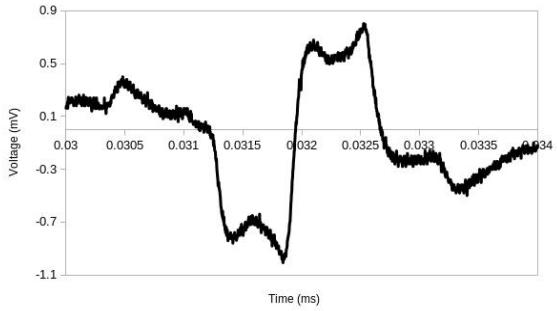


Figure 4.9. The Pound-Drever-Hall Error Signal from NICE-OHZMS instrument.

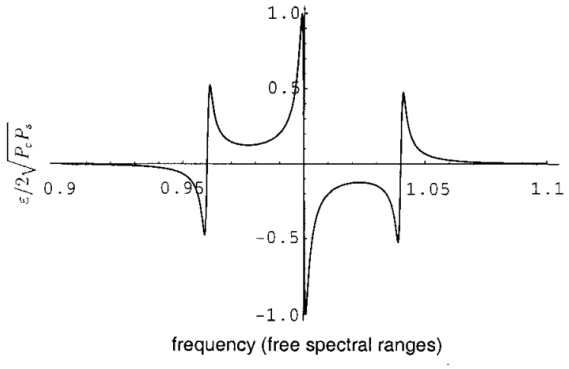


Figure 4.10. The Pound-Drever-Hall Error Signal, taken from Eric Blask's PDH paper.

signal with respect to frequency fluctuations, it can be determined which direction the frequency must be adjusted to get back onto resonance. This is done using a TEM Messtechnik GmbH LaseLock Box. The lase lock box attempts to hold the laser on resonance using proportional-integral-derivative (PID) control loops [45] which send fast corrections to the laser wavelength, through the AOM (discussed in the laser section), and slow corrections to the length of the cavity by adjusting the voltage applied to the piezo-electric transducers (pzt) mounted on the cavity mirrors. The control function performed can be described by equation (4.10) where $K_P$ represents the proportional term, $K_I$ represents the integral term, and $K_D$ represents the derivative term [45].

$$u(t) = K_p e(t) + K_I \int_0^t e(\tau)d\tau + K_D \frac{de(t)}{dt}, \tag{4.10}$$

The AOM is composed of a transparent crystal, which the laser beam is sent through, surrounded by a piezoelectric transducer (PZT), which is attached to a radio frequency driver. This causes sound waves, on the order of 100 MHz or 10 to 100 $\mu$m, to oscillate

through the crystal resulting in crystal strain and therefore a traveling index grating. The frequency of the laser beam going through the crystal experiences either an increase or decrease in wavelength proportional to the sound wave. These changes to the wavelength of the pump laser beam occur relatively quickly which aids in the process of holding the cavity and laser beam on resonance [46].

On the opposite end of the cavity, the NICE-OHZMS signal leaks out of the cavity and is detected by the transmission detector. This signal is then amplified, split to produce two signals 90 degrees out of phase with each other, and then mixed with the heterodyne frequency to demodulate the frequency modulated signal. The signal is still Zeeman modulated at this point and is demodulated by the lock-in amplifier. Two SR530 lock-in amplifiers (Standford research system), one for each signal, extract the desired absorption and dispersion signals, at a known frequency, from noise and amplify these signals and then demodulate them at the frequency used to drive the magnetic field. This frequency is generated by the BK Precision 4 MHz Sweep Function Generator which was used to drive the solenoid which produced the time varying magnetic field used for Zeeman modulation.

To understand the workings of a lock-in amplifier it will be walked through below using an arbitrary signal. A signal which ideally looks like that shown in equation (4.11), but in reality is buried in noise, $V_N$, so looks like that shown in equation (4.12), is sent into the input of the lock-in amplifier.

$$V(t) = V_0 \cos(\omega_0 t), \tag{4.11}$$

$$V(t) = V_0 \cos(\omega_0 t) + V_n(t), \tag{4.12}$$

Inside the lock-in amplifier this signal, equation (4.12), goes through the ac amplifier, which may contain filters to remove frequencies other than those near the reference frequency. This provides a voltage gain, $G_{ac}$, producing a signal looking like equation (4.13)

$$V = G_{ac} V_0 \cos(\omega_0 t), \tag{4.13}$$

This signal, equation (4.13), is sent to a multiplier stage which multiplies equation (4.13) with the reference voltage, (4.14).

$$V = E_0 \cos(\Omega_0 t), \tag{4.14}$$

The output of the multiplier stage is shown in equation (4.15) and can be

$$V = G_{ac}E_0V_0\cos(\Omega_0 t)\cos(\omega_0 t) = \frac{1}{2}G_{ac}E_0V_0[1+\cos(2\omega_0 t)], \tag{4.15}$$

The frequencies of the two signals, $\omega_0$ and $\Omega_0$, are the same and so when the signals are multiplied there are two outputs, the second harmonic, $2\omega_0$, and a dc component. We are only interested in the DC component so the signal is passed through a low-pass filter which removes the second harmonic as well as removes the random noise. The final component of the lock-in amplifier is a dc amplifier, with a voltage gain of $G_{dc}$. The signal has now been removed from the noise and the final output voltage is shown in equation (4.16) [47].

$$V = \frac{1}{2}G_{dc}G_{ac}V_0E_0, \tag{4.16}$$

The signals from the lock-in amplifiers are digitized and read by a computer producing the spectra that is seen in figure 4.11. The software used for reading the spectra was written initially for NICE-OHVMS and then adapted for NICE-OHZMS. It was written in C++ using Qt libraries by Professor Kyle Crabtree and maintained by Dr. Charles Markus.

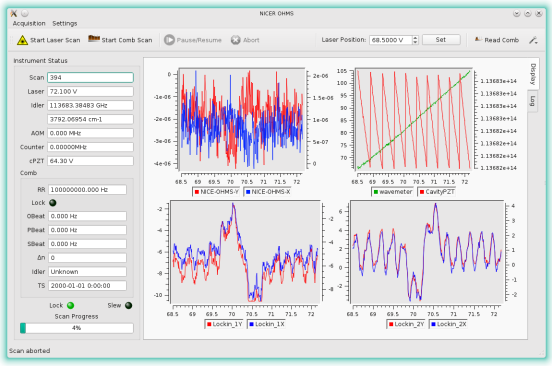

Figure 4.11. This is an amplitude modulated scan of $CO_2$ read out by the software on the computer. The top left panel displays the NICE-OHMS signal, signal coming out of the mixers. The top right panel displays the pzt voltage and the wavemeter values. The bottom panels display the readouts from the lock-in amplifiers.

Through these many parts and electronics, the NICE-OHZMS technique is being realized which will allow for the determination of the rovibrational spectra of radicals. With the fully built instrument, initial testing began and is outlined in chapter 5.

# Chapter 5

# Initial Testing of NICE-OHZMS Technique

The process of designing the Noise Immune Cavity Enhanced Optical Heterodyne Zeeman Modulation Spectroscopy, NICE-OHZMS, technique started with setting up the Noise Immune Cavity Enhanced Optical Heterodyne Velocity Modulation Spectroscopy (NICE-OHVMS) instrument, which was obtained from the University of Illinois Urbana-Champaign. A picture taken while setting up NICE-OHVMS is shown in figure 5.1. Once

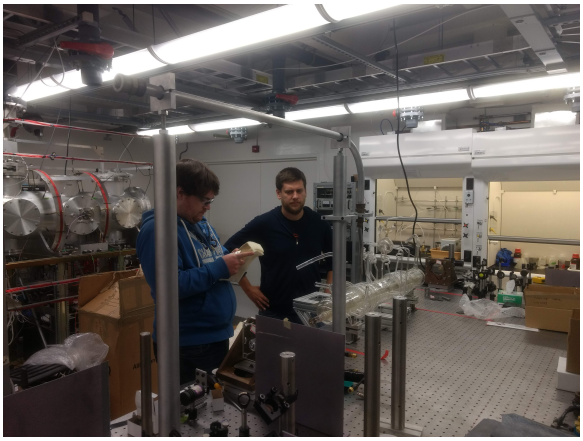

Figure 5.1. Here Dr. Zach Buchanan and Dr. Charles Markus are pictured by the newly installed laser table upon which the NICE-OHVMS instrument was installed. At the point this picture was taken, the glass cell had been installed, but not much else.

the NICE-OHVMS instrument was fully setup, it was shown to be working with the ob-

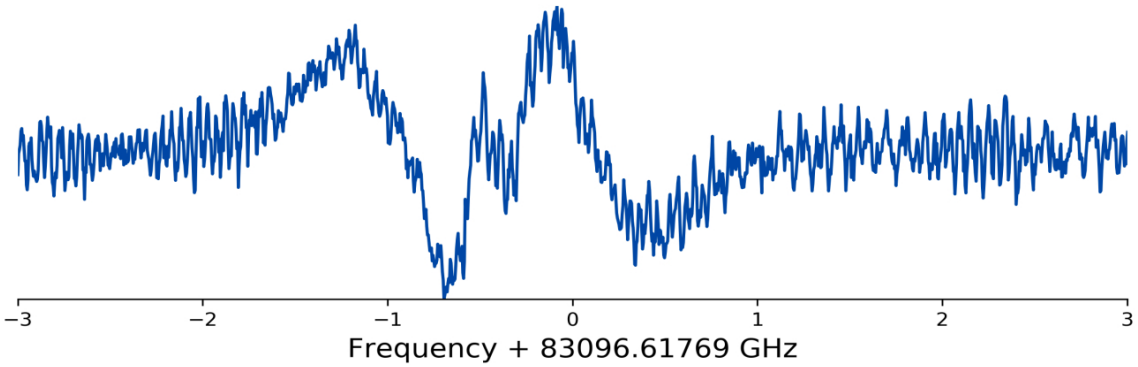


Figure 5.2. P(2) transition of the fundamental band of $HeH^+$ taken on the NICE-OHVMS instrument when it was first setup in the lab.

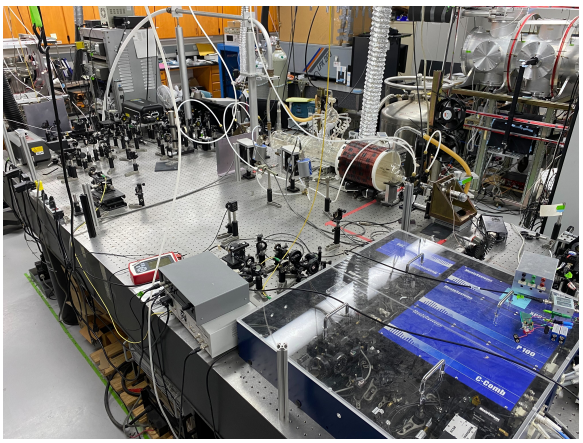

Figure 5.3. The fully setup NICE-OHZMS instrument in the lab.

tainment of the P(2) transition of the fundamental band of $HeH^+$, which is shown in figure 5.2.

At this point the instrument was modified to perform the NICE-OHZMS technique. This modification involved the addition of an AC audio amplifier driven solenoid shown in figure 7.1. This solenoid has a radius of 10 cm, a length of 25 cm, and a turn density of 7 $cm^{-1}$, producing a magnetic strength of 8 Ga/A. The solenoid is restricted in length due to the side arms of the glass cell and so does not cover the entire cell as can be seen in the figures. A picture of the NICE-OHZMS instrument is shown in figure 5.3, where the solenoid, rusty red, is shown in the upper right. For more details on the instrument, refer to chapter 4, which discusses the instrument in detail.

With the NICE-OHZMS instrument setup, proof of concept testing began. In order

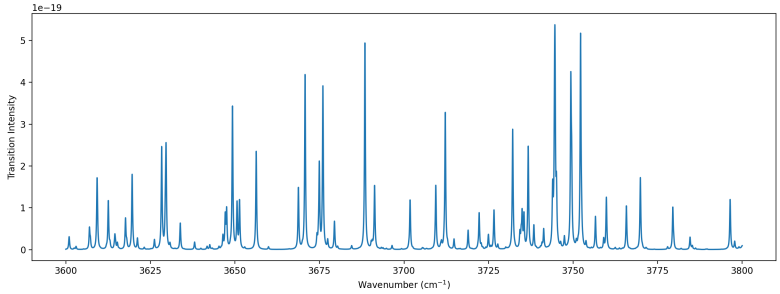


Figure 5.4. Water absorption intensity in the wavenumber region 3600 $cm^{-1}$ to 3800 $cm^{-1}$. Used to determine regions with low water absorption.

to effectively test if this technique is selective to open-shell molecules, meaning it can discriminately determine the rovibrational spectra of open-shell molecules from that of closed-shell molecules, both an open-shell test molecule and a closed-shell test molecule were needed. The open-shell test molecule chosen was nitric oxide, NO, and the closed-shell test molecule was $CO_2$. Nitric oxide was chosen because it is a relatively stable open-shell molecule that can be purchased in a gas cylinder and has a decently long self life. Most other open-shell molecules would need to be made using a discharge, which will be done in the future when using this technique to determine the rovibrational spectra of molecules of astronomical interest. For the purposes of testing the use of NO is sufficient. The rovibrational spectrum of NO is already known which adds to it being an ideal open-shell test molecule. In this testing experiment 1% NO in Ar was used. $CO_2$ was chosen as the closed-shell test molecule because it is easy and cheap to prepare and the rovibrational spectrum of it is published. A mixture of 20% $CO_2$ in Ar was prepared for testing. With test molecules chosen, transitions for these molecules were chosen based upon the scanning region of the OPO and the location of water absorption lines, which are shown in figure 5.4 in the region between 3600 and 3800 $cm^{-1}$. To avoid water absorption lines, for NO the transition pair $R(18.5)e/f\,^2\Pi_{1/2} -^2 \Pi_{1/2}$ at 3775.51 $cm^{-1}$ was chosen and for $CO_2$ the P(26) transition of the $\nu_1 + \nu_3$ combination band at 3792.04 $cm^{-1}$ was chosen. Other transitions were also looked observed. Each test molecule was observed individually by flowing the molecule into the glass cell at a pressure of  1.8 Torr. The transitions were observed with increasing magnetic field and the resulting spectra are shown in figure 7.2

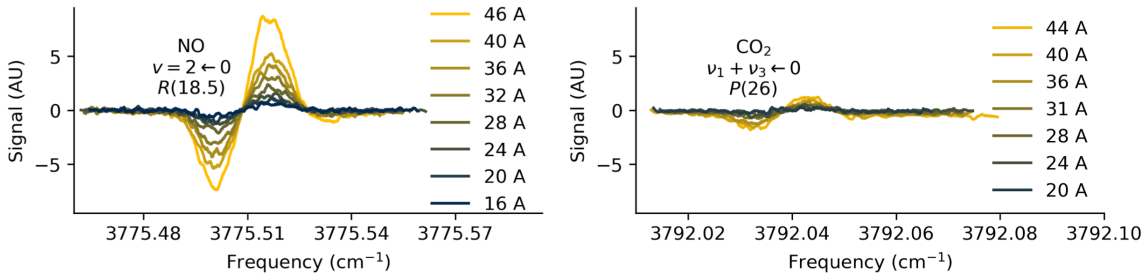


Figure 5.5. NICE-OHZMS spectra of NO and $CO_2$ as a function of current applied to the solenoid. For NO the R(18.5) transition of the first overtone band is shown on the left and for $CO_2$ the P(26) transition of the $\nu_1 + \nu_3$ combination band is shown on the right.

where there is a roughly quadratically increasing lineshape associated with magnetic field strength. Since this technique is open-shell selective, it was expected that the transition of NO would be seen and the transition of $CO_2$ would not be seen. This is not the case, as is exhibited by figure 7.2. The presence of the $CO_2$ transition has been attributed to the magnetic field inducing amplitude modulation into the system.

It was assumed that this amplitude modulation resulted from the magnetic field interacting with magnetic components in the instrument causing mechanical vibrations. The initial idea for solving this was to build a shield around the solenoid out of a material that would block the magnetic field, such as mu metal. This was attempted, but given that the magnetic field goes through the center of the solenoid, which is surrounding a glass cell with many arms off it, this was not possible. Since shielding the magnetic field would not work, the next idea was to eliminate the magnetic component that was experiencing mechanical vibrations due to the magnetic field. The springs holding the cavity mirrors to the cell were found to be magnetic and so were replaced with nonmagnetic springs. This replacement did not eliminate the $CO_2$ signal and so was not the cause or at least sole cause of the amplitude modulation.

The cause of the amplitude modulation was still an issue, but while trying to solve this we decided to extend the length of the cavity to improve the mode matching. This required not only extending the cavity length, but also redoing the lenses directing the beam into the cavity, the lenses making up the telescope. To ensure that the beam was making it into the cavity with the correct beam diameter, the beam diameter after a 20

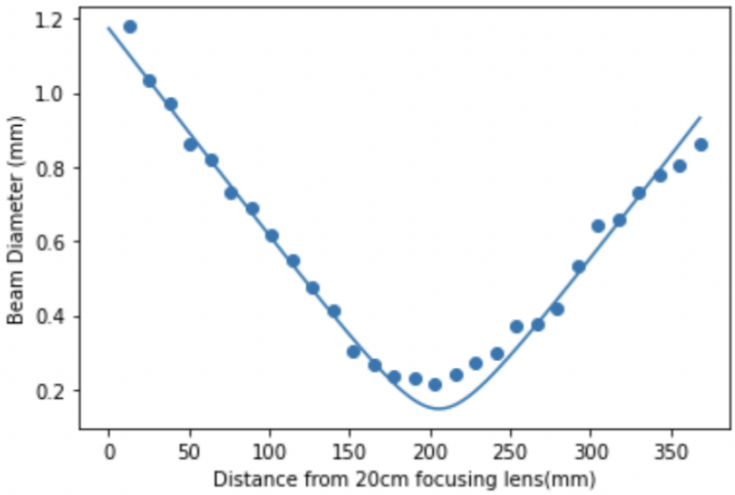


Figure 5.6. A plot of the beam diameter of the idler beam as determined by a chopper as a function of distance from a 20cm focusing lens.

cm focusing lens was determined using a chopper and found to be 1.106 mm. A plot of the beam diameter as a function of distance from the 20 cm focusing lens is shown in figure 5.6. The cavity length went from 1.91 m to 2.34 m and a new optical path directing the idler laser beam to the cavity was set up. This was done using ABCD matrices and a raytracing program, which made possible the mapping of the path, as is shown in figure 5.7, which shows the distances between the 20 cm and 50 cm focusing lens (black vertical lines). The red line indicates the laser beam, the green arrows indicate focal points and the black lines indicate lenses or mirrors, with the first and second black lines being the 20 cm and 50 cm focusing lenses respectively and the last two black lines being the cavity mirrors.

With the new cavity length and beam path we went back to trying to determine the cause of the amplitude modulation. The cause was still assumed to be some sort of mechanical vibration and since the springs did not solve this problem we identified all the magnetic components in the instrument, thinking that these might be shaking at the frequency driving the magnetic field. This included screws, irises, mirror mounts, piezos, cradles for holding the cell, along with other parts. NICE-OHZMS spectra with all the original magnetic parts are shown in figure 5.8. On the left is shown the R(18.5) transition of NO and on the right is the P(26) transition of $CO_2$. The top spectra is from

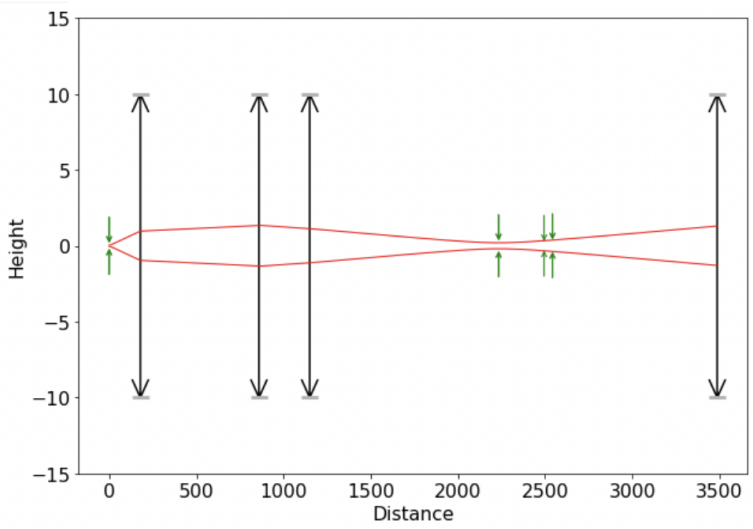


Figure 5.7. Proposed idler beam path showing the beam waist formed by the focusing lenses, made using a raytracing program. The red line indicates the laser beam, the green arrows indicate focal points and the black lines indicate lenses or mirrors. The first and second black lines are 20 cm and 50 cm focusing lenses respectively and the last two black lines are the cavity mirrors.

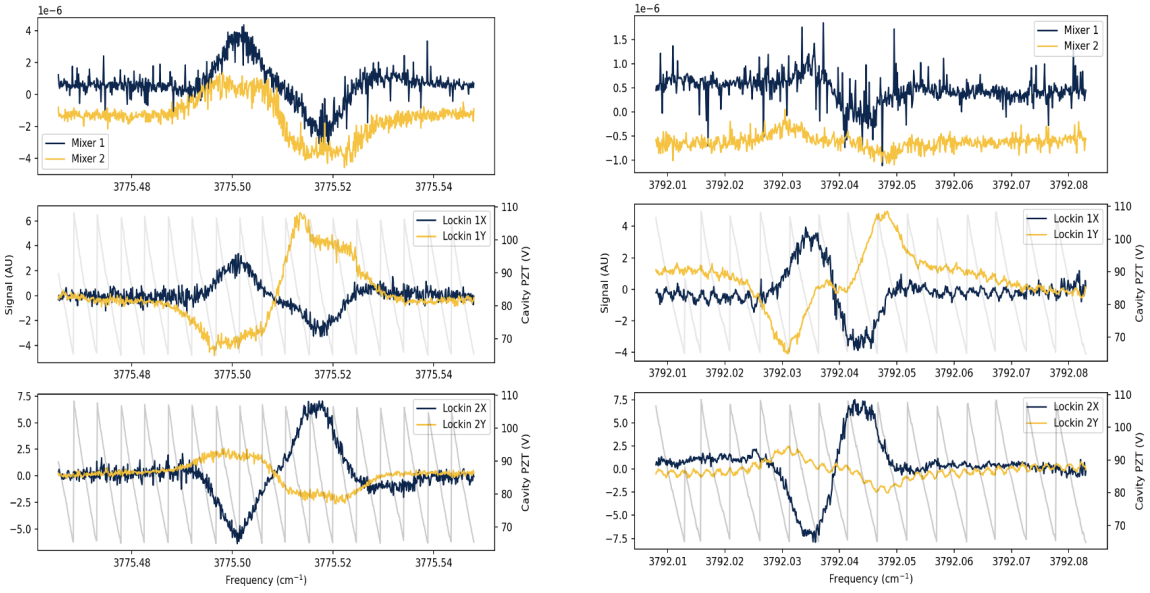


NO R(18.5) transition

$CO_2$ P(26) transition

Figure 5.8. NICE-OHZMS spectra taken before replacing the magnetic components. On the left is shown the R(18.5) transition of NO and on the right is the P(26) transition of $CO_2$

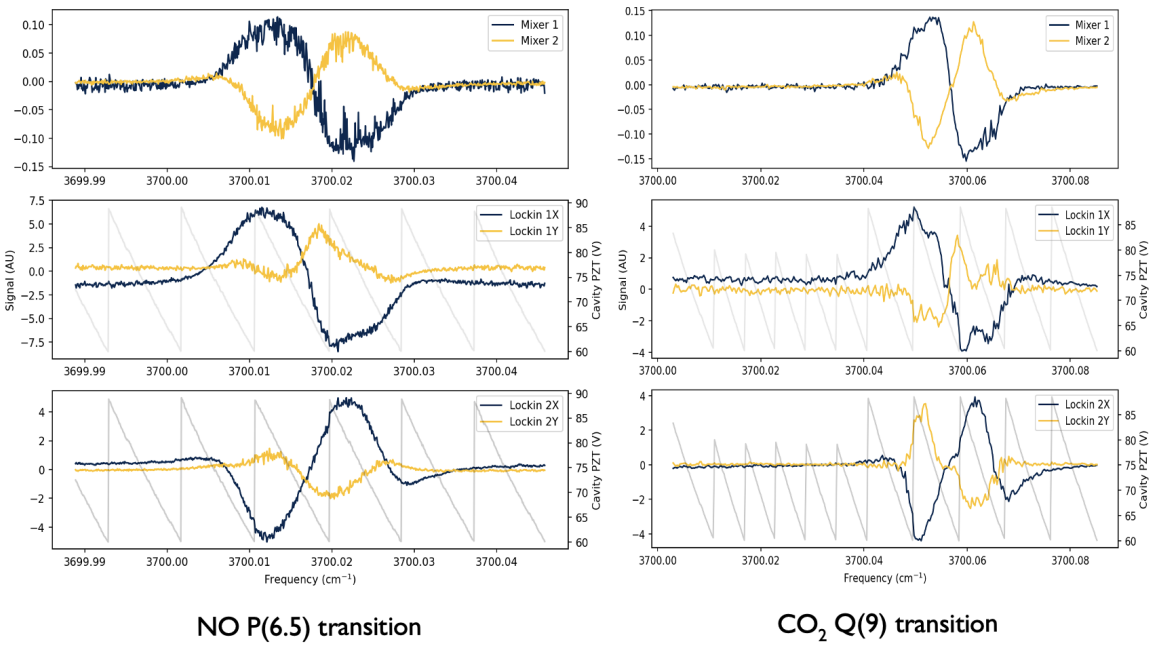


Figure 5.9. NICE-OHZMS spectra taken after replacing the magnetic components.On the left is shown the P(6.5) transition of NO and on the right is the Q(9) transition of $CO_2$

the mixers and is the pure signal that has not been demodulated at the frequency used for the Zeeman modulation. For both open and closed shell molecules we would expect to see signal here since no demodulation by the lock-ins has occured. The lower two spectra are the demodulated signal and so if the technique was working we would expect to see only signal for NO. After replacing the small magnetic parts, such as the screws, mirror mounts, irises, and cradles for holding the cell, the spectra shown in figure 5.9 was obtained. As can be seen when comparing figures 5.8 and 5.9, the replacement of these parts did not remove the $CO_2$ signal, as was hoped. The next thing to try was to replace the piezos, which were the last remaining magnetic component not yet replaced and could have been the cause of the shaking. These were ordered and while waiting for the parts I turned my attention to VUV photoionization cluster work, which is covered in chapter 6. Since I had moved onto other work, an undergrad tested the new piezos when they arrived and found that they did not remove this amplitude modulation. This means there is some other issue causing this amplitude modulation, or that amplitude modulation is not the issue. An idea for future trouble shooting is to build a helmholtz coil around

the solenoid to isolate the magnetic field so that it cannot affect any remaining magnetic components in the instrument. This trouble shooting is left for future students to fully realize this technique.

Not only were there issues with the signal itself, but there were many other hurtles in getting this instrument set up. These included the breaking of the wavemeter, used to determine the wavelength of the laser beam going into the cavity, the miss-alignment of the OPO, and the appearance of the signal leaking into the ground and therefore interfering with all signals. Each of these hurtles caused a delay in progress, but ultimately was dealt with.

While the pursuit of obtaining Doppler free rovibrational spectra of radicals of astronomical interest has not yet been realized, the quest to better understand how water surrounding three diols affects the reactivity of these diols has been realized and is discussed in detail in chapter 6.

# Chapter 6

# An experimental and computational view of the photoionization of diol water clusters


## ABSTRACT

In the interstellar medium, diols and other prebiotic molecules embed onto icy mantles surrounding dust grains. Water in the ice may affect the reactivity and photoionization of these diols. Clusters of the diol molecules ethylene glycol (EG), 1,2-propylene glycol, and 1,3-propylene glycol with water were used as a proxy to study this interaction. These diol water clusters were generated in a continuous supersonic molecular beam, photoionized by synchrotron vacuum ultraviolet light from the Advanced Light Source, and subsequently detected by reflectron time-of-flight mass spectrometry. From the mass spectra, taken at increasing photon energy, the appearance energies for the detected clusters were determined. Clusters of both diol fragments and unfragmented diols with water were detected. The lowest energy geometry optimized conformers for the observed EG water clusters and EG fragment water clusters have been visualized theoretically, providing insight into hydrogen bonding networks and how these affect fragmentation and appearance energy. As the number of water molecules clustered around EG fragments (m/z 31 and 32) increased, the appearance energy for the cluster decreased, indicating a stabilization by water. This trend was supported by theory calculations. Fragment clusters from 1,2-propylene glycol

exhibited a similar trend, but with a smaller energy decrease and no trend was observed with fragment clusters resulting from 1,3-propylene glycol. This indicates that the effect of water on the reactivity and photoionization of diols is dependent upon the size of the diol, the location of the hydroxyl group, and the number of waters clustered around the diol.

# INTRODUCTION

Diols, alcohols with 2 hydroxyl groups, in the interstellar medium may have acted as prebiotic molecules, participating in reactions forming basic building blocks of life, such as amino acids. The diol ethylene glycol (EG) has been detected in space, both in the interstellar medium (ISM) as well as in cometary ices, specifically in the hot core-like region Orion-KL [48] and in the star-forming region G31.41+0.31 [49]. EG may also have played a role in the formation of comets [48] and is thought to adsorb onto interstellar ice, which forms on the surface of dust grains and other solar system objects [50]. Vacuum ultraviolet (VUV) light in the ISM can photoionize embedded molecules, forming cations as well as fragments, which may react forming larger prebiotic molecules. To better understand and predict these reactions, it is necessary to learn how water surrounding EG and other diol molecules affects the reactivity and ionization of the diol and to understand the role of hydrogen bonds between the hydroxyl groups and water. Unraveling hydrogen bonding between water and diols has also a technological relevance. These molecules have anti-icing properties and can be used as cryoprotectants in the vitrification of biological cells and tissues [51], such as bovine embryos [52].

Here we study the photoionization of clusters with water molecules and three diol molecules, EG, $(CH_2OH)_2$, 1,2-propylene glycol (12PG), $CH_3CH(OH)CH_2OH$, and 1,3-propylene glycol (13PG), $CH_2OHCH_2CH_2OH$, with synchrotron-based VUV photoionization mass spectrometry. 1,2 and 1,3-propylene glycols will at times be referred to jointly as propylene glycol (PG).

The dielectric behavior [53] and thermodynamic properties [54] of propylene glycol water mixtures have been analyzed, as has a comparison of the dielectric properties of EG

and propylene glycol [55]. Using theoretical calculations, the thermodynamic properties of EG water mixtures were determined [56], and the structure of this mixture [57] as well as the pure liquid [58] was modeled using molecular dynamics simulations. The hydrogen bond networks of liquid EG water clusters have been examined using near-infrared spectroscopy and Raman spectroscopy. Both the IR and Raman spectroscopy experiments found that the structure is determined by the hydrogen bonds formed between the hydroxyl groups and water and the nature of the clusters depends on concentration [59] [60].

While there has been extensive work, both experimentally and theoretically, on liquid-phase EG water mixtures, little is known about the photoionization of gas-phase EG and propylene glycol water clusters, leaving a gap in understanding how water surrounding a diol affects the diol's ionization and fragmentation when exposed to VUV light.

Single photoionization is the least complicated photoionization method and is most commonly accomplished using VUV light [61], which provides an efficient and soft method for ionizing molecules [62]. Using this method, the ionization energy (IE), appearance energy (AE), photoioinization efficiency curves and thermodynamic properties of molecules can be determined [62]. The first published VUV photoionization mass spectrometry experiment generated VUV radiation using a discharge lamp coupled to a monochromator [63]. Roughly 15 years later, tunable VUV radiation was generated by a synchrotron in France [64], and soon after, a molecular beam was coupled to the synchrotron, allowing for the determination of photoionization intensity curves of acetylene and carbon dioxide [65]. The tunable nature of the VUV radiation results in precise threshold ionization, with little excess internal energy imparted to the ion [62]. As synchrotrons have become more accessible, end stations with cluster beams coupled to time-of-flight mass spectrometers have given rise to a new series of photoionization studies focused largely on hydrogen bonded and van der Waals clusters [62].

The thermodynamics and bonding properties of water clusters have been analyzed using tunable VUV radiation (10–14 eV) with detection by a reflectron time-of-flight mass spectrometer. The neutral clusters were photoionized forming an unstable cation cluster,

$[(H_2O)_n^+]$, which underwent a redistribution, forming protonated clusters containing up to 79 molecules. Photoionization intensity curves were obtained, and from these, AEs were determined. A decrease in AE was observed in neutral water clusters as the cluster size increased, with the most substantial drop observed as cluster size increased to 4 water molecules. With large clusters of more than 22 water molecules, the AE converged. The appearance energy for small protonated water clusters was also observed to decrease as cluster size increased, due to the stabilization caused by the extensive intracluster hydrogen bond network [66].

The effects of hydrogen bonding networks on fragmentation dynamics have been observed through the photoionization of alcohols and sugars. VUV photoionization of the simplest alcohol, methanol, in the presence of water has been studied. Below the ionization energy of methanol, the mass spectrum was dominated by protonated methanol clusters, $(CH_3OH)_nH^+(n = 1 - 12)$. When the concentration of water was increased, methanol water clusters, $(CH_3OH)_n(H_2O)H^+(n = 2 - 11)$ formed [67]. Using a 355 nm picosecond laser, the photoionization of ethanol aqueous solutions was performed and it was found that the hydrogen bond networks of water were disrupted by the addition of ethanol and as ethanol concentration increased, hydrated ethanol clusters were observed to form [17]. Photoionization mass spectrometry of the larger alcohol glycerol has been performed, and fragmentation of the glycerol radical cation was found to occur via two channels. One channel proceeds through a six-membered hydrogen transfer transition state, forming a ternary intermediate, and the other channel proceeds via the cleavage of the C-C bond. The intermediate is composed of neutral water, neutral formaldehyde, and a vinyl alcohol radical cation, explaining why the first observed products result from water or formaldehyde loss [68]. Similar to glycerol, water elimination and fragmentation through a cyclic intermediate were observed with photoionization mass spectrometry of the sugar deoxyribose. In this case, most of the fragmentation occurred when the cyclic molecule was unfurled by breaking a C-C bond. This caused two hydroxyl groups to come close together, resulting in water elimination [69]. Hydrogen bonding in glycerol was further investigated by performing photoionization mass spectrometry of glycerol wa-

ter clusters. The AE of certain fragments were found to be similar to those seen with pure glycerol, while for other fragments the AE was found to depend upon both cluster composition and water concentration in the beam. Theory calculations predicted certain barrierless chemical processes when glycerol water clusters were photoionized, which were not observed to occur with pure glycerol [3].

There are some reports on the thermal decomposition and dissociative ionization of pure EG performed via VUV photoionization mass spectrometry. From this, the appearance energies of the observed fragments were determined, and possible formation channels for the fragments were proposed via theory calculations [4]. Complementing this work, Kumar et al. performed DFT theory calculations to determine the structure, stability, and spectral properties of pure EG as well as EG-water clusters, which up until this writing had not been studied experimentally in the gas phase. These calculations found that, due to electrostatics and polarization, interactions between water and EG are preferred over those between pure EG [70]. To further our understanding of photoionization of alcohol water clusters, we performed photoionization mass spectrometry experiments of 1,2-propylene glycol water clusters, 1,3-propylene glycol water clusters, and EG water clusters in a molecular beam paired with theoretical calculations on both neutral and ionized EG water clusters. Through this work, the effect of hydrogen bond networks formed when water clusters around diols is understood through the changes in ionization energy, appearance energy and fragmentation of the diols in the clusters.

# METHODS

## Experimental Details

The experiment was performed with a reflectron time-of-flight mass spectrometer containing a continuous supersonic expansion molecular beam source connected to a 3-meter vacuum monochromator and attached to the Chemical Dynamics Beamline (9.0.2) located at the Advanced Light Source. For a detailed description of the instruments, refer to previous studies [71], [72], [66]. The diol of interest, either EG or propylene glycol, is placed in a stainless steel nozzle, vaporized by a cartridge heater, and entrained in an argon carrier

gas seeded with water vapor. The gas mixture passes through a 50 $\mu$m nozzle source and supersonically expands into a vacuum chamber, yielding the desired diol water molecular beam. This beam is extracted through a skimmer into a differentially pumped interaction region where the clusters are exposed to and ionized by VUV synchrotron radiation. The ionized fragments are then detected using a reflectron time-of-flight mass spectrometer. Mass spectra are recorded at photon energies between 9.0 and 12.5 eV every 50 meV. Photoionization intensity curves, which show ion count versus photon energy (in eV), of the diol water clusters are obtained by integrating over the peaks in the mass spectrum at each photon energy after being normalized by the photon flux.

## Computational Details

Theoretical calculations were performed on the EG water cluster system. The optimized geometries of the observed clusters were determined through a conformation search using the semi-empirical quantum chemistry package Crest [73]. The lowest energy conformer from this search was further optimized using Q-Chem [74] at the $\omega$B97X-D/6-311+G-(2d,p) level of theory to obtain the neutral cluster geometry. To determine the cation geometry, the lowest energy conformer was optimized using Q-Chem [74] at the $\omega$B97X-D/6-311+G-(2d,p) level of theory with the total charge set to +1. For geometry optimization, the hybrid functional $\omega$B97X-D reproduces well the intermolecular interactions given its range-separated exact exchange and dispersion corrections [75]. Single point calculations were carried out with the $\omega$B97X-V functional and the def2-TZVPPD basis set to determine vertical and adiabatic ionization energies. This computational framework was chosen due to its enhanced atomic orbital basis set. Appearance energies were calculated using the calculated energies (E) for neutral EG (m/z 62), neutral m/z 31, and cation m/z 31, as shown in equation 6.1 where m, n, and k represent the number of water molecules in the cluster. Starting from a cluster consisting of one EG and $m$ water molecules, the AEs of fragment m/z31$(H_2O)_n^+$ ionized clusters were calculated at the $\omega$B97X-V/def2-TZVPPD level of theory as shown:

$$AE(m/z31(H_2O)_n^+) = E(m/z31(H_2O)_{m-n}) + E(m/z31(H_2O)_n^+) - E(m/z62(H_2O)_m) \tag{6.1}$$

More details on this calculation are given in the results and discussion section.

# RESULTS AND DISCUSSION

## Mass Spectra of EG

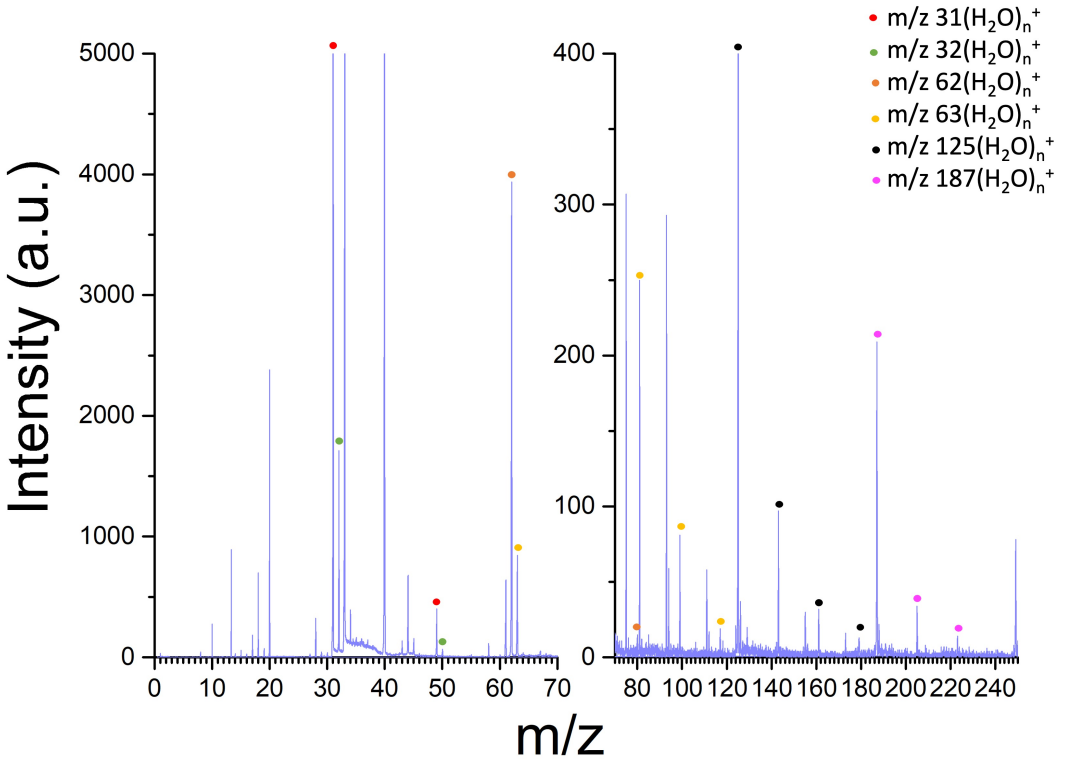


Figure 6.1. 40% EG mass spectrum recorded at 12.0 eV. The cluster series for m/z $31(H_2O)_n^+$, m/z $32(H_2O)_n^+$, m/z $62(H_2O)_n^+$, m/z $63(H_2O)_n^+$, m/z $125(H_2O)_n^+$, and m/z $187(H_2O)_n^+$ are indicated with colored dots.

The concentration of EG to water in the molecular beam was adjusted by changing the temperature of the nozzle as well as the pressure of the backing Ar gas. The mass spectrum taken with 40% EG at 12 eV is shown in figure 6.1, where the x-axis has been broken up and split over the 2 plots to better show the intensity of the peaks. The mass spectra are dominated by EG water clusters, both protonated and unprotonated, as well as EG fragments and fragment water clusters. The cluster series m/z $31(H_2O)_n^+$, m/z $32(H_2O)_n^+$, m/z $62(H_2O)_n^+$, m/z $63(H_2O)_n^+$, m/z $125(H_2O)_n^+$, and m/z $187(H_2O)_n^+$ are indicated with colored dots. The concentration of EG in the molecular beam as well as

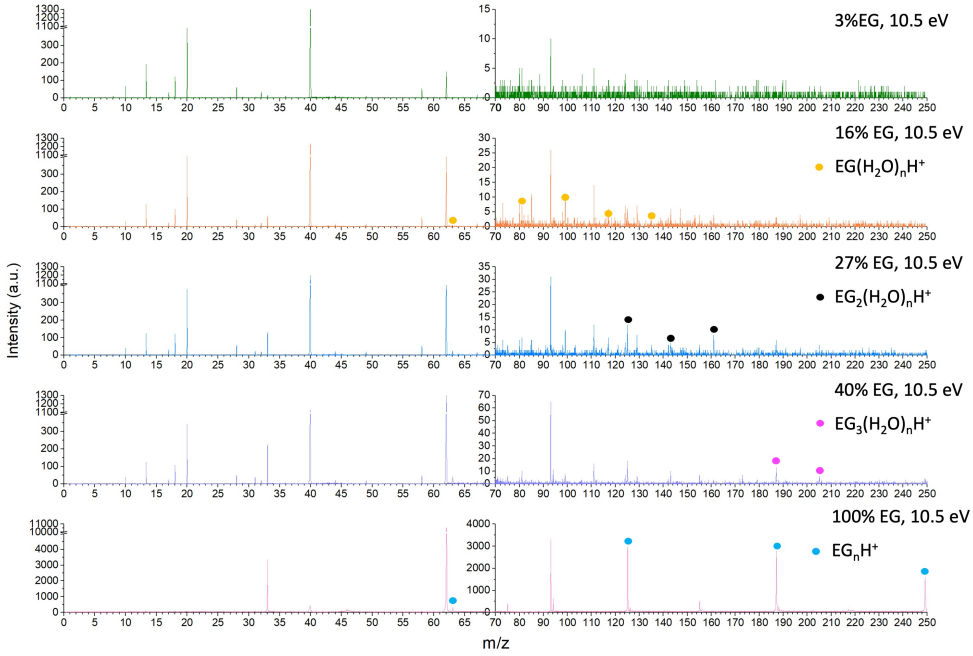


Figure 6.2. Mass spectra of EG water clusters recorded at 10.5 eV at EG mole fractions of 3%, 16%, 27%, and 40%. Monomer, dimer and trimer protonated EG water clusters are indicated with colored dots.

the photon energy effect the intensity of clusters. This can be observed in figures 6.2 and 6.3 which show mass spectra obtained at different mole fractions of EG, specifically 3%, 16%, 27%, and 40%. All mass spectra in figure 6.2 were taken with a photon energy of 10.5 eV and in figure 6.3 with a photon energy of 12.0 eV. Monomer, dimer and trimer protonated EG water clusters are indicated in these figures.

Along with fragments m/z 31 and m/z 32 (shown in figure 6.1), other EG fragments were observed with masses m/z 43, 44, 45, and 61. A previous VUV photoionization study of pure EG determined the formation channels and chemical identities of these fragments [4]. Based upon this, the fragments are attributed as follows: m/z 31 is $CH_2OH^+$, m/z 32 is $CH_3OH^+$, m/z 43 is $CH_3CO^+$, m/z 44 is $CH_2CHOH^+$, m/z 45 is $CH_3CHOH^+$, and m/z 61 is $C_2H_5O_2^+$.

In the mass spectrum shown in figure 6.1, the peaks to the left of m/z 125$(H_2O)_nH^+$ (which correspond to m/z $EG_2(H_2O)_nH^+$), and m/z 187$(H_2O)_nH^+$ (which correspond to

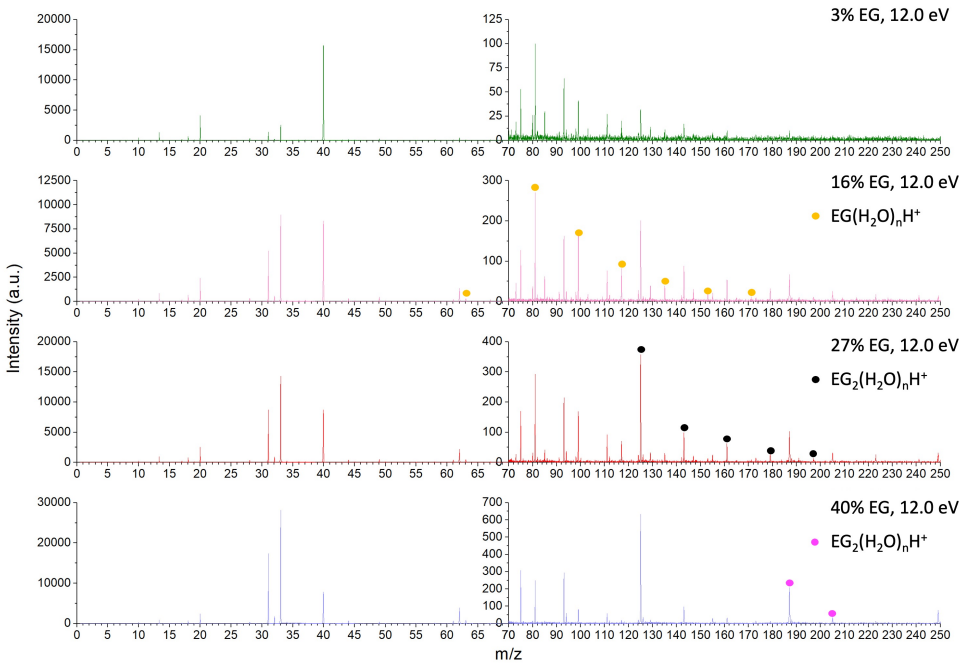


Figure 6.3. Mass spectra of EG water clusters recorded at 12.0 eV at EG mole fractions of 3%, 16%, 27%, and 40%. Monomer, dimer and trimer protonated EG water clusters are indicated with colored dots.

$EG_3(H_2O)_nH^+$) are from unprotonated EG dimer and trimer water clusters. Larger clusters with up to 5 waters around EG, $EG(H_2O)_5H^+$ and $EG_2(H_2O)_5H^+$, were observed, but are not highlighted in figure 6.1 due to the low intensity of their corresponding peaks. The signal from these largest clusters is found to be too noisy to give useful information, so these clusters are omitted from subsequent tables.

Figure 6.4 shows the sum of the cluster series as a function of the EG mole fraction taken at 12.0 eV. EG fragments represents the sum of masses m/z 31, 32, 33, 43, 44, 45, 61. All clusters are observed to increase with the concentration of EG. With increasing EG concentration, the intensity of fragment cluster m/z 31$(H_2O)^+$ increases more rapidly than the intensity of pure EG clusters.

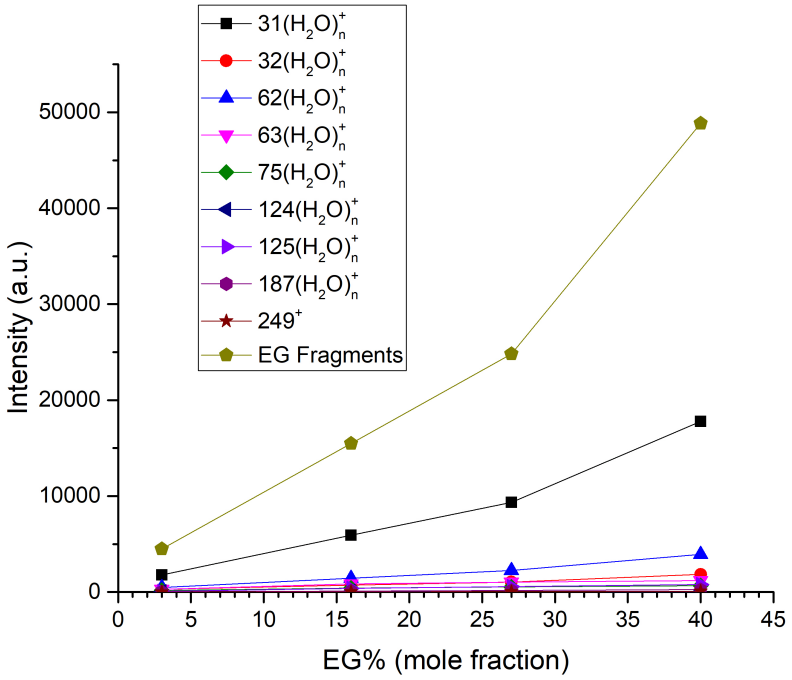


Figure 6.4. Sum of intensities of each cluster series as a function of EG mole fraction, recorded at 12.0 eV. The EG fragments summed are m/z 31, 32, 33, 43, 44, 45, 61.

| | $CH_2OH$ | $CH_2OH^+$ | $CH_3OH$ | $CH_3OH^+$ |
|---|---|---|---|---|
| $(H_2O)_0$ | | | | |
| $(H_2O)_1$ | | | | |
| $(H_2O)_2$ | | | | |
| $(H_2O)_3$ | | | | |
| $(H_2O)_4$ | | | | |

Figure 6.5. Geometry optimized lowest energy conformers for fragments with mass 31, both neutral ($CH_2OH$) and cation ($CH_2OH^+$), and mass 32, neutral ($CH_3OH$) and cation ($CH_3OH^+$). These conformers were identified using the semi-empirical quantum chemistry package crest and then further optimized using Q-Chem ($\omega$B97X-D/6-311+G-(2d,p)).

| | EG | $EG^+$ | $EG_2$ | $EG_2^+$ |
|---|---|---|---|---|
| $(H_2O)_0$ | 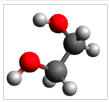 | 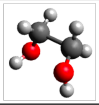 | 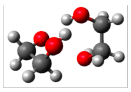 | 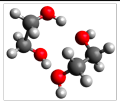 |
| $(H_2O)_1$ | 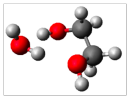 | 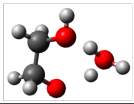 | 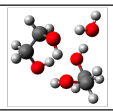 | 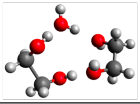 |
| $(H_2O)_2$ | 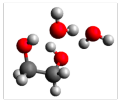 | 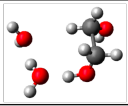 | 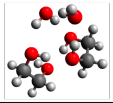 | 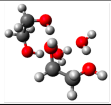 |
| $(H_2O)_3$ | 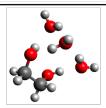 | 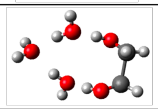 | 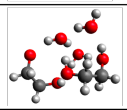 | 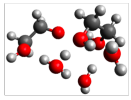 |
| $(H_2O)_4$ | 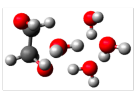 | 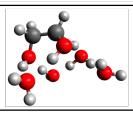 | 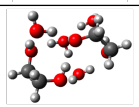 | 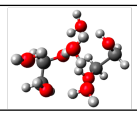 |

Figure 6.6. Geometry optimized lowest energy conformers for both neutral and cationic EG (mass 62) and dimer EG (mass 124). These conformers were identified using the semi-empirical quantum chemistry package crest and then further optimized using Q-Chem ($\omega$B97X-D/6-311+G-(2d,p)).

| | $EGH^+$ | $EG_2H^+$ | $EG_3H^+$ | $EG_4H^+$ |
|---|---|---|---|---|
| $(H_2O)_0$ | 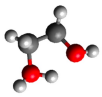 | 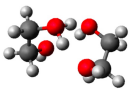 | 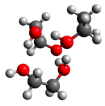 | 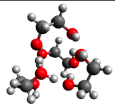 |
| $(H_2O)_1$ | 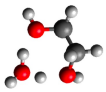 | 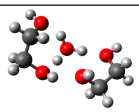 | 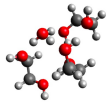 | 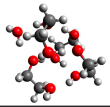 |
| $(H_2O)_2$ | 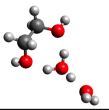 | 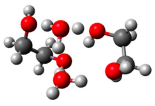 | 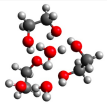 | 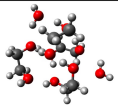 |
| $(H_2O)_3$ | 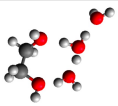 | 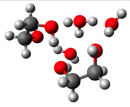 | 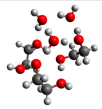 | 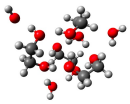 |
| $(H_2O)_4$ | 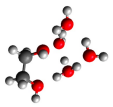 | 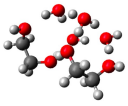 | 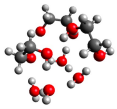 | 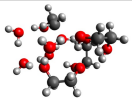 |

Figure 6.7. Geometry optimized lowest energy conformers for neutral and cationic protonated EG monomer (mass 63), dimer (mass 125), trimer (mass 187) and tetramer (mass 249). These conformers were identified using the semi-empirical quantum chemistry package crest and then further optimized using Q-Chem $\omega$B97X-D/6-311+G-(2d,p).

## Lowest Energy Geometries of EG Water Clusters

To predict the molecular structure of the clusters in the molecular beam, low-energy conformers were obtained using the semi-empirical quantum chemistry package Crest and the lowest energy conformer was further optimized at the quantum chemical level ($\omega$B97X-D/6-311+G-(2d,p)). These lowest energy conformers are shown in figures 6.5, 6.6, and 6.7.

Using the calculated energies of the optimized geometries of the clusters, the appearance energies of the ionized clusters were calculated and will be discussed in detail later. The structural models reveal the most energetically favorable hydrogen bonding patterns between EG and the water network. When EG is neutral, water molecules are observed to connect the two OH groups forming a pathway or water wire which makes for easy protron hoping between the two OH groups. When the fragments $CH_2OH^+$ and $CH_3OH^+$ are surrounded by three water molecules, the proton from the OH group of EG detaches and is shared between two water molecules forming a Zundel ion, which is the ion formed when 2 water molecules share a proton between them. This Zundel ion is also observed to form in protonated clusters with up to four EG molecules.

## Photoionization Intensity Curves and Appearance Energies (AE)

From the mass spectra, recorded every 50 meV, photoionization intensity curves were obtained for all clusters at each concentration of EG (3%, 16%, 27%, and 40%). These photoionization intensity curves are given in the SI. As an example, one photoionization intensity curve for fragment m/z 31 water clusters, taken with 27% EG in the molecular beam, is shown in figure 6.8. The arrows indicate the location of the appearance energy, which for this cluster varies substantially with cluster size. This will be discussed in detail later.

From the photoionization intensity curves, the appearance energies for the clusters, as a function of mole fraction, were determined and are given in table 6.1, along with experimental and calculated AE values from reference [4]. We define appearance energy as the energy needed to ionize and potentially fragment the gas phase molecule or cluster.

The concentration of EG in the molecular beam showed no effect on appearance energy

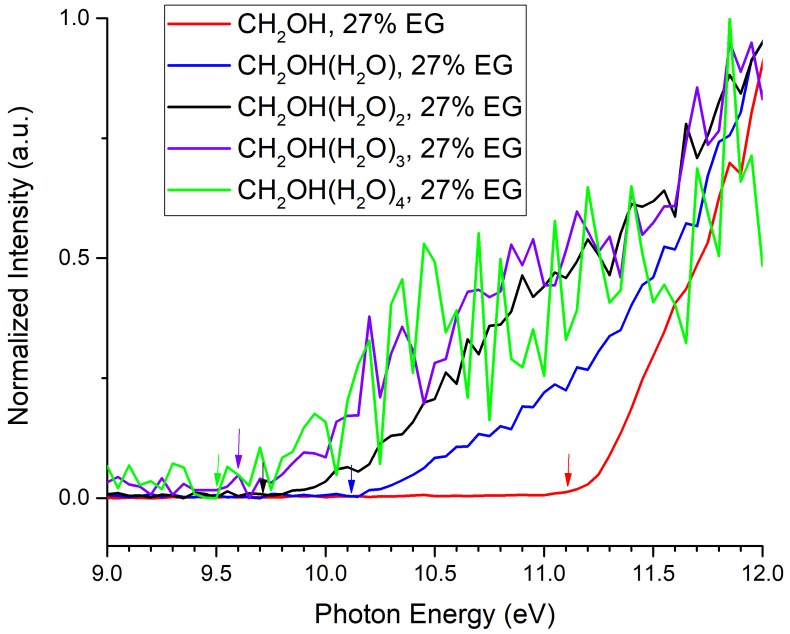


Figure 6.8. Photoionization intensity curve for fragment m/z 31 water clusters with 27% EG in the molecular beam. The arrows indicate the location of the appearance energy.

indicating that the concentration of water does not effect fragmentation. By contrast, the appearance energy is dependent upon the size of the cluster. The intensity of the clusters is directly related to the photon energy, as can be observed in figures 6.26, 6.27, 6.28, and 6.29 in the SI. The plots are shown for clusters with up to 4 waters, though not all clusters were observed to be this large.

## Ionization Energy

Typically, the appearance energy obtained from a photoionization intensity curve for a cluster with hydrogen bonds would correspond to vertical ionization energy (VIE), which occurs when a neutral cluster absorbs a VUV photon causing a transition to a vibrationally excited ionic state with the same geometry as the neutral cluster. From there the cluster may relax, resulting in a geometry change, and the energy difference between this relaxed cation and the neutral molecule is the adiabatic ionization energy (AIE). Vertical and adiabatic ionization energies for the lowest energy geometry optimized conformers of EG

Table 6.1. Appearance energies (AE) in eV of EG clusters as well as fragment clusters observed at different mole fractions of EG with an error of $\pm 0.1eV$. The error in the appearance energies from reference [4] is $\pm 0.05eV$. A - indicates that the signal to noise ratio was not good enough to obtain a conclusive AE value.

| | AE (eV) as a function of EG % | | | | AE (eV) from ref [4] | Calculated AE (eV) |
|---|---|---|---|---|---|---|
| | 3% | 16% | 27% | 40% | Experimental | Calculated |
| m/z $31^+$ | 11.1 | 11.1 | 11.1 | 11.1 | 11.12 | 11.18 |
| m/z $31(H_2O)^+$ | 10.2 | 10.2 | 10.1 | 10.1 | | |
| m/z $31(H_2O)_2^+$ | 9.8 | 9.8 | 9.7 | 9.8 | | |
| m/z $31(H_2O)_3^+$ | 9.7 | 9.7 | 9.6 | 9.6 | | |
| m/z $31(H_2O)_4^+$ | 9.6 | 9.6 | 9.5 | - | | |
| m/z $32^+$ | 10.8 | 11.1 | 11.2 | 11.2 | 11.42 | 11.47 |
| m/z $32(H_2O)^+$ | 10.4 | 10.3 | 10.3 | 10.4 | | |
| m/z $32(H_2O)_2^+$ | 9.9 | 9.9 | 9.9 | 9.9 | | |
| m/z $33^+$ | 10.2 | 10.3 | 10.2 | 10.2 | 10.45 | 11.77 |
| m/z $43^+$ | 10.3 | 10.6 | 10.3 | 10.5 | 10.64 | 11.43 |
| m/z $44^+$ | 10.7 | 10.7 | 10.7 | 10.7 | 10.64 | 10.80 |
| m/z $45^+$ | 10.5 | 10.5 | 10.3 | 10.5 | 11.00 | 10.80 |
| m/z $61^+$ | 10.9 | 10.9 | 10.9 | 10.9 | 10.84 | 10.77 |
| m/z 62 $(EG)^+$ | 9.9 | 9.9 | 9.9 | 9.9 | 9.85 | 9.77 |
| m/z $62(H_2O)^+$ | - | 9.6 | 9.6 | - | | |
| m/z $62(H_2O)_2^+$ | 9.7 | 9.7 | 9.7 | 9.7 | | |
| m/z 63 $(EGH^+)$ | 10.1 | 10.1 | 10.1 | 10.1 | | |
| m/z $63(H_2O)^+$ | 10.4 | 10.2 | 10.2 | 10.2 | | |
| m/z $63(H_2O)_2^+$ | 10.0 | 9.9 | 9.8 | 9.8 | | |
| m/z $63(H_2O)_3^+$ | 10.0 | 9.5 | 9.8 | 9.6 | | |
| m/z $63(H_2O)_4^+$ | - | 9.6 | 9.6 | - | | |
| m/z 124 $(EG_2)$ | 9.5 | 9.5 | 9.5 | 9.5 | | |
| m/z $124(H_2O)^+$ | 9.5 | 9.5 | 9.5 | 9.5 | | |
| m/z 125 $(EG_2H^+)$ | - | 9.9 | 10.0 | 9.9 | | |
| m/z $125(H_2O)^+$ | - | 10.1 | 9.6 | 9.6 | | |
| m/z $125(H_2O)_2^+$ | - | 9.8 | 9.7 | 9.7 | | |
| m/z $125(H_2O)_3^+$ | - | 9.8 | 9.9 | - | | |
| m/z $125(H_2O)_4^+$ | - | 9.9 | - | - | | |
| m/z 187 $(EG_3^+)$ | - | 9.7 | 9.7 | 9.7 | | |
| m/z $187(H_2O)^+$ | - | 10.0 | 9.6 | 9.7 | | |
| m/z $187(H_2O)_2^+$ | - | 9.8 | 9.7 | 9.6 | | |
| m/z 249 $(EG_4H^+)$ | - | 9.8 | 9.8 | 9.8 | | |

water clusters and dimer EG water clusters, were calculated and are shown in tables 6.2 and 6.3, respectively. The larger the difference in energy between the adiabatic and vertical ionization energies, the worse the Frank-Condon Factor and therefore the greater the geometry change upon relaxation after ionization. In this case, the vertical and adiabatic ionization energies are not close indicating a change in geometry upon

Table 6.2. Calculated adiabatic and vertical ionization energies for EG (mz 62) clusters.

| | EG (mz 62) | |
|---|---|---|
| | Adiabatic Ionization (eV) | Vertical Ionization (eV) |
| $(H_2O)_0$ | 9.6 | 10.5 |
| $(H_2O)_1$ | 9.3 | 11.4 |
| $(H_2O)_2$ | 8.9 | 10.5 |
| $(H_2O)_3$ | 8.3 | 9.7 |
| $(H_2O)_4$ | 8.0 | 9.8 |

Table 6.3. Calculated adiabatic and vertical ionization energies for EG dimer(mz 124) clusters.

| | EG Dimer (mz 124) | |
|---|---|---|
| | Adiabatic Ionization (eV) | Vertical Ionization (eV) |
| $(H_2O)_0$ | 8.7 | 9.8 |
| $(H_2O)_1$ | 8.5 | 10.1 |
| $(H_2O)_2$ | 8.4 | 10.1 |
| $(H_2O)_3$ | 8.3 | 10.4 |
| $(H_2O)_0$ | 8.6 | 10.1 |

relaxation. This ionization process is outlined for EG water clusters in figure 6.9 and for dimer EG (m/z 124) water clusters in figure 6.10.

In figures 6.9 and 6.10 certain hydrogen bonds are labeled and the Mulliken charges and spins on water are given. The ionization process changes the hydrogen bonding networks and cluster geometries. The Mulliken charge and spin is obtained theoretically via a Mulliken population analysis and gives an estimate of the partial atomic charges [76]. For the clusters shown, at threshold the majority of the charge and spin of the cluster is contained on EG indicating that when ionized, the charge prefers to stay on EG rather than moving towards water. Of the four clusters, water in cluster $EG(H_2O)^+$ has the highest charge and spin. This finding is in contrast to naphthalene water clusters and dimethyl uracil water clusters where, at 11.7 eV, a hole was observed in the 3A" orbital

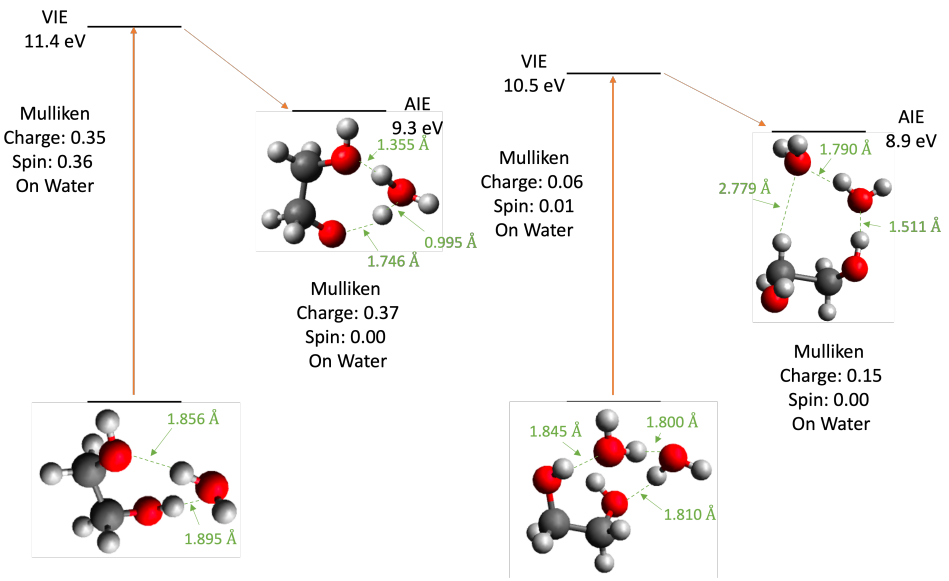


Figure 6.9. Vertical and adiabatic ionization of clusters EG($H_2O$) (left) and EG$(H_2O)_2$ (right)

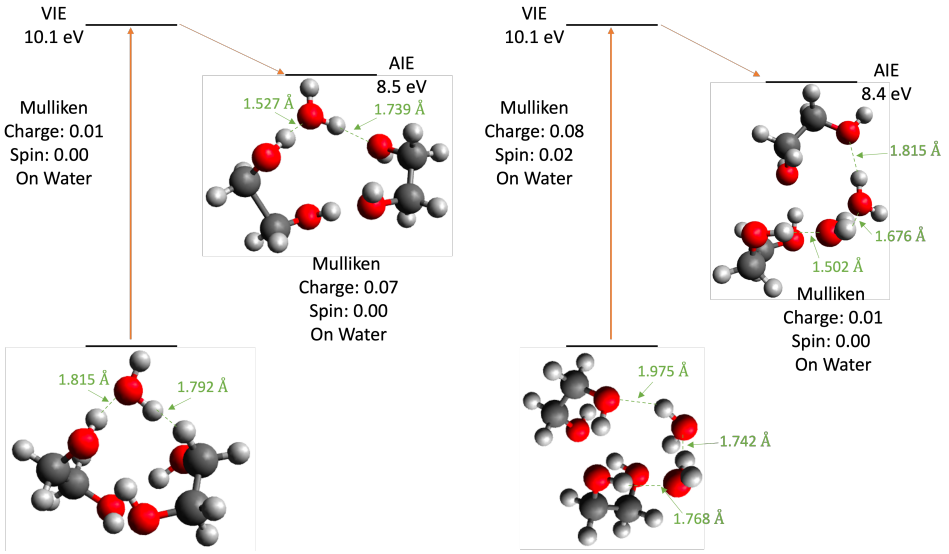


Figure 6.10. Vertical and adiabatic ionization of clusters $EG_2$($H_2O$) (left) and $EG_2(H_2O)_2$ (right)

of water [77][78].

## Changes in AE with cluster size

As can be seen in table 6.1, as cluster size around both protonated and unprotonated EG monomer, dimer and trimer increases, the appearance energy decreases slightly and ultimately converges. This same trend was observed with glycerol water clusters [3], PAH

water clusters [77] and nucleobase water clusters [79]. A similar trend in decreasing AE was observed with increasing methanol molecules clustered around a single water molecule [67]. Pure EG (m/z 62) has an appearance energy of 9.9 eV, while an EG cluster with 2 waters has an appearance energy of 9.7 eV, a decrease of 0.2 eV, which is small given that the error in appearance energy is ± 0.1 eV. The appearance energies for fragments m/z 31 and 32 are over 1 eV higher than that of pure EG. The higher appearance energy is due to the additional energy needed to break the C-C bond of the unfragmented molecule or cluster after ionization. This process is outlined in figure 6.11. In contrast to the unfragmented clusters, the appearance energy of the fragment water clusters is found to decrease substantially as cluster size increases, with a nearly 1 eV drop when 1 water is added to the fragment. Water surrounding the unfragmented molecule stabilizes the transition state so less energy is required to break the C-C bond and form the fragment.

Given the high energy of the VUV beam, it might be expected that water would evaporate during the fragmentation process. This is found not to be the case given the observed fragment clusters. To investigate this, the average excess energy ($E_{excess}$), which could cause water molecules to evaporate, after ionization of the EG water clusters was calculated using equation 6.2.

$$E_{excess} = AE - AIE \tag{6.2}$$

The average appearance energy (AE) (which is the upper limit to the adiabatic ionization energy (AIE)) for EG water clusters is 9.7 eV and the average adiabatic ionization energy for these clusters is 9.3 eV giving an excess energy of 0.4 eV at the threshold. If this excess energy is higher than the binding energy of water in the cluster, then the water may evaporate. The binding energy of water in EG water clusters was determined following equation 6.3

$$E_{bind} = E[(EG)H_2O_n]^+ - E[(EG)H_2O_{n-1}]^+ - E(H_2O) \tag{6.3}$$

where E is the electronic energy calculated at $\omega$B97X-V/def2-TZVPPD level of theory. The calculated binding energies are given in table 6.4. These binding energies are in the same ball park as those found for methanol water clusters and ethanol water clusters [80].

Table 6.4. Binding energies in eV, calculated at the ωB97X-V/def2-TZVPPD level of theory, of the nth water (n = 1 - 4) attached to $EG(H_2O)_n$ clusters.

| | n = 1 | n = 2 | n = 3 | n = 4 |
|---|---|---|---|---|
| BE(eV) of $EG(H_2O)_n$ | 0.60 | 0.88 | 0.87 | 0.71 |

The average binding energy is 0.76 eV, which is 0.36 eV higher than the excess energy explains why at threshold energies, water did not evaporate during the fragmentation process and therefore fragment water clusters were observed. At higher photon energies, above the threshold, fragment water clusters are still observed. The clusters in the molecular beam may have argon clusters around them, which may evaporate with the excess energy. Previous work looking at argon water clusters detected $(H_2O)_m^+$ and $(H_2O)_mH^+$, but did not detect $Ar_n(H_2O)_m^+$ or $Ar_n(H_2O)_mH^+$. At threshold, the excess energy was 0.2 eV and the binding energy converged to roughly 30 meV. This excess energy upon ionization is enough to evaporate 7 argon molecules, which explains the lack of detected argon water clusters [81]. This argon water cluster finding lends support to the idea that the excess energy, when above the threshold of the EG water clusters, goes into evaporating argon clusters rather than evaporating the water cluster surrounding EG, shown in figure 6.6. The appearance of these EG water clusters indicates that, at least on the time scale of detection, the water clusters are not observing the ionization and fragmentation processes of EG.

The decrease in appearance energy as water clusters around fragments m/z 31 and m/z 32 indicates that the interaction between the water and EG is affecting some step of the ionization and fragmentation processes. It is hypothesized that fragment m/z 31 forms from a cyclic transition state when VUV light breaks the C-C bond of EG.

A suggested potential energy surface for the formation of this fragment is shown in figure 6.11. This is based upon the appearance energy for fragment m/z 31 clusters being higher than the vertical ionization energy of EG. The appearance energy is calculated theoretically following equation 6.4 where m, n, and k represent the number of water molecules in the cluster and E is the electronic energy calculated at ωB97X-V/def2-

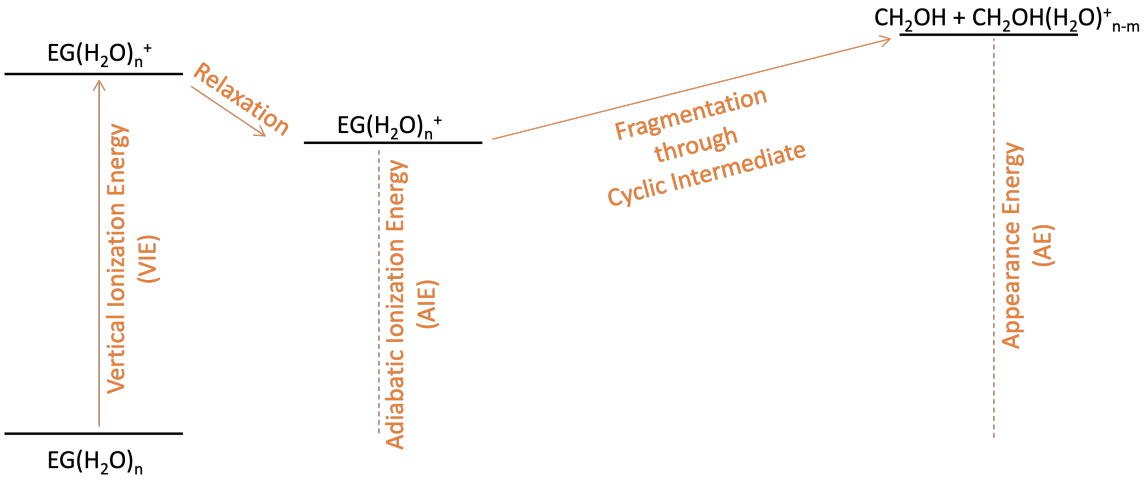


Figure 6.11. Potential energy surface for the fragmentation process of EG water clusters forming m/z 31 water clusters. This process is hypothesized to occur through a cyclic intermediate.

TZVPPD level of theory using Q-Chem [74].

$$AE(m/z31(H_2O)_n^+) = E(m/z31(H_2O)_m) + E(m/z31(H_2O)_n^+) - E(m/z62(H_2O)_k) \quad (6.4)$$

The size of the EG water cluster producing the observed fragments is unknown, so the appearance energy for the clusters was determined using different sized EG water clusters. The determined values are shown in table 6.5. Table 6.5 shows that the size of the

Table 6.5. Calculated appearance energy for m/z $31(H_2O)_n^+$. This table indicates that the final product is the determining factor in the energy, rather than the size of the reactant EG water cluster.

| | m/z $31^+$ | m/z $31(H_2O)^+$ | m/z $31(H_2O)_2^+$ | m/z $31(H_2O)_3^+$ | m/z $31(H_2O)_4^+$ |
|---|---|---|---|---|---|
| EG | 11.31 | - | - | - | - |
| EG$(H_2O)$ | 11.39 | 10.33 | - | - | - |
| EG$(H_2O)_2$ | 11.41 | 10.52 | 9.88 | - | - |
| EG$(H_2O)_3$ | 11.29 | 10.43 | 9.96 | 9.54 | - |
| EG$(H_2O)_4$ | 11.24 | 10.32 | 9.88 | 9.62 | 9.31 |

reactant EG water cluster does not determine the energy of the fragment cluster; rather, this energy is determined based upon the size of the fragment cluster. The calculated appearance energies in table 6.5 show the experimentally seen downward trend as the size

of the cluster increases and the roughly 1 eV drop in AE with the addition of one water to fragment m/z 31.

## 1,2- and 1,3-Propylene Glycol Water Clusters

As a comparison with EG and to see how the addition and placement of a methyl group affects photoionization, the VUV photoionization of 1,2-propylene glycol and 1,3-propylene glycol was performed. Similarly to the EG experiments, the concentration of 1,2-propylene glycol to water and 1,3-propylene glycol to water was adjusted by changing the temperature of the nozzle as well as the pressure of the backing Ar gas. Mass spectra taken at photon energies of 10.5 and 12.5 eV with different mole fractions of 1,2- and 1,3-propylene glycol are shown in the SI in figures 6.30 (12PG, 10.5 eV), 6.31 (12PG, 12.5 eV), 6.32 (13PG, 10.5 eV), and 6.33 (13PG, 12.5 eV). The mass spectrum taken at 12.5 eV with 52% 1,2-propylene glycol is shown in figure 6.12. Monomer and dimer protonated propylene glycol water clusters are indicated as well as the protonated propylene glycol trimer. The mass spectrum taken at 12.5 eV with 12% 1,3-propylene glycol is shown in figure 6.13. The observed cluster series m/z 31$(H_2O)_n^+$, PG$(H_2O)_n^+$, PG$_2(H_2O)_n^+$ are indicated.

The observed fragments for 1,2-propylene glycol are the same as those for EG with the addition of m/z 63, which is attributed to protonated EG. 1,3-propylene glycol has similar fragmentation to the other two diols, with the exception of fragment m/z 61 and the addition of fragments m/z 57, 59, 60, and 75. These differences in fragmentation show that the addition of a methyl group as well as the location of this methyl group affect fragmentation. This methyl group effects hydrogen bonding in the cyclic transition state which then effects what fragments can form.

Figure 6.14 shows the sum of the cluster series as a function of the 1,2-propylene glycol mole fraction taken at 12.5 eV. Unlike what was seen with EG, as the concentration of 1,2-propylene glycol increases, the intensity for only 1,2-propylene glycol clusters and $PG_3H^+$ (m/z 229) increases while for all other clusters the intensity decreases. This decreasing trend follows the depletion of water that was also observed when glycerol water clusters were photoionized [3]. This decrease suggests that clusters m/z 31$(H_2O)_n^+$, m/z 63$(H_2O)_n^+$,

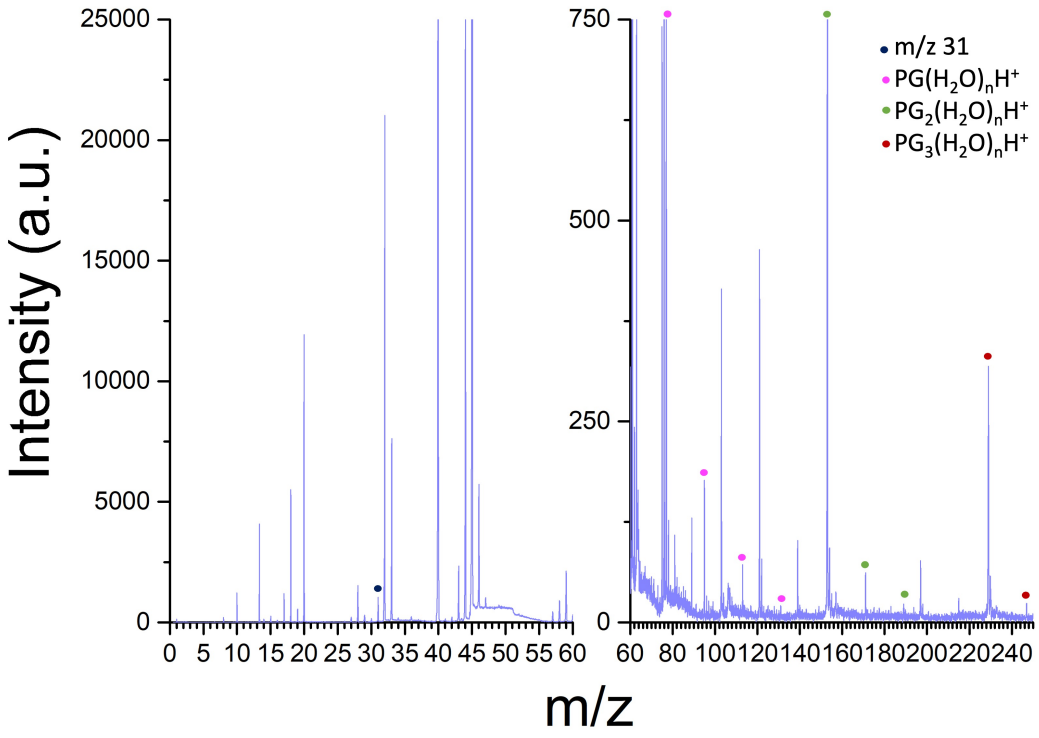


Figure 6.12. 52% 1,2-propylene glycol mass spectrum taken at 12.5 eV showing monomer and dimer protonated propylene glycol water clusters as well as the protonated propylene glycol trimer.

m/z 77$(H_2O)_n^+$, and m/z 153$(H_2O)_n^+$ are directly involved in the photoionization dynamics of 1,2-propylene glycol water clusters.

Table 6.6 shows the appearance energies for fragments and clusters resulting from the 1,2-propylene glycol water molecular beam and table 6.7 shows appearance energies from the 1,3-propylene glycol water molecular beam.

Both propylene glycols are observed to form fragments with mass 31, just as was observed with EG. 1,2-propylene glycol does show a slight drop in appearance energy as more water clusters around it, but nothing like what was seen in EG. 1,3-propylene glycol does not show any drop in appearance energy with the addition of water to fragment m/z 31. This difference is attributed to the addition of a methyl group, and in the case of 1,3-propylene glycol, the location of the methyl group between the hydroxyl groups affecting hydrogen bonding and the transition state that forms before or during the photoionization

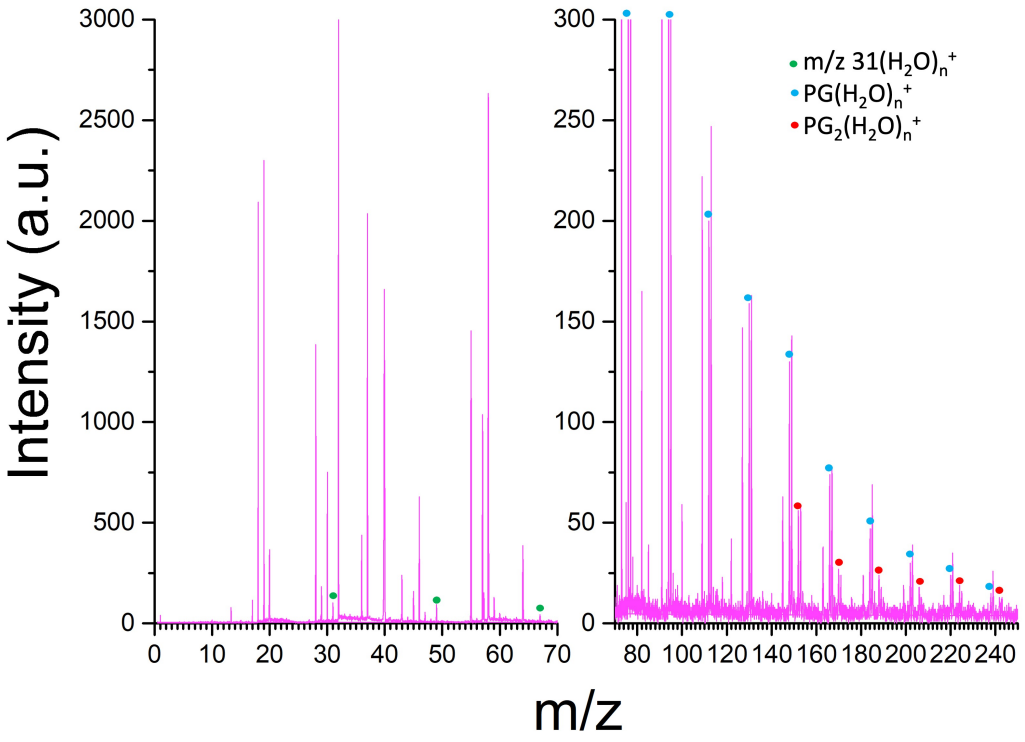


Figure 6.13. Mass spectrum taken with 12% 1,3-propylene glycol in the molecular beam at a photon energy of 12.5 eV. The cluster series for $m/z31(H_2O)_n^+$, $PG(H_2O)_n^+$, and $PG_2(H_2O)_n^+$ are shown.

process.

A similar trend in decreasing AE was observed for certain fragment water clusters formed when glycerol water clusters were photoionized. Fragments m/z 61, 62, and 74 were found to form clusters with water. No trend was observed for fragment m/z 31, as this fragment was not detected, though the formation of this fragment was predicted, by theory, to be barrierless [3]. The appearance energies of the fragment clusters m/z $62(H_2O)_n^+$ and m/z $74(H_2O)_n^+$ are close to that of pure glycerol (AE = 9.4 eV [3]) and show a change of 0.1 eV, which is within the experimental error, as more water molecules cluster around the fragment. Fragment m/z 61 showed a decrease in appearance energy of 0.3 eV with the addition of 1 water molecule, which is larger than was seen with the other fragments but small compared with what was seen with fragment m/z 31 from EG. The decrease in energy with addition of water was on the order of that observed

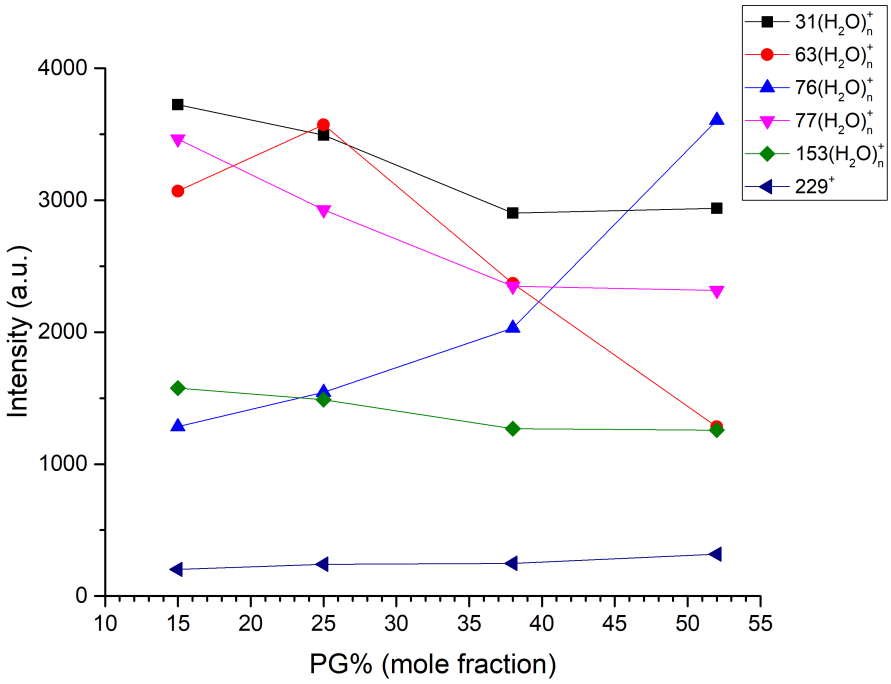


Figure 6.14. Sum of intensities of each cluster series as a function of 1,2-propylene glycol mole fraction, recorded at 12.5 eV. Unlike with EG, as the concentration of 1,2-propylene glycol increases, the intensity of 1,2-propylene glycol clusters and $PG_3H^+$ increases while the intensity for all other clusters decreases.

for fragmentation of 1,2-propylene glycol. For comparison, the optimized geometries of neutral (top) and cation (bottom) EG, 1,2-propylene glycol, 1,3-propylene glycol, and glycerol [3] are shown in figure 6.15. These were optimized with Q-Chem at the $\omega$B97X-V/def2-TZVPPD level of theory. Figure 6.15 shows how the hydrogen bonding between water and the alcohol changes with ionization. Before ionization, all alcohols form at least two hydrogen bonds with water. These hydrogen bonds are between 1.87 and 2.1 Å. Upon ionization, a hydrogen bond between both propylene glycols and water and between glycerol and water is severed. In these three cases, when ionized, the alcohol acts as a hydrogen bond donor, and the water drifts closer to one hydroxyl group. For 1,2-propylene glycol, the hydrogen bond that remains goes from 1.935 Å to 1.591 Å, and the severed hydrogen bond is 1.886 Å long. For 1,3-propylene glycol, the hydrogen bond that remains goes from 1.938 Å to 1.551 Å, and the severed hydrogen bond is 2.029 Å long. For glycerol, the hydrogen bond that remains goes from 1.903 Å to 1.609 Å, and

Table 6.6. Experimental appearance energies in eV of 1,2-propylene glycol clusters as well as observed fragments and fragment clusters taken at a propylene glycol mole fraction of 12%. The error is ±0.01. Using an effusive heater, the AE for 1,3-propylene glycol was found to be 9.80 ± 0.1 eV, which nicely matches this experimental data. A - indicates that the signal to noise ratio was not good enough to obtain a conclusive AE value.

| | 12% |
|---|---|
| m/z $27^+$ | 9.6 |
| m/z $29^+$ | 9.5 |
| m/z $30^+$ | 10.5 |
| m/z $31^+$ | 11.1 |
| m/z $31(H_2O)^+$ | 10.8 |
| m/z $31(H_2O)_2^+$ | 10.5 |
| m/z $31(H_2O)_3^+$ | 10.4 |
| m/z $31(H_2O)_4^+$ | 10.1 |
| m/z $31(H_2O)_5^+$ | 9.6 |
| m/z $31(H_2O)_6^+$ | 9.5 |
| m/z $31(H_2O)_7^+$ | 9.5 |
| m/z $31(H_2O)_8^+$ | 9.5 |
| m/z $31(H_2O)_9^+$ | 9.5 |
| m/z $31(H_2O)_{10}^+$ | 9.5 |
| m/z $33^+$ | 10.1 |
| m/z $43^+$ | 10.0 |
| m/z $44^+$ | 10.1 |
| m/z $45^+$ | 10.3 |
| m/z $63^+$ ($EGH^+$) | 9.6 |
| m/z $63(H_2O)^+$ | 9.7 |
| m/z $63(H_2O)_2^+$ | 9.5 |
| m/z $63(H_2O)_3^+$ | 9.5 |
| m/z $63(H_2O)_4^+$ | 9.5 |
| m/z $76^+$ $(PG)^+$ | 9.7 |
| m/z $76(H_2O)^+$ | 9.5 |
| m/z $76(H_2O)_2^+$ | 9.5 |
| m/z $77^+$ ($PGH^+$) | 10.4 |
| m/z $77(H_2O)^+$ | 11.0 |
| m/z $77(H_2O)_2^+$ | 11.0 |
| m/z $77(H_2O)_3^+$ | 11.0 |
| m/z $77(H_2O)_4^+$ | 11.0 |
| m/z $77(H_2O)_5^+$ | 11.0 |
| m/z $77(H_2O)_6^+$ | 11.0 |
| m/z $153^+$ ($PG_2H^+$) | 9.5 |
| m/z 153 $(H_2O)^+$ | 9.5 |
| m/z 153 $(H_2O)_2^+$ | 10.2 |
| m/z 153 $(H_2O)_3^+$ | 10.3 |
| m/z 153 $(H_2O)_4^+$ | 11.1 |
| m/z 153 $(H_2O)_5^+$ | 11.1 |
| m/z 229 ($PG_3H^+$) | 9.5 |

the severed hydrogen bond is 1.896 Å long. Ethylene glycol, which contains one fewer methyl group than the propylene glycols and one fewer methyl group and hydroxyl group

Table 6.7. Experimental appearance energies in eV of 1,3-propylene glycol clusters as well as observed fragments and fragment clusters taken at a 1,3-propylene glycol mole fraction of 30% (from 85*C). The error is ±0.01 Using an effusive heater, the AE for 1,3-propylene glycol was found to be 9.75 ± 0.05 eV, which nicely matches this experimental data. A - indicates that the signal to noise ratio was not good enough to obtain a conclusive AE value.

| | 30% |
|---|---|
| m/z 31 | 11.3 |
| m/z 31$(H_2O)^+$ | 11.2 |
| m/z 31$(H_2O)_2^+$ | 11.2 |
| m/z 31$(H_2O)_3^+$ | - |
| m/z 43 | 10.2 |
| m/z 44 | 10.2 |
| m/z 45 | 10.0 |
| m/z 57 | 10.7 |
| m/z 59 | 10.0 |
| m/z 60 | 10.0 |
| m/z 75 | 10.9 |
| m/z 76 (PG) | 9.7 |
| m/z 76$(H_2O)^+$ | 9.8 |
| m/z 76$(H_2O)_2^+$ | - |
| m/z 77 (PGH) | 9.8 |
| m/z 77$(H_2O)^+$ | 9.8 |
| m/z 77$(H_2O)_2^+$ | 9.8 |
| m/z 77$(H_2O)_3^+$ | - |
| m/z 152 ($PG_2$) | 9.7 |
| m/z 152 $(H_2O)^+$ | 9.6 |
| m/z 152 $(H_2O)_2^+$ | - |
| m/z 153 ($PG_2H$) | 9.6 |
| m/z 153 $(H_2O)^+$ | 9.6 |
| m/z 229 ($PG_3H$) | 9.7 |

than glycerol, undergoes a proton transfer when ionized. This proton is shared between the hydroxyl group and water, similar to a Zundel ion. The lower propensity of propylene glycol and glycerol to bind to water when ionized is attributed to the additional methyl group when compared with ethylene glycol.

The fragmentation process, upon VUV photoionization, of pure glycerol occurs through either a six-membered hydrogen transfer transition state forming a stable ternary intermediate or through elongation of the C-C bond. Similar cyclic hydrogen bond transition structures were found to be involved in the fragmentation process, upon VUV photoionization, of glycerol water clusters [3] and deoxyribose [69]. The fragmentation of the diol water clusters is proposed to occur through similar cyclic hydrogen bond transition states as well as via C-C bond elongation. The cyclic hydrogen bond transition state that can

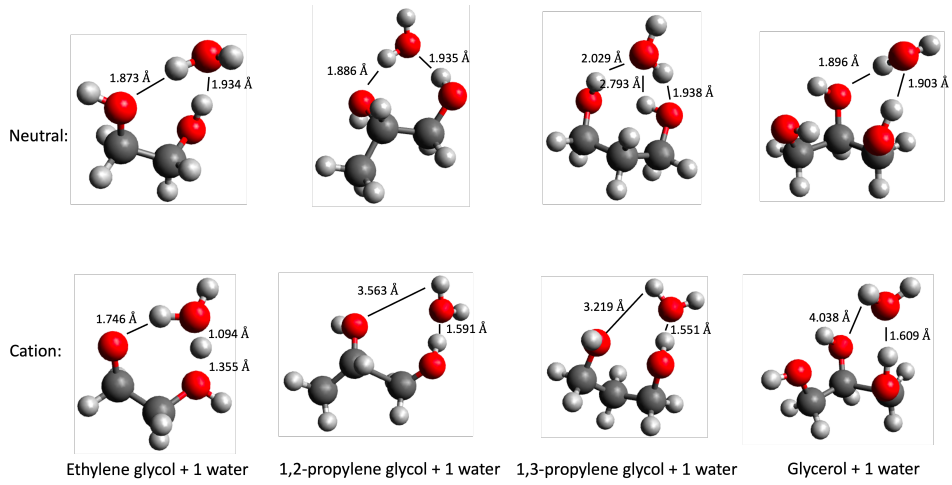


Figure 6.15. Optimized geometry of neutral (top row) and cation (bottom row) EG, 1,2-propylene glycol, 1,3-propylene glycol, and glycerol [3] with the hydrogen bond lengths given. The optimization was done using Q-Chem at the ωB97X-V/def2-TZVPPD level of theory.

form is dependent upon the location of the hydroxyl groups on the diol, which explains the difference in fragments observed for the three diols as well as the difference in appearance energy trends between these diols.

The combination of diol with water is found to change the ionization mechanism for both the water and the diol. In general, cationic diols are found to have a lower propensity for binding to water than neutral diols, as shown in figure 6.15 by the severing of one hydrogen bond when ionized. This finding is supported by previous theory calculations that found that the EG water interaction is dominant over EG EG and water water interactions, indicating that the presence of water disrupts EG EG hydrogen bonding [70]. By understanding the effect water has upon ionization mechanisms and fragmentation of the diols EG, 1,2-propylene glycol, and 1,3-propylene glycol, reactions occurring on the icy mantles of dust grains in the ISM can be better understood and predicted. Based upon these findings, cationic diols and alcohols in general will bind less to water when ionized and will require less energy to fragment when surrounded by water. These findings are based on small clusters of water surrounding the alcohol. To fully understand the reaction dynamics occurring in the ISM, further studies involving ice and these diols along with calculations simulating a full surface of water are needed, such as has been done with

some polycyclic aromatic hydrocarbons trapped onto cryogenic water-ice [82].

# Conclusions

EG, 1,2-propylene glycol, and 1,3-propylene glycol water clusters were photoionized using tunable VUV radiation (in the range 9.0 to 12.5 eV) and the products were detected using reflectron time-of-flight mass spectrometry. Water clustered around the diols as well as fragments of the diols were detected, indicating that through the fragmentation process not all water surrounding the diol evaporates. The detected fragments differed for the three diols. EG and 1,2-propylene glycol exhibited similar fragmentation both forming fragments m/z 31, 32, 33, 43, 44, 45, 61 and 1,2-propylene glycol formed fragment m/z 63. 1,3-propylene glycol exhibited somewhat different fragmentation forming fragments m/z 31, 32, 43, 44, 45, 57, 59, 60, 75. This difference is due to the addition and location of the methyl group. From the mass spectra, photoionization intensity curves were determined, and from this, the appearance energies (AE) for the clusters were obtained. AE for the unfragmented diol water clusters was found to show little variation with cluster size. A small decrease in AE was observed as cluster size increased, similar to what was observed with glycerol water clusters [3]. The formation of fragment clusters through dissociative ionization was found to be affected by the number of methyl groups and the placement of hydroxyl groups with respect to these methyl groups. In the case of EG, forming m/z $31(H_2O)_n^+$ takes roughly 1 eV less energy than forming m/z 31. With the addition of 1 methyl group to the end of EG, forming 1,2-propylene glycol, fragmentation to produce m/z $31(H_2O)_n^+$ takes 0.3 eV less than producing m/z 31. When the hydroxyl group is moved to the added methyl, in the case of 1,3-propylene glycol, no change in energy needed to form m/z $31(H_2O)_n^+$ versus m/z 31 is observed. This indicates that methyl group and hydroxyl group location play a large role in the energy needed to undergo dissociative photoionization when water is present. This is attributed to the formation of a cyclic hydrogen-bonded transition state, similar to that observed for glycerol water clusters and deoxyribose.

# Supplemental Information (SI)

Photoionization intensity curves:

Figure 6.16 - m/z 31$(H_2O)_n^+$, from ethylene glycol water clusters

Figure 6.17 - m/z 32$(H_2O)_n^+$, from ethylene glycol water clusters

Figure 6.18 - EG$_n(H_2O)_m^+$, from ethylene glycol water clusters

Figure 6.19 - EG$(H_2O)_nH^+$, from ethylene glycol water clusters

Figure 6.20 - EG2$(H_2O)_nH^+$, from ethylene glycol water clusters

Figure 6.21 - EG3$(H_2O)_nH^+$, from ethylene glycol water clusters

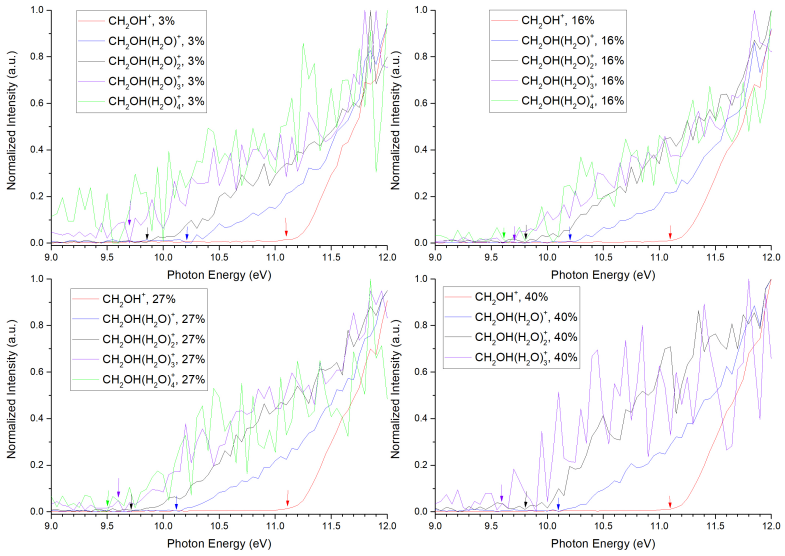


Figure 6.16. Photoionization intensity curves for m/z 31$(H_2O)_n^+$

Figure 6.22 - fragments from 1,2-propylene glycol water clusters

Figure 6.23 - 1,2-propylene glycol water clusters

Figure 6.24 - fragments from 1,3-propylene glycol water clusters

Figure 6.25 - 1,3-propylene glycol water clusters

In table 6.8 the appearance energies for 1,2-propylene glycol and 1,3-propylene glycol are given. These were obtained through effusive heating (eff) of pure 1,2-propylene glycol and 1,3-propylene glycol and and a supersonic beam (sup) of pure 1,2-propylene glycol

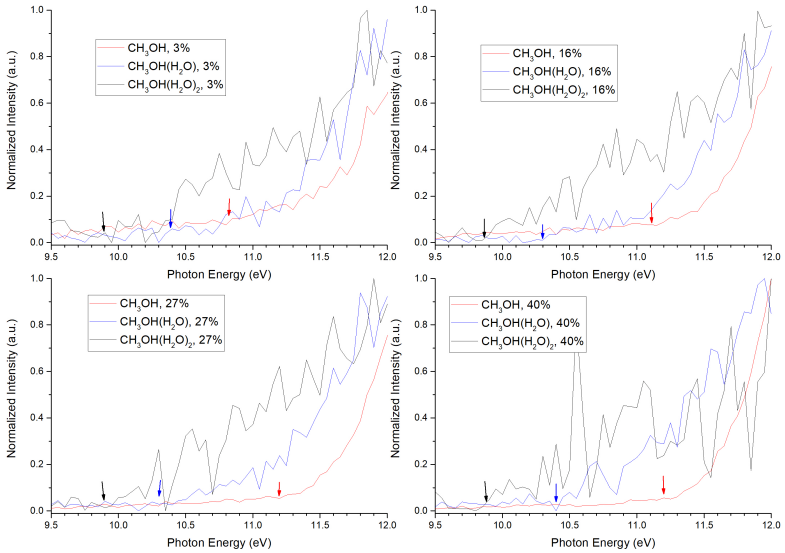


Figure 6.17. Photoionization intensity curves for m/z 32$(H_2O)_n^+$

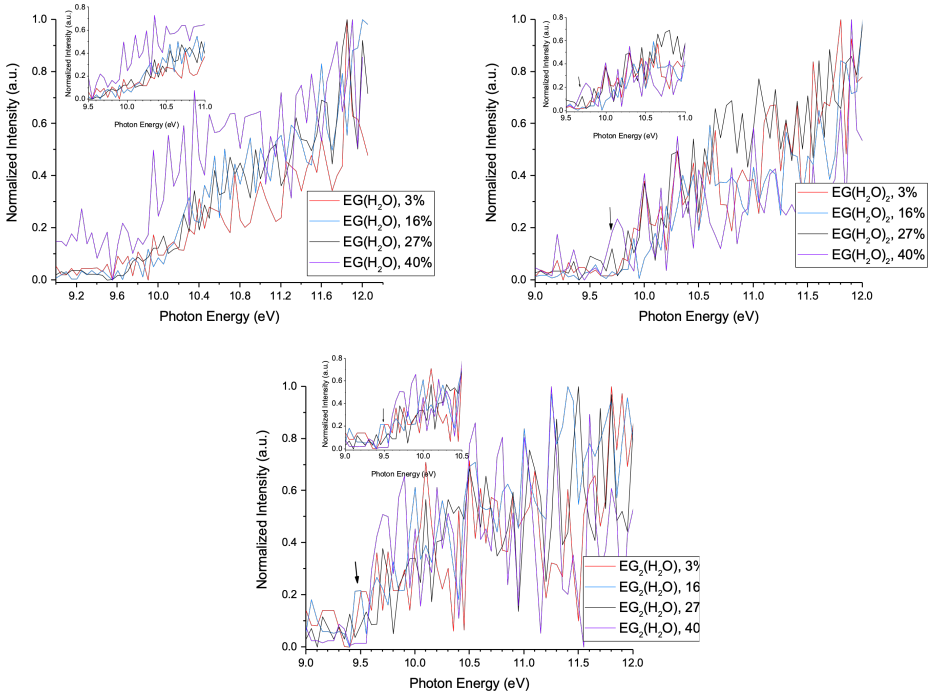


Figure 6.18. Photoionization intensity curves for $EG_n(H_2O)_m^+$

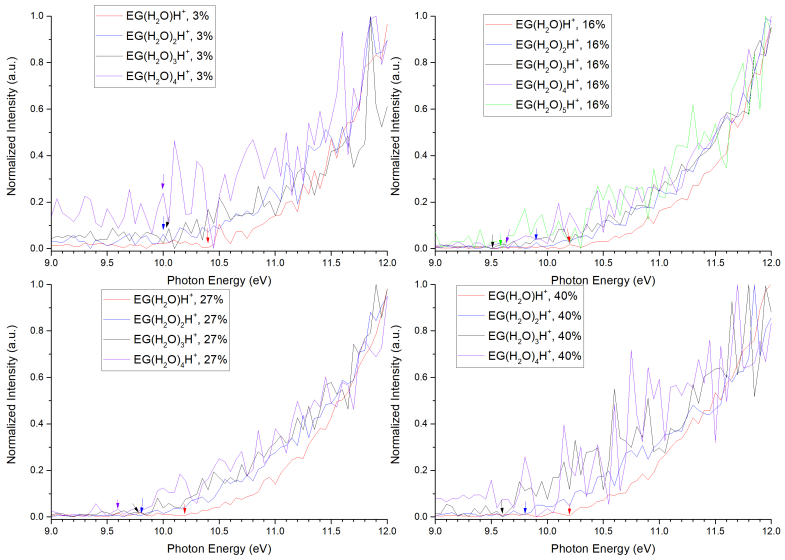


Figure 6.19. Photoionization intensity curves for $\mathrm{EG}(H_2O)_nH^+$

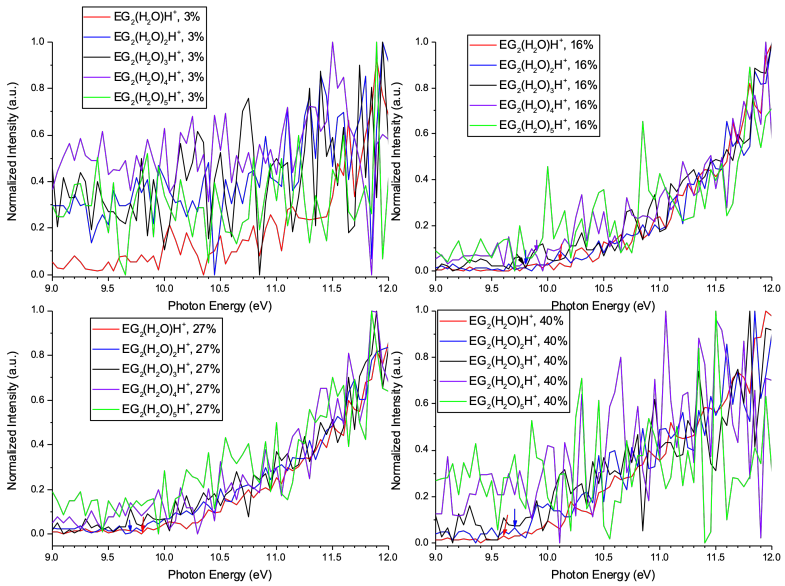


Figure 6.20. Photoionization intensity curves for $\mathrm{EG}_2(H_2O)_nH^+$

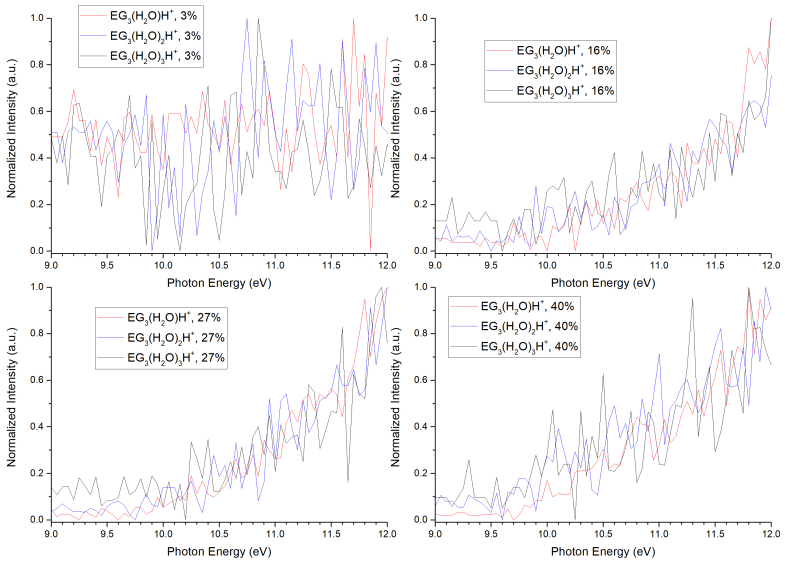


Figure 6.21. Photoionization intensity curves for $\mathrm{EG}_3(H_2O)_nH^+$

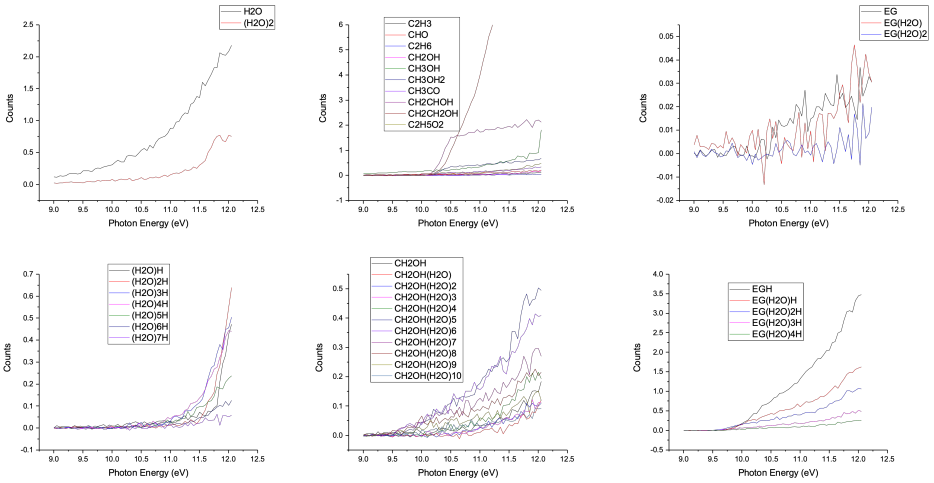


Figure 6.22. Photoionization intensity curves for fragments from 1,2-propylene glycol water clusters

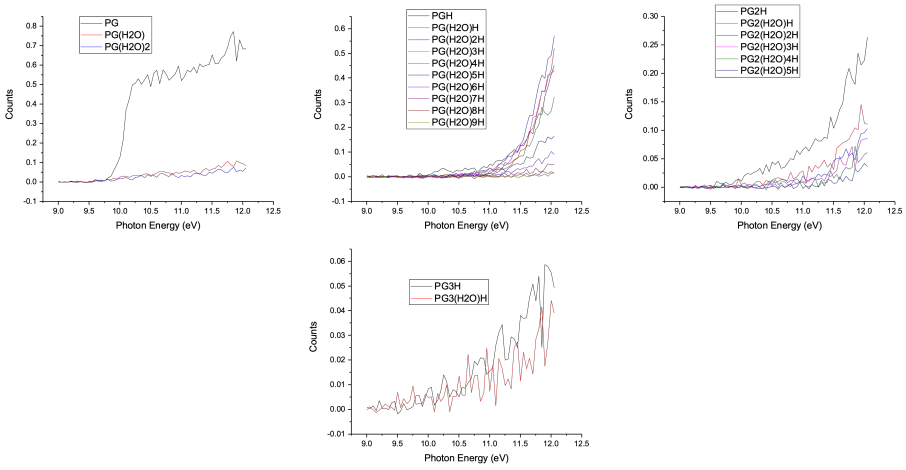


Figure 6.23. Photoionization intensity curves for 1,2-propylene glycol water clusters

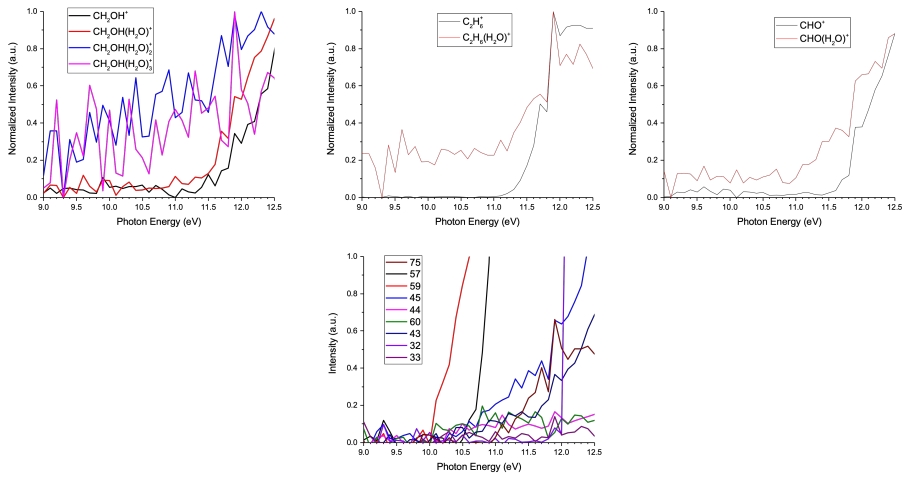


Figure 6.24. Photoionization intensity curves for fragments from 1,3-propylene glycol water clusters

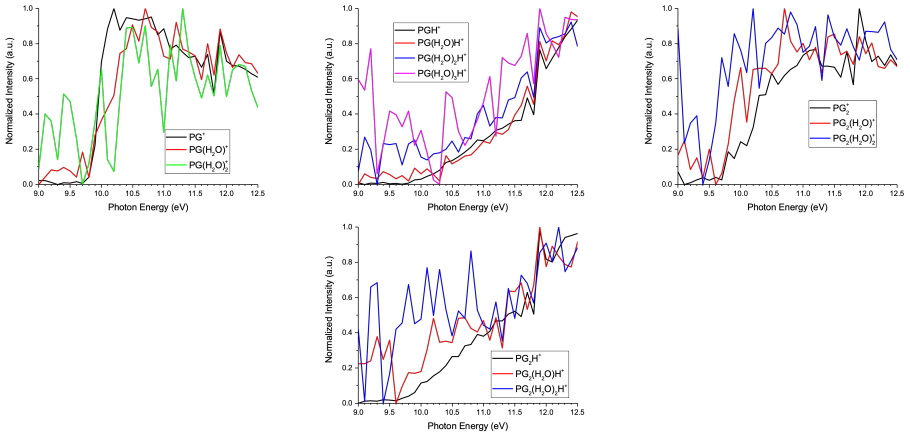


Figure 6.25. Photoionization intensity curves for 1,3-propylene glycol water clusters

and 1,3-propylene glycol. Due to the lack of water, the values seen here differ from those given in the paper for diol water clusters. When 2 numbers are given, the first is the appearance energy for the species and the second is the a new channel opening up.

Table 6.8. Appearance energies for pure 1,2-propylene glycol and 1,3-propylene glycol obtained previously through effusive heating (eff) and a supersonic beam (sup). When 2 numbers are given, the first is the appearance energy for the species and the second is the a new channel opening up.

| | Appearance Energy (eV) | | | |
|---|---|---|---|---|
| | 1,2 | | 1,3 | |
| | Eff (±0.1) | Sup (±0.2) | Eff (±0.05) | Sup (±0.2) |
| Parent $C_3H_8O_2$, m/z 76 | 9.80, 10.82 | 9.86 | 9.75, 10.40 | 9.80 |
| Lost $H_2O$, $C_3H_5O_2$, m/z 58 | 9.91 | 9.99 | 10.00, 10.47 | 10.04 |
| Lost $H_3O$, $C_3H_5O_2$, m/z 57 | | | 10.54, 10.79 | 10.58, 10.80 |
| $C_2H_6O$, m/z 46 | 10.32 | 10.31 | 10.55, 10.83 | 10.47, 11.00 |
| Lost $H_2O$ and $CH_2O$, m/z 30 | | | 11.02, 11.40 | 11.04, 11.35 |
| Lost $H_2O$, H CHO, m/z 29 | | | 11.68, 12.76 | 11.59 |
| Lost $H_2O$ and $CH_2O$, m/z 28 | | | 11.50, 12.04 | 11.48 |

The intensity of the clusters as a function of cluster size and photon energy are shown for the fragment clusters in figure 6.26, for EG and protonated EG clusters in figure 6.27, for dimer protonated and unprotonated clusters in figure 6.28 and for protonated trimer

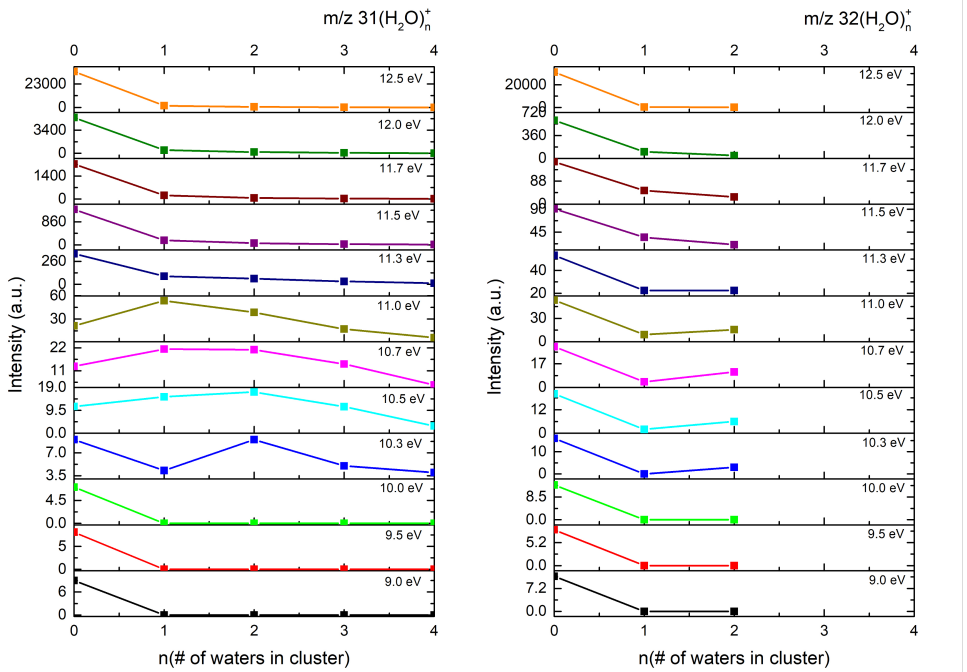


Figure 6.26. Intensity of fragment m/z 31 and m/z 32 clusters as a function of cluster size and photon energy (eV)

ethylene glycol clusters in figure 6.29. From this, it can be seen that the intensities of the clusters increase with photon energy (highest at 12.5 eV).

Figure 6.30 shows mass spectra taken with a photon energy of 10.5 eV at 15%, 25%, 38%, 52%, and 100% mole fractions of 1,2-propylene glycol. Figure 6.31 shows mass spectra taken with a photon energy of 12.5 eV at 15%, 25%, 38%, and 52% mole fractions of 1,2-propylene glycol. In both figures propylene glycol water clusters are indicated as well as protonated dimer and trimer propylene glycol.

Figure 6.32 shows mass spectra taken with a photon energy of 10.5 eV at 9%, 12%, 20%, 30%, and 42% mole fraction of 1,3-propylene glycol. Figure 6.33 shows mass spectra taken with a photon energy of 12.5 eV at 9%, 12%, 20%, 30%, and 42% mole fraction of 1,3-propylene glycol. Monomer, dimer and trimer, protonated and unprotonated 1,3-propylene glycol water clusters are indicated.

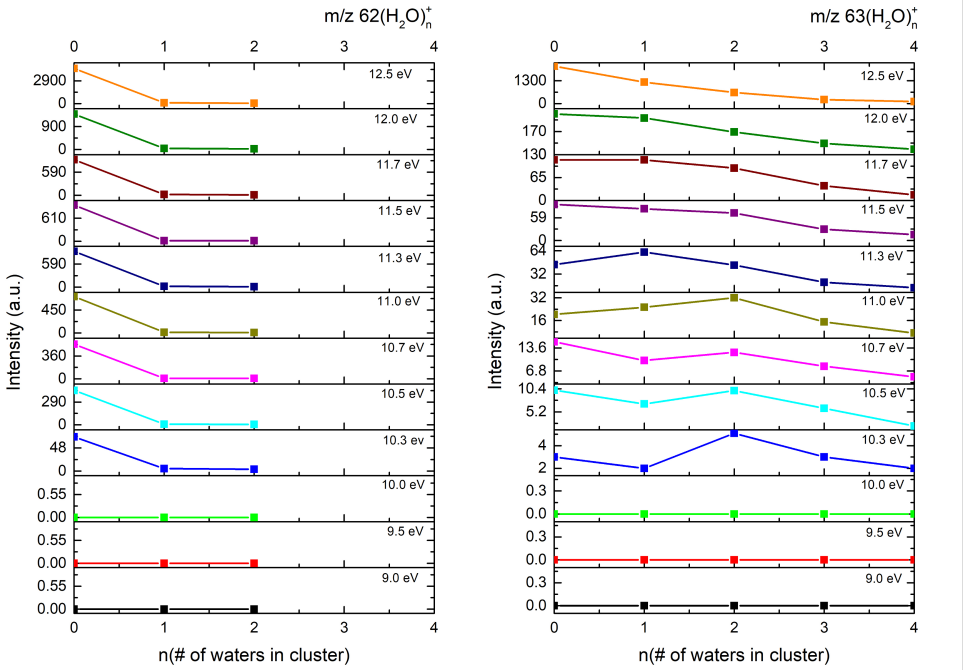


Figure 6.27. Intensity of EG and EGH clusters as a function of cluster size and photon energy (eV)

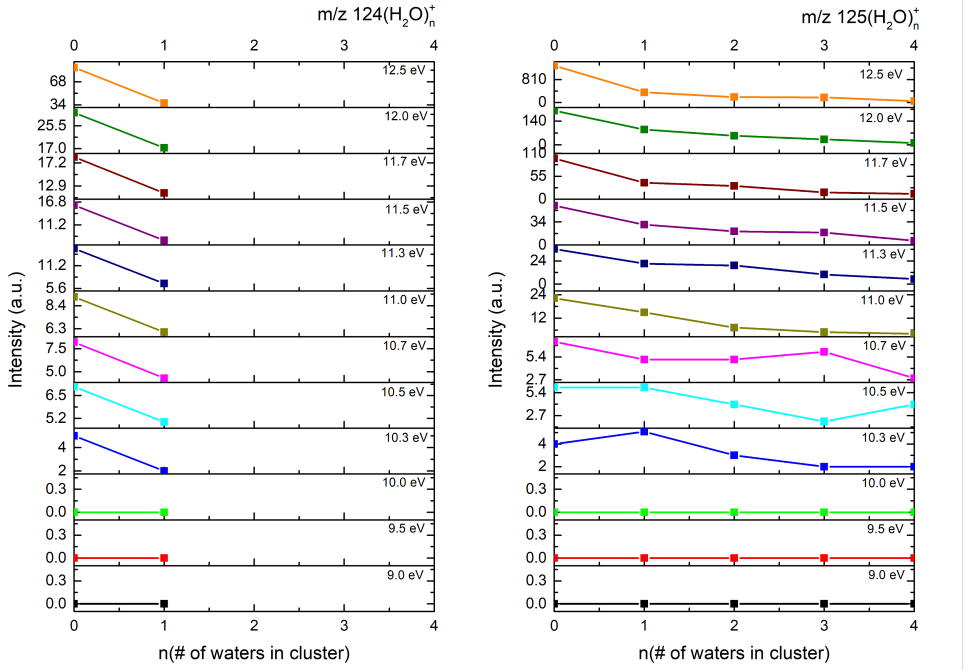


Figure 6.28. Intensity of dimer ethylene glycol and protonated dimer ethylene glycol clusters as a function of cluster size and photon energy (eV)

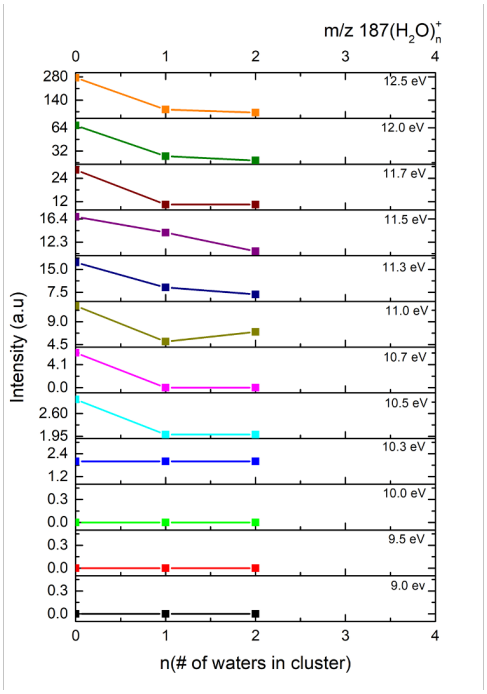


Figure 6.29. Intensity protonated trimer ethylene glycol clusters as a function of cluster size and photon energy (eV)

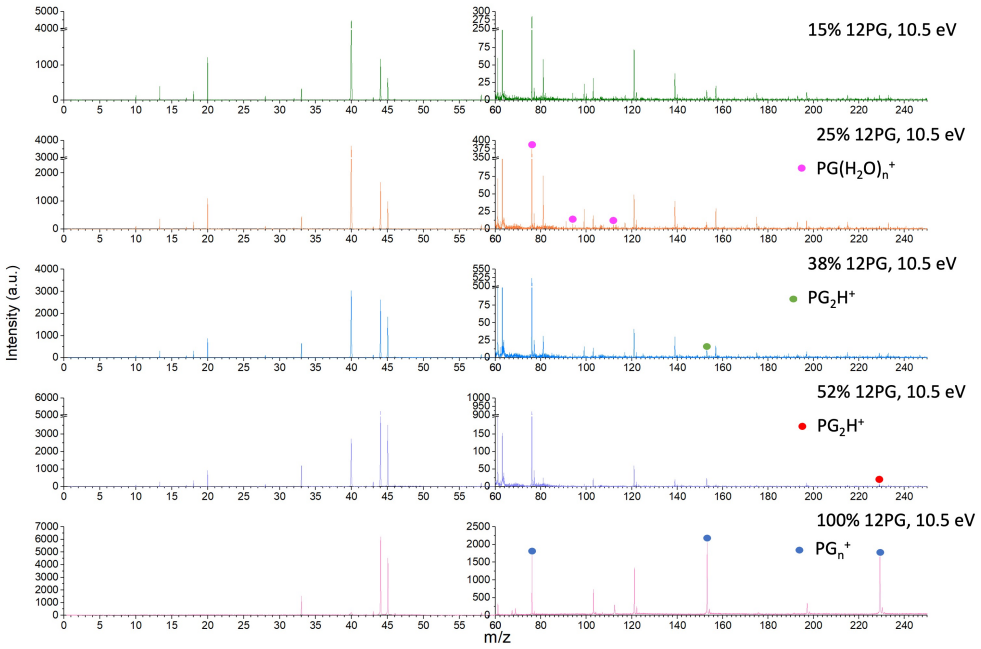


Figure 6.30. Mass spectra of 1,2-propylene glycol water clusters recorded at 10.5 eV with 1,2 propyolene glycol mole fraction 15%, 25%, 38%, and 52%, and 100%. The propylene glycol water cluster series is shown along with dimer and trimer prontonated propylene glycol.

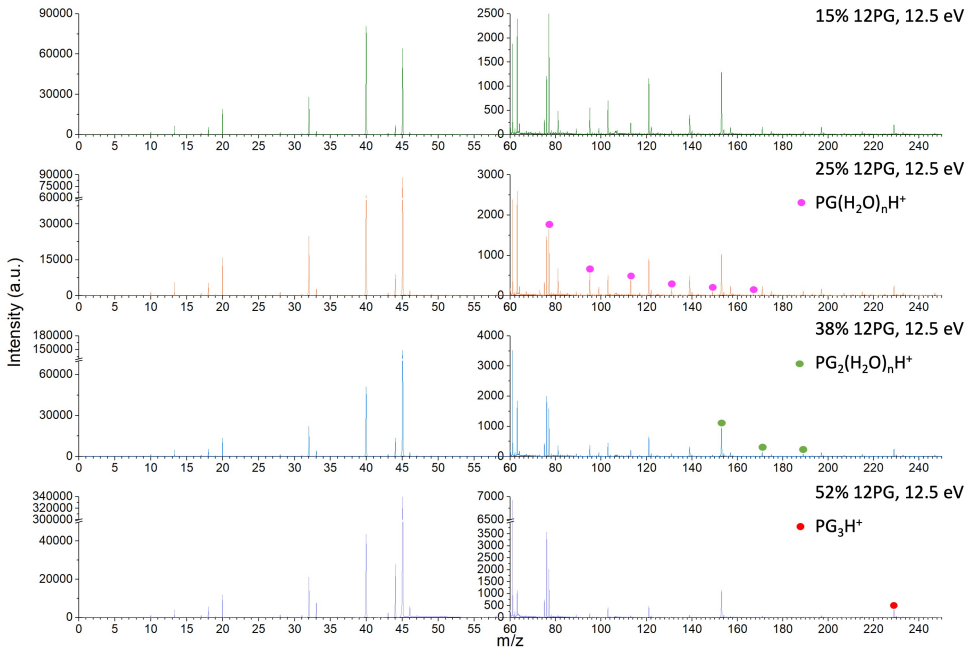


Figure 6.31. Mass spectra of 1,2-propylene glycol water clusters recorded at 12.5 eV with 1,2 propyolene glycol mole fractions 15%, 25%, 38%, and 52%. The propylene glycol water cluster series is shown along with dimer and trimer prontonated propylene glycol.

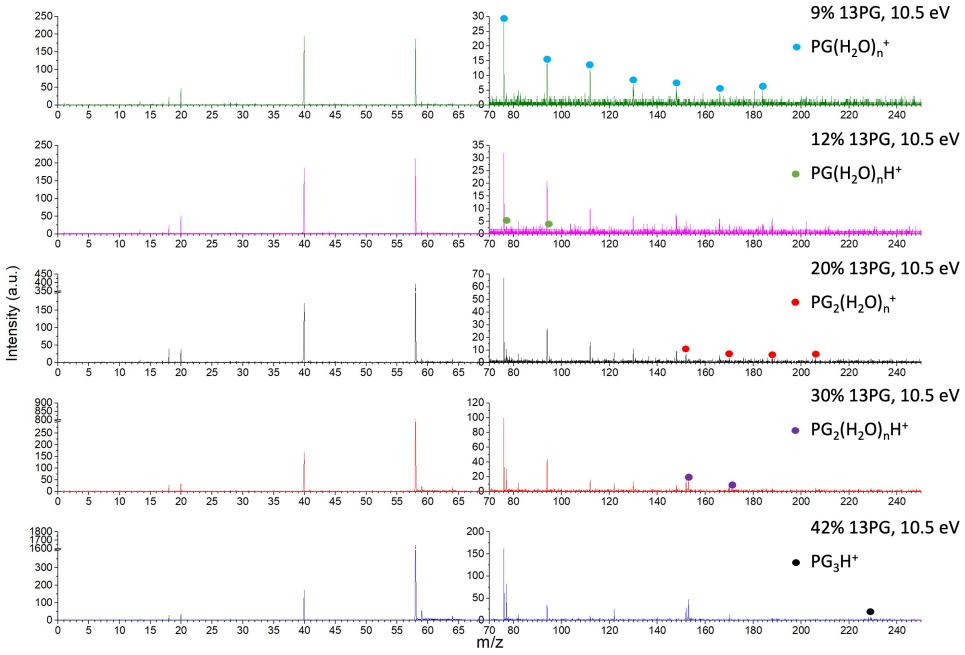


Figure 6.32. Mass spectra of 1,3-propylene glycol water clusters recorded at 10.5 eV and at 1,3-propylene glycol mole fractions 9%, 12%, 20%, 30%, and 42%. Monomer, dimer and trimer, protonated and unprotonated 1,3-propylene glycol water clusters are shown.

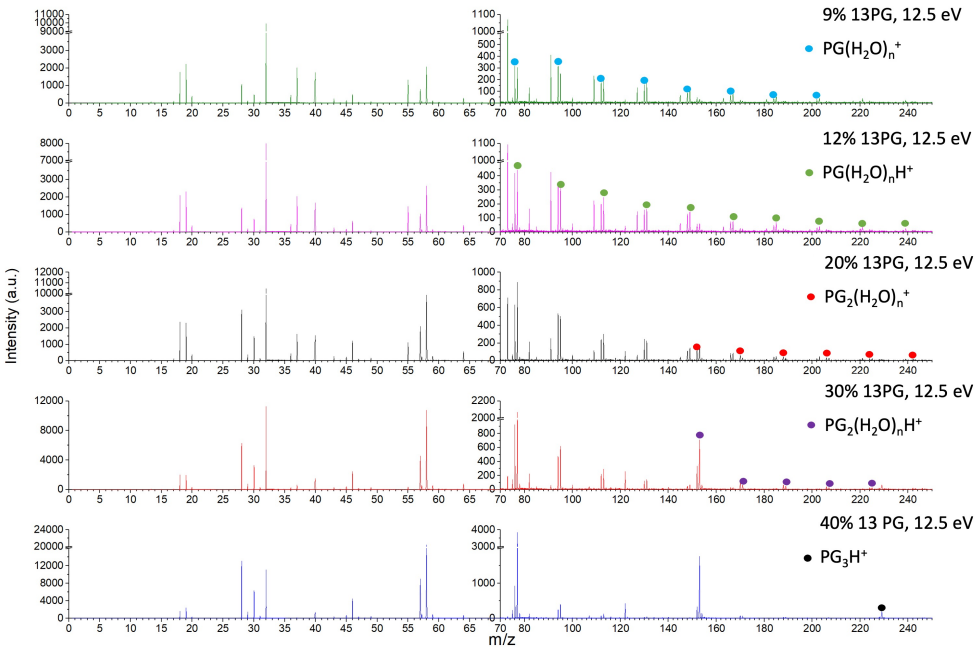


Figure 6.33. Mass spectra of 1,3-propylene glycol water clusters recorded at 12.5 eV and at 1,3-propylene glycol mole fractions 9%, 12%, 20%, 30%, and 42%. Monomer, dimer and trimer, protonated and unprotonated 1,3-propylene glycol water clusters are shown.

# Chapter 7

# Conclusions

Through my graduate school research, I have aimed to shed light on the origins of life. With this pursuit in mind, I worked on three different gas phase spectroscopy projects on three different apparatuses. These projects studied reactions and molecules involved in the formation of complex organic molecules (COMs), which may have provided much of the organic material in the solar system and are thought to have been involved in prebiotic chemistry on Earth.

In my first project, I performed two ion-molecule reactions, which, in the interstellar medium (ISM), are proposed to have formed small molecular precursors to COMs. In these reactions, I studied the chemical reactivity of vanadium cations excited to a specific quantum spin-orbit electronic state with methane and water, separately, as a function of the center of mass collision energy in the range 0.1 to 10.0 eV. The vanadium cation was prepared into the quantum spin-orbit states $a^5D_{0,2}$, $a^5F_{1,2}$, and $a^3F_{2,3}$. For the vanadium cation water reactions, the three observed product channels were $VO^+ + H_2, VH^+ + OH$, and $VOH^+ + H_2O$. For the reaction between vanadium cation and methane, the three observed product channels were $VH^+ + CH_3$, $VCH_2^+ + H_2$ and $VCH^+ + H$.

In both reactions, the triplet state, $a^3F_{2,3}$, was found to be more reactive than the quintet states, $a^5D_{0,2}, a^5F_{1,2}$, which is attributed to a weak quintet-to-triplet spin crossing mechanism and therefor a favoring of conservation of total electron spin. In the vanadium cation methane reaction, an inserted intermediate $HV^+CH_3$ also favored the triplet state. The distinct pathways for the various electronic states are attributed to weak spin-orbit

coupling. In both reactions, viable pathways to form $H_2$ were shown, providing insight into designing more effective catalysts for $H_2$ formation as well as $CH_4$ activation.

Larger molecules in the ISM are thought to form through radical-neutral or radical-radical reactions. To better predict these reactions, it is necessary to know what radicals are in the ISM. The spectra of radicals can be detected by radio telescopes and then identified by comparison with experimentally determined spectra. To aid in this detection, in my second project, I designed a new technique and built a new instrument that would selectively determine the rovibrational spectra of radicals. This technique combined cavity-enhanced frequency modulation spectroscopy with an AC magnetic field generated by a solenoid to achieve a sensitive, radical-selective, Doppler-free technique that we named Noise-Immune Cavity-Enhanced Optical Heterodyne Zeeman Modulation Spectroscopy (NICE-OHZMS). The instrument was built by modifing an existing instrument used for noise-immune cavity-enhanced optical heterodyne velocity modulation. The velocity modulation was replaced with Zeeman modulation through the addition of the AC audio amplifier-driven solenoid, shown in figure 7.1. To test the effectiveness of the

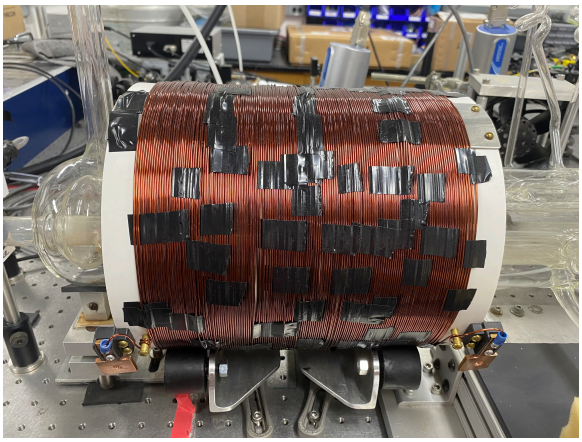

Figure 7.1. A picture of the AC audio-amplified solenoid, which produces the time-varying magnetic field used in the NICE-OHZMS technique to discriminate the spectra of radicals from those of closed shell molecules.

instrument and technique, proof-of-concept testing was performed with the radical (or open-shell molecule) NO as well as the closed-shell molecule $CO_2$. If working correctly, because of the Zeeman modulation, only the spectra of NO should appear. The spectra of $CO_2$ would be removed through the modulation process. A NICE-OHZMS spectra of

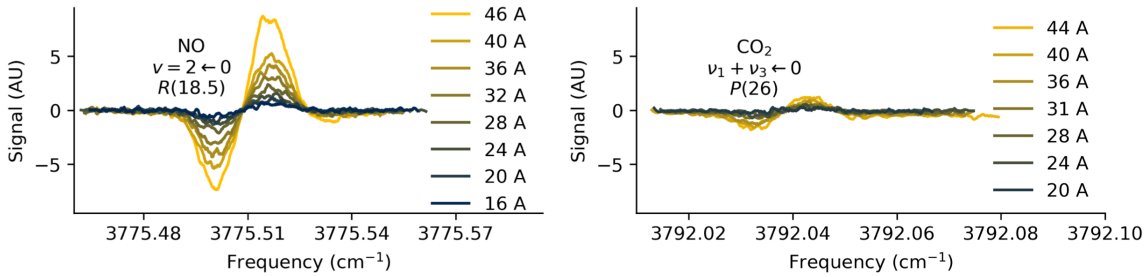


Figure 7.2. NICE-OHZMS spectra of NO and $CO_2$ as a function of current applied to the solenoid. For $NO$, the R(18.5) transition of the first overtone band is shown on the left and for $CO_2$ the P(26) transition of the $\nu_1 + \nu_3$ combination band is shown on the right.

NO and $CO_2$ taken at different applied currents is shown in figure 7.2. On the left, the R(18.5) transition of the first overtone band of NO is shown, and on the right, the P(26) transition of the $\nu_1 + \nu_3$ combination band of $CO_2$ is shown. Given the presence of the $CO_2$ transition, modifications and further testing are needed before this technique is fully realized. This further testing will be done by future graduate students.

In the ISM, molecules embed onto the icy mantles surrounding dust grains are ionized and potentially fragmented by vacuum ultraviolet (VUV) light. These ions and fragments may then go on to form COMs. The molecules in the ice, such as $CO_2$ and $H_2O$, may affect the reactivity and photoionization of the embedded molecules. As a proxy for studying this, the photoinization of ethylene glycol, 1,2-propylene glycol, and 1,3-propylene glycol water clusters was studied. These diol water clusters were generated in a continuous supersonic molecular beam, photoionized by synchrotron vacuum ultraviolet light from the Advanced Light Source, and subsequently detected by reflectron time-of-flight mass spectrometry. From the mass spectra, taken at increasing photon energy, the appearance energies for the detected clusters were determined. Clusters of both diol fragments and unfragmented diols with water were detected. Water clustered around the diols as well as fragments of the diols were detected, indicating that through the fragmentation process, not all the water surrounding the diol evaporates. The detected fragments differed for the three diols. Ethylene glycol and 1,2-propylene glycol exhibited similar fragmentation both forming fragments m/z 31, 32, 33, 43, 44, 45, 61 and 1,2-propylene glycol formed frag-

ment m/z 63. 1,3-propylene glycol exhibited somewhat different fragmentation forming fragments m/z 31, 32, 43, 44, 45, 57, 59, 60, 75. This difference is due to the addition and location of the methyl group. From the mass spectra, photoionization intensity curves were determined, and from this, the appearance energies (AE) for the clusters were obtained. AE for the unfragmented diol water clusters was found to show little variation with cluster size. A small decrease in AE was observed as cluster size increased, similar to what was observed with glycerol water clusters [3]. The formation of fragment clusters through dissociative ionization was found to be affected by the number of methyl groups and the placement of hydroxyl groups with respect to these methyl groups. In the case of ethylene glycol, forming m/z $31(H_2O)_n^+$ takes roughly 1 eV less energy than forming m/z 31. With the addition of 1 methyl group to the end of ethylene glycol, forming 1,2-propylene glycol, fragmentation to produce m/z $31(H_2O)_n^+$ takes 0.3 eV less than producing m/z 31. When the hydroxyl group is moved to the added methyl, in the case of 1,3-propylene glycol, no change in energy needed to form m/z $31(H_2O)_n^+$ versus m/z 31 is observed. This indicates that methyl group and hydroxyl group location play a large role in the energy needed to undergo dissociative photoionization when water is present. This is attributed to the formation of a cyclic hydrogen-bonded transition state, similar to that observed for glycerol water clusters and deoxyribose.

# References


[1] Gary C. Bjorklund. Frequency-modulation spectroscopy: a new method for measuring weak absorptions and dispersions. *Opt. Lett.*, 5(1):15–17, Jan 1980.

[2] Fourtier, Tara and Baumann, Esther. 20 years of developments in optical frequency comb technology and applications. *Commun Phys*, 2(153):1–16, 2019.

[3] Wenchao Lu, Cameron J. Mackie, Bo Xu, Martin Head-Gordon, and Musahid Ahmed. A computational and experimental view of hydrogen bonding in glycerol water clusters. *The Journal of Physical Chemistry A*, 126(10):1701–1710, 2022. PMID: 35254809.

[4] Hong Wang, Jiwen Guan, Jiao Gao, Yanbo Li, Jinyang Zhang, Xiaobin Shan, and Zhandong Wang. Discriminating between the dissociative photoionization and thermal decomposition products of ethylene glycol by synchrotron vuv photoionization mass spectrometry and theoretical calculations. *Phys. Chem. Chem. Phys.*, 24:26915–26925, 2022.

[5] Alma. https://www.almaobservatory.org/en/about-alma/how-alma-works/how-does-alma-see/. Accessed: July 14, 2023.

[6] Mihwa Jin and Robin T. Garrod. Formation of complex organic molecules in cold interstellar environments through nondiffusive grain-surface and ice-mantle chemistry. *The Astrophysical Journal Supplement Series*, 249:1–30, 2020.

[7] William D. Watson. The Rate of Formation of Interstellar Molecules by Ion-Molecule Reactions. , 183:L17, July 1973.

[8] Garrod, R. T. and Herbst, E. Formation of methyl formate and other organic species in the warm-up phase of hot molecular cores. *A&A*, 457(3):927–936, 2006.

[9] B. A. Mcguire. 2018 census of interstellar, circumstellar, extragalactic, protoplanetary disk, and exoplanetary molecules. *The Astrophysical Journal Supplement Series*, 239:17, 2018.

[10] L. H. Pettit. Metal ions in solution by john burgess. pp. 481. published by ellis horwood ltd. chichester and distributed by john wiley and sons, chichester and new york, 1978, £25.00 or $55.00. *Biochemical Education*, 7(1):24–24, 1979.

[11] Meng Ni, Michael K. H. Leung, Dennis Yiu Cheong Leung, and K. Sumathy. A review and recent developments in photocatalytic water-splitting using tio2 for hydrogen production. *Renewable & Sustainable Energy Reviews*, 11:401–425, 2007.

[12] Chris J. Bennett, Corey S. Jamieson, Yoshihiro Osamura, and Ralf I. Kaiser. Laboratory studies on the irradiation of methane in interstellar cometary and solar system ices. *The Astrophyscial Journal*, 653:792–811, 2006.

[13] S. Montzka, E. Dlugokencky, and J. Butler. Non-co2 greenhouse gases and climate change. *Nature*, 476:43–50, 2011.

[14] Hessam Jahangiri, James Bennett, Parvin Mahjoubi, Karen Wilson, and Sai Gu. A review of advanced catalyst development for fischer–tropsch synthesis of hydrocarbons from biomass derived syn-gas. *Catal. Sci. Technol.*, 4:2210–2229, 2014.

[15] J. Allison, R. B. Freas, and D. P. Ridge. Cleavage of alkanes by transition metal ions in the gas phase. *Journal of the American Chemical Society*, 101(5):1332–1333, 1979.

[16] N. Aristov and P. B. Armentrout. Methane activation by vanadium(1+): electronic and translational energy dependence. *The Journal of Physical Chemistry*, 91(24):6178–6188, 1987.

[17] Deng Li, Jingying Shi, and Can Li. Transition-metal-based electrocatalysts as cocatalysts for photoelectrochemical water splitting: A mini review. *Small*, 14(23), 2018-06.

[18] Z. Juo and K.C. Lau C.Y. Ng Y.C. Chang, C.S. Lam. *Frontiers and Advances in Molecular Spectroscopy*.

[19] Yuntao Xu, Yih-Chung Chang, Matthew Parziale, Anna Wannenmacher, and Cheuk-Yiu Ng. Chemical activation of water molecule by collision with spin–orbit-state-selected vanadium cation: Quantum-electronic-state control of chemical reactivity. *The Journal of Physical Chemistry A*, 124(43):8884–8896, 2020. PMID: 33078936.

[20] Yuntao Xu, Yih-Chung Chang, and Cheuk-Yiu Ng. Chemical activation of a deuterium molecule by collision with a quantum electronic state-selected vanadium cation. *The Journal of Physical Chemistry A*, 123(28):5937–5944, 2019. PMID: 31241954.

[21] Yih Chung Chang, Yuntao Xu, and Cheuk-Yiu Ng. Quantum state control on the chemical reactivity of a transition metal vanadium cation in carbon dioxide activation. *Phys. Chem. Chem. Phys.*, 21:6868–6877, 2019.

[22] Cheuk-Yiu Ng, Yuntao Xu, Yih-Chung Chang, Anna Wannenmacher, Matthew Parziale, and P. B. Armentrout. Quantum electronic control on chemical activation of methane by collision with spin–orbit state selected vanadium cation. *Phys. Chem. Chem. Phys.*, 23:273–286, 2021.

[23] Chapter 2 mechanisms of radical production. In Catherine A. Rice-Evans, Anthony T. Diplock, and Martyn C.R. Symons, editors, *Techniques in Free Radical Research*, volume 22 of *Laboratory Techniques in Biochemistry and Molecular Biology*, pages 19–50. Elsevier, 1991.

[24] Sommer L. Johansen, Marie-Aline Martin-Drumel, and Kyle N. Crabtree. Rotational spectrum of the -cyanovinyl radical: A possible astrophysical n-heterocycle precursor. *The Journal of Physical Chemistry A*, 123(24):5171–5177, 2019. PMID: 31135161.

[25] Peter William Atkins. *Physical Chemistry*. W. H. Freeman and Company, 4 edition, 1990.

[26] Jun Ye, Long-Sheng Ma, and John L. Hall. Cavity-enhanced frequency modulation spectroscopy: advancing optical detection sensitivity and laser frequency stabilization. In Bryan L. Fearey, editor, *Methods for Ultrasensitive Detection*, volume 3270, pages 85 – 96. International Society for Optics and Photonics, SPIE, 1998.

[27] Ortega Larcher Walter E. Kozameh Carlos N. Dominguez, Alfredo E. Fundamental residual amplitude modulation in electro-optic modulators. *Journal of the Optical Society of America B*, pages 1–10, 2021.

[28] J. L. Hall, L. Hollberg, T. Baer, and H. G. Robinson. Optical heterodyne saturation spectroscopy. *Applied Physics Letters*, 39(9):680–682, 1981.

[29] Axel Schenzle, Ralph G. DeVoe, and Richard G. Brewer. Phase-modulation laser spectroscopy. *Phys. Rev. A*, 25:2606–2621, May 1982.

[30] Isak Silander, Thomas Hausmaninger, Weiguang Ma, Frans J. M. Harren, and Ove Axner. Doppler-broadened mid-infrared noise-immune cavity-enhanced optical heterodyne molecular spectrometry based on an optical parametric oscillator for trace gas detection. *Opt. Lett.*, 40(4):439–442, Feb 2015.

[31] Jianxin Liu, Gang Zhao, Weiguang Ma, and Ove Axner. Development of a doppler-broadened nice-ohms system for trace gas detection based on a single sideband phase modulator. *Opt. Express*, 29(26):42411–42419, Dec 2021.

[32] James N. Hodges and Benjamin J. McCall. Quantitative velocity modulation spectroscopy. *The Journal of Chemical Physics*, 144(184201):1–8, 2016.

[33] Brian M. Sillera and Michael W. Porambo and Andrew A. Mills and Benjamin J. McCall. Noise immune cavity enhanced optical heterodyne velocity modulation spectroscopy. *Optics Express*, 19(24):24822–24827, 2011.

[34] Michael C. McCarthy and Robert W. Field. The use of magnetic rotation spectroscopy to simplify and presort spectra: An application to nih and cef. *The Journal of Chemical Physics*, 96(10):7237–7244, 1992.

[35] Michael C. McCarthy, Jonathan C. Bloch, and Robert W. Field. Frequency-modulation enhanced magnetic rotation spectroscopy: A sensitive and selective absorption scheme for paramagnetic molecules. *The Journal of Chemical Physics*, 100(9):6331–6346, 1994.

[36] Michael C. McCarthy, Hideto Kanamori, Mingguang Li, and Robert W. Field. Sideband optical–optical double resonance zeeman spectroscopy. i. theory of saturation and line shape behavior. *The Journal of Chemical Physics*, 102(21):8295–8307, 1995.

[37] Eugene Hecht. *Optics*. Addison Wesley Longman, Inc, 3 edition, 1998.

[38] Aculight Corporation. *Argos Model 2400 CW OPO User Manual*. Lockheed Martin Aculight Corporation, Bothell, WA, 2008.

[39] W. Brunner and H. Paul. I theory of optical parametric amplification and oscillation. volume 15 of *Progress in Optics*, pages 1–75. Elsevier, 1977.

[40] R. Castell, W. Demtröder, A. Fischer, and et al. The accuracy of laser wavelength meters. *Appl. Phys. B*, 38:1–10, 1985.

[41] Radu Mavrodineanu. Hollow cathode discharges: Analytical applications. *J Res Natl Bur Stand (1977)*, 89(2):143–185, 1984.

[42] Boston Electronics Corporation. *IR Detetors from Vigo System*. Boston Electronics Corporation, Brookline, Massachusetts, 2011.

[43] Thomas Hausmaninger. *Mid- and Near-infrared NICE-OHMS - Techniques for ultrasensitive detection of molecules in gas phase*. PhD thesis, Umea Universitet, 2018.

[44] Eric D. Black. An introduction to pound–drever–hall laser frequency stabilization. *American Journal of Physics*, 69(1):79–87, 2001.

[45] K. J. Astrom and T. Hagglund. *PID Controllers: Theory, Design and Tuning*. Instrument Society of America, 1995.

[46] Neil Savage. Acousto-optic devices. *Nature Photonics*, 4:728–729, 2010.

[47] John H. Scofield. Frequency-domain description of a lock-in amplifier. *American Journal of Physics*, 62(2):129–133, 1994.

[48] Brouillet, N., Despois, D., Lu, X.-H., Baudry, A., Cernicharo, J., Bockelée-Morvan, D., Crovisier, J., and Biver, N. Antifreeze in the hot core of orion - first detection of ethylene glycol in orion-kl. *A&A*, 576:A129, 2015.

[49] Rivilla, V. M., Beltrán, M. T., Cesaroni, R., Fontani, F., Codella, C., and Zhang, Q. Formation of ethylene glycol and other complex organic molecules in star-forming regions. *A&A*, 598:A59, 2017.

[50] Marla H. Moore and Reggie L. Hudson. Production of complex molecules in astrophysical ices. *Proceedings of the International Astronomical Union*, 1(S231):247–260, 2005.

[51] SE Zhu, M Kasai, H Otoge, T Sakurai, and T Machida. Cryopreservation of expanded mouse blastocysts by vitrification in ethylene glycol-based solutions. *Reproduction*, 98(1):139–145, 1993.

[52] S.A. Voelkel and Y.X. Hu. Use of ethylene glycol as a cryoprotectant for bovine embryos allowing direct transfer of frozen-thawed embryos to recipient females. *Theriogenology*, 37(3):687–697, 1992.

[53] R. J. SENGWA, RAKHEE CHAUDHARY, and S. C. MEHROTRA. Dielectric behaviour of propylene glycol-water mixtures studied by time domain reflectometry. *Molecular Physics*, 99(21):1805–1812, 2001.

[54] GN Malcolm and JS Rowlinson. The thermodynamic properties of aqueous solutions of polyethylene glycol, polypropylene glycol and dioxane. *Transactions of the Faraday Society*, 53:921–931, 1957.

[55] RJ Sengwa. A comparative dielectric study of ethylene glycol and propylene glycol at different temperatures. *Journal of molecular liquids*, 108(1-3):47–60, 2003.

[56] Miguel A Villamanan, Carlos Gonzalez, and Hendrick C Van Ness. Excess thermodynamic properties for water/ethylene glycol. *Journal of Chemical and Engineering Data*, 29(4):427–429, 1984.

[57] AV Gubskaya and PG Kusalik. Molecular dynamics simulation study of ethylene glycol, ethylenediamine, and 2-aminoethanol. 2. structure in aqueous solutions. *The Journal of Physical Chemistry A*, 108(35):7165–7178, 2004.

[58] AV Gubskaya and PG Kusalik. Molecular dynamics simulation study of ethylene glycol, ethylenediamine, and 2-aminoethanol. 1. the local structure in pure liquids. *The Journal of Physical Chemistry A*, 108(35):7151–7164, 2004.

[59] Ying Wang, Fabing Li, Wenhui Fang, Chenglin Sun, and Zhiwei Men. Study of hydrogen bonding interactions in ethylene glycol-water binary solutions by raman spectroscopy. *Spectrochimica Acta Part A: Molecular and Biomolecular Spectroscopy*, 260:119916, 2021.

[60] Yujing Chen, Yukihiro Ozaki, and Mirosław A. Czarnecki. Molecular structure and hydrogen bonding in pure liquid ethylene glycol and ethylene glycol–water mixtures studied using nir spectroscopy. *Phys. Chem. Chem. Phys.*, 15:18694–18701, 2013.

[61] Cheuk-Yiu Ng. Vacuum ultraviolet spectroscopy and chemistry by photoionization and photoelectron methods. *Annual Review of Physical Chemistry*, 53(1):101–140, 2002. PMID: 11972004.

[62] Oleg Kostko, Biswajit Bandyopadhyay, and Musahid Ahmed. Vacuum ultraviolet photoionization of complex chemical systems. *Annual Review of Physical Chemistry*, 67(1):19–40, 2016. PMID: 26980311.

[63] H. Hurzeler, Mark G. Inghram, and J. D. Morrison. Photon Impact Studies of Molecules Using a Mass Spectrometer. *The Journal of Chemical Physics*, 28(1):76–82, 08 2004.

[64] T. Baer. Why i love science: A personal statement. *The Journal of Physical Chemistry A*, 108(45):9627–9628, 2004.

[65] Gary R. Parr and James W. Taylor. A photoionization mass spectrometer utilizing a high intensity molecular beam sampling system and synchrotron radiation. *Review of Scientific Instruments*, 44(11):1578–1583, 11 2003.

[66] Leonid Belau, Kevin R. Wilson, Stephen R. Leone, and Musahid Ahmed. Vacuum ultraviolet (vuv) photoionization of small water clusters. *The Journal of Physical Chemistry A*, 111(40):10075–10083, 2007. PMID: 17715907.

[67] Oleg Kostko, Leonid Belau, Kevin R. Wilson, and Musahid Ahmed. Vacuum-ultraviolet (vuv) photoionization of small methanol and methanolwater clusters. *The Journal of Physical Chemistry A*, 112(39):9555–9562, 2008. PMID: 18578483.

[68] Franziska Bell, Qiao N. Ruan, Amir Golan, Paul R. Horn, Musahid Ahmed, Stephen R. Leone, and Martin Head-Gordon. Dissociative photoionization of glycerol and its dimer occurs predominantly via a ternary hydrogen-bridged ion–molecule complex. *Journal of the American Chemical Society*, 135(38):14229–14239, 2013. PMID: 23924376.

[69] Debashree Ghosh, Amir Golan, Lynelle K. Takahashi, Anna I. Krylov, and Musahid Ahmed. A vuv photoionization and ab initio determination of the ionization energy of a gas-phase sugar (deoxyribose). *The Journal of Physical Chemistry Letters*, 3(1):97–101, 2012. PMID: 26701259.

[70] R. Mahesh Kumar, Prathab Baskar, K. Balamurugan, Sumitesh Das, and V. Subramanian. On the perturbation of the h-bonding interaction in ethylene glycol clusters upon hydration. *The Journal of Physical Chemistry A*, 116(17):4239–4247, 2012. PMID: 22530594.

[71] Musahid Ahmed and Oleg Kostko. From atoms to aerosols: probing clusters and nanoparticles with synchrotron based mass spectrometry and x-ray spectroscopy. *Phys. Chem. Chem. Phys.*, 22:2713–2737, 2020.

[72] Leonid Belau, Kevin R. Wilson, Stephen R. Leone, and Musahid Ahmed. Vacuum-ultraviolet photoionization studies of the microhydration of dna bases (guanine, cytosine, adenine, and thymine). *The Journal of Physical Chemistry A*, 111(31):7562–7568, 2007. PMID: 17419600.

[73] Philipp Pracht. Crest website. https://crest-lab.github.io/crest-docs/page/about.

[74] Evgeny Epifanovsky, Andrew T. B. Gilbert, Xintian Feng, Joonho Lee, Yuezhi Mao, Narbe Mardirossian, Pavel Pokhilko, Alec F. White, Marc P. Coons, Adrian L. Dempwolff, Zhengting Gan, and et al. Software for the frontiers of quantum chemistry: An overview of developments in the q-chem 5 package. *J. Chem. Phys.*, 155, 084801, 2021.

[75] Narbe Mardirossian and Martin Head-Gordon. Thirty years of density functional theory in computational chemistry: an overview and extensive assessment of 200 density functionals. *Molecular Physics*, 115(19):2315–2372, 2017.

[76] Attila Szabo and Neil S. Ostlund. *Modern Quantum Chemistry: Introduction to Advanced Electronic Structure Theory*. Dover Publications, 1 edition, 1996.

[77] Bo Xu, Tamar Stein, Utuq Ablikim, Ling Jiang, Josie Hendrix, Martin Head-Gordon, and Musahid Ahmed. Probing solvation and reactivity in ionized polycyclic aromatic hydrocarbon–water clusters with photoionization mass spectrometry and electronic structure calculations. *Faraday Discuss.*, 217:414–433, 2019.

[78] Amir Golan and Musahid Ahmed. Molecular beam mass spectrometry with tunable vacuum ultraviolet (vuv) synchrotron radiation. *Journal of Visual Experiments*, 68:e50164, 2012.

[79] Kirill Khistyaev, Amir Golan, Ksenia B. Bravaya, Natalie Orms, Anna I. Krylov, and Musahid Ahmed. Proton transfer in nucleobases is mediated by water. *The Journal of Physical Chemistry A*, 117(31):6789–6797, 2013. PMID: 23805987.

[80] Jagannath Pal, Arnab Patla, and Ranga Subramanian. Thermodynamic properties of forming methanol-water and ethanol-water clusters at various temperatures and pressures and implications for atmospheric chemistry: A dft study. *Chemosphere*, 272:129846, 2021.

[81] Wenchao Lu, Ricardo B. Metz, Tyler P. Troy, Oleg Kostko, and Musahid Ahmed. Exciton energy transfer reveals spectral signatures of excited states in clusters. *Phys. Chem. Chem. Phys.*, 22:14284–14292, 2020.

[82] Antti Lignell, Laura I. Tenelanda-Osorio, and Murthy S. Gudipati. Visible-light photoionization of aromatic molecules in water-ice: Organic chemistry across the universe with less energy. *Chemical Physics Letters*, 778:138814, 2021.